POLITECNICO DI MILANO
DEPARTMENT OF MECHANICAL ENGINEERING
DOCTORAL PROGRAMME IN MECHANICAL ENGINEERING

METHODS FOR LCF LIFE PREDICTIONS IN PRESENCE OF DEFECTS

Doctoral Dissertation of:
Silvio Rabbolini

Supervisor:
Prof. Stefano Beretta

Co-Supervisor:
Prof. Huseyin Sehitoglu

Tutor:
Prof. Maurizio Vedani

The Chair of the Doctoral Program:
Prof. Bianca Maria Colosimo

AY 2011-2014 – cycle XXVII

ABSTRACT

In this Ph.D. thesis, fatigue crack growth in presence of plastic strains is discussed. This work has the aim to provide an accurate description of short crack propagation starting from defects, in order to develop elastic-plastic crack propagation models that can be included in a damage tolerant design frame.

In the first part of the work, a general overview of the propagation models present in the literature is provided. Particular attention is given to models that describe propagation in regions in which plastic strains are present, together with an accurate description of crack closure phenomenon.

In the second part of the work, the general formulation of the effective cyclic J- integral is discussed and applied to assess fatigue life of notched specimens. In this section, the effects of crack closure and temperature on short crack propagation are discussed and analyzed with the state-of-the-art models present in the literature.

In the third chapter, an experimental campaign is developed to observe crack propagation in presence of a plastic strain gradient. The activity is performed to check short crack propagation in conditions similar to those experienced by real components, such as turbine disks. A crack propagation model, obtained taking into account numerical simulations of material cyclic response, is presented and discussed. The assessment results are employed to highlight the limits of actual crack closure models.

Accordingly, the focus is shifted to the development of an innovative technique, based on digital image correlation, employed to measure crack opening levels. The technique is applied on single crystal specimens, made of a Ni-based superalloy, Haynes 230. A regression algorithm is developed to extract crack propagation driving forces from the displacement registered around the crack tips. These results are employed to measure the extent of the irreversibility present at the tip and are compared to those numerically calculated, obtained considering a single crystal plasticity code.

Finally, the experimental method based on DIC is applied to LCF. Experimental measurements are implemented in a ΔJ_{eff}-based model. The model is employed to describe crack propagation in presence of very high plastic strains, like those experienced by pipelines. The effects of material transient response on fatigue life assessment are discussed, together with the effects of the defect shape on crack opening and closing levels.

ACKNOWLEDGEMENTS

First of all, I want to express my gratitude to my parents, Anna and Luigi, who supported me throughout the course of my studies. Without their help, this could not have been possible.

Special thanks go to my advisors, Prof. Stefano Beretta and Prof. Huseyin Sehitoglu. In particular, I am very grateful to Prof. Beretta for the opportunity given to work in his research group and for the support given during all the time spent both in Politecnico di Milano and in the US. I am also very grateful to Prof. Sehitoglu, who gave me the opportunity to study at the University of Illinois at Urbana-Champaign and was always ready with his suggestions, in particular during the daily meetings we had in the office and in the lab. I would like to thank also Prof. Stefano Foletti, who was always available to discuss the concerns risen during these studies and ready to suggest a possible solution.

Finally, I'd like to thank all the colleagues I've met during these three years and all my friends, who always supported me and shared my ideas and feelings.

Part of this research activity was developed in the frame of a technical cooperation between Politecnico di Milano, Dept. of Mechanical Engineering and Ansaldo Energia SpA - AEN (Genova, Italy) about methods for life prediction under LCF. Ansaldo Energia SpA is acknowledged for the permission to publish the results presented in Chapter 2 and 3.

The research activity presented in the final part of this work was developed in the frame of a technical cooperation between Politecnico di Milano, Dept. of Mechanical Engineering and Dalmine SpA, in the frame of a research project about methods for life assessment of line pipes. Dr. Mario Rossi, director of Tenaris Dalmine Research and Development Center, and Dr. Philippe Darcis, Linepipe Product Manager, are kindly acknowledged for the permission to publish the results presented in Chapter 5.

Contents

0.1 THESIS MOTIVATION XVII
0.2 THESIS STRUCTURE XVIII

1 Literature review 1
1.1 FATIGUE LIFE DESIGN 1
1.2 FATIGUE CRACK GROWTH IN HIGH CYCLE FATIGUE AND THE ROLE OF CRACK CLOSURE 2
1.2.1 Crack closure measurements 3
1.2.2 Analytical models for crack closure evaluation 4
1.3 FATIGUE CRACK GROWTH IN LOW CYCLE FATIGUE 6
1.3.1 Models based on the cyclic J-Integral 6
1.4 PHENOMENOLOGICAL MODELS BASED ON THE APPLIED STRAIN RANGE 8
1.5 NON-CONTACT TECHNIQUES FOR LOCAL CRACK CLOSURE MEASUREMENTS 9
1.5.1 Digital image correlation 9
1.5.2 DIC setup for fatigue crack growth analysis 10
1.5.3 Crack-closure characterization with two-points digital extensometers 11
1.5.4 Stress intensity factor ranges extraction from the displacement field 12

2 Short crack propagation in the LCF regime at Room and High Temperature 15
2.1 INTRODUCTION 15
2.2 EXPERIMENTS 16
2.2.1 Test details 16
2.2.2 Strain life diagrams 18
2.3 CRACK GROWTH ANALYSIS 20
2.3.1 Analytical approach based on plastic strain range 20
2.3.2 Elastic-plastic facture mechanics approach 20
2.4 RESULTS AND DISCUSSION 24
2.4.1 LCF tests at Room Temperature 24
2.4.2 LCF tests at High Temperature 28

2.4.3 Correction of growth rate for damage at the crack tip 33
2.5 CONCLUSIONS 33

3 Short crack propagation in the dovetail attachment of a compressor disk 35
3.1 INTRODUCTION 35
3.2 COMPANION SPECIMEN DESIGN 36
3.2.1 Numerical analysis of the stress field acting at the dovetail attachment of the compressor disk of a gas turbine. 36
3.2.2 Companion specimen 38
3.2.3 Stabilized hysteresis loops at the root of the specimens notch . . 39
3.3 FATIGUE EXPERIMENTS PERFORMED ON COMPANION SPECIMENS 40
3.3.1 Nucleation 43
3.4 FATIGUE CRACK GROWTH 43
3.4.1 Stress intensity factor calculations 43
3.4.2 Crack closure implementation 44
3.4.3 Constraint factor calculation 45
3.4.4 Results and discussion 46
3.5 CONCLUSIONS 48

4 Fatigue crack growth in Ni-based superalloy single crystals 49
4.1 INTRODUCTION 49
4.2 EXPERIMENTS 50
4.2.1 Material and fatigue testing 50
4.2.2 Digital image correlation procedure 53
4.2.3 Effective stress intensity factor ranges extraction 54
4.3 RESULTS 55
4.3.1 Crack closure measurements 55
4.3.2 Effective stress intensity factor ranges and Paris curve calculations 58
4.4 STRAIN IRREVERSIBILITY AT THE CRACK-TIP 60
4.4.1 Cyclic plastic zones from extracted stress intensity factor ranges 60
4.4.2 Cyclic plastic zones from numerical simulations with single crystal plasticity 64
4.5 CONCLUSIONS 67

5 Short crack propagation in line pipes material under severe loading conditions 69
5.1 INTRODUCTION 69
5.2 EXPERIMENTS ON SMALL SCALE SPECIMENS 70
5.2.1 LCF conditions 70
5.2.2 Specimen preparation 71
5.2.3 Fatigue tests 72
5.2.4 Test results 73
5.3 CRACK CLOSURE MEASUREMENTS IN LCF WITH DIGITAL IMAGE CORRELATION 75
5.3.1 Virtual extensometers 75
5.3.2 Virtual strain gauges 76
5.3.3 Results 78

5.4 FATIGUE CRACK GROWTH IN LARGE SCALE SPECIMENS . . . 80
  5.4.1 Experiments 80
  5.4.2 Results 80
  5.4.3 Analysis of constraint 83
5.5 FATIGUE LIFE ASSESSMENT FOR LARGE SCALE SPECIMENS . 84
  5.5.1 ΔJ formulation for large scale specimens 85
  5.5.2 Fatigue life estimates 86
5.6 CONCLUSIONS 88

6 Concluding remarks **89**

Bibliography **95**

Appendices **105**

A Analysis of damage with the GTN model **107**
A.1 The GTN model for void nucleation, growth and coalescence simulation 107
A.2 Numerical simulations of tensile behavior of a line pipe steel 109
A.3 FEM simulation of the cracked small scale specimen 111

List of Figures

1.1 Crack propagation curves, for 2024-T3 aluminum alloy at different stress ratios. a) Crack growth rates as function of ΔK; b) Crack growth rates as function of ΔK_{eff} [1]. 2

1.2 Experimental crack-closure measurements. 4

1.3 ΔK reduction factor as a function of the applied load ratio R. 5

1.4 Image correlation between a reference and a deformed image. The single pixel tracking is impossible, whereas subset tracking allows the calculation of the displacements. 9

1.5 Experimental setup for the In-Situ DIC methodology. 11

1.6 Experimental crack-closure measurements with two point digital extensometers [2]: virtual displacement gages position along the defect. . . . 11

1.7 Evolution of crack flanks displacements during a fatigue cycle [2]. . . . 12

1.8 Crack tip coordinate system. 13

1.9 Experimental crack-closure measurements with full-field regression [2]: a) comparison between regressed and experimental vertical displacement field; b) individuation of K_{open} during a fatigue load cycle. 13

2.1 LCF experimental tests: a) experimental setup for HT LCF tests; b) micro-notch shape and orientation (defect depth $400\,\mu m$). 16

2.2 Plastic replica technique for crack length measurements during fatigue tests: a) replica preparation on the fracture surface, during a test interruption; b) surface crack propagation observed on a plastic replica, high temperature (defect depth 400 μm). 17

2.3 Low Cycle Fatigue tests results. a) Steel #1, room temperature; b) Steel #2, T = 490$°C$; c) Steel #3, T = 500$°C$. 19

2.4 Elastic and plastic strain energy densities employed in ΔJ calculations. 21

2.5 Definition of the significant part of the stress/strain cycle for ΔJ_{eff}. a) Seeger and Vormwald [3]. b) McClung and Sehitoglu [4]. 23

2.6 Fatigue crack growth analysis based on Tomkins model, steel #1 at room temperature: a) Comparison between experimental and predicted crack growth rates, high strain amplitude; b) Comparison between experimental and predicted crack growth rates, low strain amplitude; c) Fatigue life prediction for micronotched specimens (a_0 = 400 μm). 25

2.7 Fatigue crack growth analysis based on ΔJ_{tot}, steel #1 at room temperature: a) Crack growth rates vs. ΔJ_{tot} according to Polak; b) Crack growth rates vs. ΔJ_{tot} according to Harkegard; c) Fatigue life prediction for micronotched specimens ($a_o = 400\,\mu m$). 26

2.8 Fatigue crack growth analysis based on ΔJ_{eff}, steel #1 at room temperature: a) Crack growth rates vs. ΔJ_{eff} according to Vormwald; b) Crack growth rates vs. ΔJ_{eff} according to Sehitoglu; c) Crack growth rates vs. ΔJ_{eff} according to Zerbst; d) Fatigue life prediction for micronotched specimens ($a_o = 400\,\mu m$). 27

2.9 Fatigue life prediction for smooth specimens with ΔJ_{eff}(Eq.2.16). . . . 28

2.10 Fatigue crack growth analysis based on Tomkins formulation, steel #2 at T = 490 °C: a) Comparison between experimental and predicted crack growth rates, high strain amplitude; b) Comparison between experimental and predicted crack growth rates, low strain amplitude; c) Fatigue life prediction for micronotched specimens (a_0 = 400 μm). 29

2.11 Fatigue crack growth analysis for steel #2, T = 490$^{\circ}C$. a) Crack growth rates against effective J-Integral range, Vormwald; c) Fatigue life prediction for micronotched specimens ($a_o = 400\,\mu m$), Vormwald. 30

2.12 Fatigue crack growth analysis for steel #3, T = 500$^{\circ}C$. a) Crack growth rates against effective J-Integral range, Vormwald; c) Fatigue life prediction for micronotched specimens ($a_o = 400\,\mu m$), Vormwald. 30

2.13 Additional tests for steel #3: a) tests at R = 0.25, T= 500$^{\circ}C$; b) tests at R = -1, T= 350$^{\circ}C$. 31

2.14 Comparison between fracture surfaces at different temperatures, steel #3. a) Steel # 3, T=350$^{\circ}C$; b) Steel # 3, T = 500$^{\circ}C$; c) Steel # 3, T = 500$^{\circ}C$ after surface polishing. 32

2.15 Comparison between fracture surfaces at different temperatures, steel #2. a) Steel # 2, T=490$^{\circ}C$; b) Steel # 2, T = 490$^{\circ}C$, after surface polishing. 32

2.16 Speed increment factor against testing temperature together with 90% scatter band ($5\% - 95\%$ percentiles): the grey area corresponds to the scatter evaluated at RT for steel #1. 33

3.1 Finite element analysis of the compressor disk of a gas turbine. a) FEM model with boundary conditions; b) Refined mesh at the root of the blade attachment. 37

3.2 Load steps implemented for representing the initial overspeed (spinning test) followed by nominal speed cycles. 37

3.3 FEM results of the disk sector: a) Stress-strain behavior, b) Plastic strain field after the first unloading. 38

3.4 Specimen geometry and EDM micronotch orientation. All dimensions are expressed in millimeters. 38

3.5 FEM analysis of the companion specimen. a) Equivalent plastic strain field; b) Maximum principal stress field. 39
3.6 Results of the FE analysis: a) Load conditions considered b) with first overload (OL+BL), c) only nominal speed (BL), d) only overload (OL). 40
3.7 Companion specimen with defect and strain gauges 41
3.8 The plastic replica technique; a) Plastic replica preparation; b) Measurement of the surface crack from the replica under a microscope. 41
3.9 Experimental results. a) Crack length evolution during the tests; b) Crack growth rates vs surface crack length. 42
3.10 Experimentally registered force/strain behavior during a OL+BL test. . 42
3.11 Fracture surface after the end of a fatigue test. 43
3.12 Schematic of crack formation from the artificial defect. 43
3.13 FEM model for the calculation of constraint factor α: a) Refined mesh at the crack tip, b) Plastic zone at the crack tip at the maximum load (stabilized cycle). 45
3.14 Influence of the constraint factor α on the life prediction in OL+BL case. 46
3.15 Crack growth model results: a) crack growth rates; b) crack length. . . . 47

4.1 The experimental setup and a schematic of specimen geometry. a) Camera and lens; b) light source; c) specimen. 51
4.2 A schematic of the samples in the crystal frame showing the loading directions. $(1\ 1\ 1)$ slip planes in cyan and crack propagation planes in purple. 52
4.3 Slip plane traces analysis: a) surface of the $[0\ 0\ 1]$ oriented crystal after the end of fatigue testing; b) analytical slip plane traces calculated from EBSD crystal orientation. 52
4.4 Examples of vertical displacements of each specimen, calculated by digital image correlation a) $[0\ 0\ 1]$ oriented single crystal specimen at R=0.05 and $\Delta\sigma$=133 MPa. b) $[1\ 1\ 1]$ specimen at R=0.05 and $\Delta\sigma$=181 MPa. 53
4.5 a) An example of virtual-extensometers disposition on the $[1\ 1\ 1]$ specimen; b) A schematic showing the displacements measured by extensometers; c) Coordinate system for measuring crack opening and sliding displacements and for extracting ΔK_{eff}. 54
4.6 Virtual extensometers for the $[0\ 0\ 1]$ oriented specimen. a) The vertical crack opening displacement profiles of the $[0\ 0\ 1]$ single crystal specimen at R=0.05 and $\Delta\sigma$=133 MPa with a measured crack length of 1.23 mm. b) Crack opening levels for the $[0\ 0\ 1]$ oriented crystal. 56
4.7 Virtual extensometers for the $[1\ 1\ 1]$ oriented specimen. a) The vertical crack opening displacement profiles of the $[1\ 1\ 1]$ single crystal specimen at R=0.05 and $\Delta\sigma$=181 MPa with a measured crack length of 1.614 mm. b) The horizontal crack sliding displacement profiles of the $[1\ 1\ 1]$ single crystal specimen at R=0.05 and $\Delta\sigma$=181 MPa with a measured crack length of 1.614 mm. c) Crack opening levels for the $[1\ 1\ 1]$ oriented crystal. 57

4.8 Comparison of experimentally measured and regression vertical displacement contours in micrometers for the $[0\ 0\ 1]$ oriented single crystal. The crack length is 0.775 mm with a corresponding ΔK_I regression value of 10.78 $MPa\sqrt{m}$. 58

4.9 Comparison of experimentally measured and regression a) horizontal and b) vertical displacement contours for the $[1\ 1\ 1]$ oriented single crystal. The crack is 1.46 mm long with corresponding regression values for ΔK_I of 9.3 $MPa\sqrt{m}$ and ΔK_{II} of 9.4 $MPa\sqrt{m}$. 59

4.10 Fatigue crack growth results for polycrystalline and single crystal Haynes 230 specimens at room temperature. 60

4.11 Cyclic plastic zones calculated according to Hill's criterion and vertical contours in micrometers for the two considered orientations. a) and b) : $[0\ 0\ 1]$ oriented specimen with a crack length of 0.95 mm with an applied load equal to 50% and 100% of the maximum load, respectively. The cyclic plastic zone area, $A_{\Delta R_p}$, at the maximum load is equal to 0.03320 mm^2. c) and d) : $[1\ 1\ 1]$ oriented specimen with a crack length of 1.66 mm with an applied load equal to 50% and 100% of the maximum load, respectively. $A_{\Delta R_p}$ at the maximum load is equal to 0.2410 mm^2 63

4.12 Comparison between experimental and numerical results of Haynes 230 single crystal tensile behavior. a) $[1\ 1\ 1]$ oriented crystal; b) $[0\ 0\ 1]$ oriented crystal. 65

4.13 FEM model for the simulation of the cyclic plastic zone of the $[0\ 0\ 1]$ oriented single crystal. 66

4.14 Cyclic plastic zone calculated from single crystal plasticity simulation. a) $[0\ 0\ 1]$ specimen with a 0.96 mm long crack. Cyclic plastic zone extension, $A_{\Delta r_p}$, is equal to 0.0116 mm^2. b) $[1\ 1\ 1]$ specimen with a 1.66 mm long crack. Cyclic plastic zone extension, $A_{\Delta r_p}$, is equal to 0.1455 mm^2. 67

5.1 Hysteresis loop evolution during LCF testing. a) Test performed at R = 0.5 and ϵ_a = 0.0025 mm/mm; b) Test performed at R = -1 and ϵ_a = 0.0035 mm/mm. 71

5.2 LCF testing under severe loading conditions. a) Specimen geometry and micro-notch shape and orientation (depth 400 μm); b) Experimental setup with the digital camera employed to observe crack propagation during the experiment. 71

5.3 Compression precracking. a) Plastic zone around the notch, FEM calculations with an applied compressive stress of 400 MPa; b) Fatigue pre-crack after 500000 cycles. 72

5.4 Fracture surfaces during fatigue crack growth. a) Fracture surface in the early propagation stage; b) Surface crack propagation on a sample surface, observed on a plastic replica; c) Fatigue crack surface after the end of the experiment. 73

5.5 Fatigue crack growth analysis based on ΔJ_{eff} [3]. Crack opening and closing levels calculated according to Newman [5]. 74

5.6 An image of the fracture taken with the optical microscope during a fatigue test. 74

5.7 Crack closure measurements with two-point digital extensometers. a) Disposition of the extensometer on the two crack flanks; b) Force vs COD plot. The extensometer was positioned 50 μm before crack tip. . . 76

5.8 Crack closure measurements in LCF with DIC. a) Virtual strain gauge position, Vormwald's proposal [3]; b) local stress/strain loop measured under the EDM notch; c) Virtual strain gauge position near crack-tip. d) local stress/strain loop measured in the cyclic plastic zone. 77

5.9 Crack closure measurements in LCF with DIC. a) Virtual strain gauge position adopted for crack closure estimates; b) comparison between local and global hysteresis loops and opening and closing levels identification. 78

5.10 Crack closure measurements in LCF with DIC on small scale specimens. a) comparison between local and global hysteresis loops and opening and closing levels identification for tests conducted at R = -1; b) comparison between local and global hysteresis loops and opening and closing levels identification for tests conducted at R = 0.5. 78

5.11 Comparison between experimental and analytical effective stress amplitudes, small scale specimens. a) R = -1, ϵ_a = 0.0035 mm/mm; b) R = 0.5, ϵ_a = 0.0025 mm/mm. 79

5.12 Fatigue crack growth analysis based on ΔJ_{eff} [3]. a) Crack opening and closing levels calculated according to Newman; b) Crack opening and closing levels calculated from DIC measurements. 79

5.13 LCF testing on large scale specimens. a) Schematic of the large scale specimen, together with micro-notch geometry and disposition. b) The specimen mounted in the 250 kN load frame. 80

5.14 Crack closure measurements in LCF with DIC on large scale specimens. a) comparison between local and global hysteresis loops and opening and closing levels identification for tests conducted at R = -1; b) comparison between local and global hysteresis loops and opening and closing levels identification for tests conducted at R = 0.5. 81

5.15 Comparison between experimental and analytical effective stress amplitudes, large scale specimens. a) R = -1, ϵ_a = 0.0035 mm/mm; b) R = 0.5, ϵ_a = 0.0025 mm/mm. 82

5.16 Fracture surface of two large scale specimens after the end of the test. a) Initial defect depth 1.4 mm, R = 0.5; b) Initial defect depth 0.7 mm, R = -1. 82

5.17 Numerical analysis of the large scale specimen. a) Mesh refinement along the crack front; b) boundary conditions; c) Plastic zone around the crack front, crack deepest point. 83

5.18 Numerical analysis of the large scale specimen for J validation: comparison between numerical and analytical results, expressed in terms of J vs applied force. 86

5.19 Fatigue life assessment for the two broken specimens. The cross represents the experimental point, whereas the dashed and continuous lines are, respectively, the results of the simulations performed considering the models based on ΔJ_{tot} and ΔJ_{eff}. a) Test performed at R = -1; b) Test performed at R = 0.5. 87

6.1 Comparison between crack opening levels calculated according to Newman and experimental measurements at R = -1. Grey points represent results presented in [3], whereas red points are those experimentally measured in this work. 91

A.1 Numerical models employed for monotonic stress/strain simulation. a) Boundary conditions of the axial-symmetric model; b) Numerical stress distribution at necking in the 2D model; c) Boundary conditions of the 3D model; d) Numerical results for the 3D geometry at necking. 110
A.2 Comparison between experimental and numerical stress/strain curves. . 111
A.3 3D model of the 0.5 mm deep semi-circular crack. a) Void volume fraction after the first load. b) Equivalent plastic strain (PEEQ) distribution around the crack front. 112

List of Tables

2.1 Summary of the experimental tests. 18

3.1 Constraint factor - α - calculated through FE analyses for the OL+BL load case. 46

4.1 Chemical composition (%wt) of Haynes 230. 50
4.2 Selected tensile properties of Haynes 230 alloy specimens 51
4.3 Effective Paris Law fits from fatigue crack growth tests of Haynes 230 alloy. Crack growth rates measured in mm/cycle and stress intensity factor ranges in $MPa\sqrt{m}$. 60
4.4 Coefficients employed for FEM simulations. 66

5.1 Stress and strain components for ΔJ_{tot} and ΔJ_{eff} formulations. 87

A.1 GTN model parameters. 109

INTRODUCTION

0.1 THESIS MOTIVATION

Nowadays, gas turbines and other components employed for power generation are subjected to several load cycles during their lifetime, since they are switched on and turned off several times each day, in order to meet the peak loads requested by users. High plastic strain can be present in these components, since high loads, applied to the structures during start-ups and turn-offs, can generate yielding in certain regions, such as near notches.

In order to take into account these conditions, state-of-the-art procedures consider fatigue life assessment as a crack propagation problem. Fatigue crack growth is usually described taking into account material elastic-plastic behavior and crack growth rates are described as a function of elastic-plastic parameters, such as the applied plastic strain range or the cyclic J-Integral.

These models, however, present several limits. First, there are simplified equations based on fatigue load cycles calculated by adopting Masing's hypothesis, a feature that does not take into account transient phenomena, such as ratchetting and mean stress relaxation. Then, they consider the effects of crack closure, but opening levels are usually calculated by adopting analytical models, known to be valid only under fully reversed loadings.

These conditions represent the motivation and the starting point of this Ph.D. thesis, which aims to study crack propagation in plastic zones. In this work the attention is mainly focused on the effects of crack closure and material cyclic behavior and to the possibility to apply the general formulation of ΔJ in fatigue life assessment for components subjected to LCF conditions.

0.2 THESIS STRUCTURE

- *Chapter 1: Literature review.* An overview of fatigue crack growth mechanisms is provided, with emphasis on models that describe crack propagation in plastic regions. The influence of crack closure is discussed, together with a description of the experimental techniques employed to measure opening and closing levels. In the final part of the chapter, a non contact technique, based on computer vision, is presented and its application to fatigue crack growth is discussed.
- *Chapter 2: Short crack propagation in the LCF regime at Room and High Temperature.* An experimental campaign is developed in order to check the effects of high temperature in short crack propagation. Experimental results are compared to the assessments provided by short crack propagation models present in the literature.
- *Chapter 3: Short crack propagation in the dovetail attachment of a compressor disk.* An experimental campaign is performed to check crack propagation in presence of a plastic strain gradient. Experimental results are employed to develop a model capable of describing crack propagation when elastic shakedown conditions are present.
- *Chapter 4: Fatigue crack growth in Ni-based superalloy single crystals.* Fatigue crack growth in single crystals of a Ni-based superalloy is investigated. An innovative technique based on digital image correlation is employed to extract the effective stress intensity factor ranges from the displacement fields measured around crack tips. The extracted ΔK are employed to evaluate the extension of the plastic zones surrounding the tips. Experimental results are then compared to those numerically calculated considering a single crystal plasticity code.
- *Chapter 5: Short crack propagation in line pipes material under severe loading conditions.* An experimental campaign is developed to check crack propagation in presence of very high plastic strains in large scale specimens. Fatigue lives of notched specimens are assessed by implementing the crack propagation model based on the effective J-Integral range. The ΔJ formulation is modified in order to take into account the geometry of large scale specimens, whereas experimental $da/dN - \Delta J$ curves from small scale specimens and measured closure levels on large scale specimens are employed to evaluate crack growth rates.

CHAPTER 1

Literature review

1.1 FATIGUE LIFE DESIGN

Unexpected failure of railway axles, designed to withstand loads higher than those registered during in-service conditions, introduced in the XIX century the concept of fatigue design. Since then, fatigue crack growth mechanisms have been intensively investigated and different fatigue life assessment procedures have been proposed.

Lately, damage tolerant design has become the state of the art of fatigue design, especially for aeronautic applications [6,7]. According to this design frame, it is assumed that a crack is present in the component and it can grow during in-service operations. Fatigue life is then assessed by calculating the number of cycles necessary for a defect to propagate and cause the failure of the component. Such an approach, integrated with an adequate inspection plan, has proven to be cost efficient and to increase overall safety.

It is widely recognized that the accuracy of the fatigue life assessed following a damage tolerant frame strongly depends on the model adopted to describe crack propagation. Crack growth models present in the literature can be divided into two different categories, depending on the applied loading conditions: models describing high cycle fatigue (HCF) propagation and low cycle fatigue (LCF) crack growth can be found.

In the first case, these models consider that the plastic zone surrounding the crack tip has a limited extension and it is relatively small respect to the dimensions of the cracked body. For this category of defects, usually referred as 'long cracks', an approach based on Linear Elastic Fracture Mechanics (LEFM) is applicable and crack growth rates can be related to the stress intensity factor, ΔK.

In the second category, crack propagation occurs in zones where plastic strains are present: this usually happens near notches or when the crack length is small respect to the plastic zone present at the tip. In such a condition, also referred as 'short crack' propagation, experimentally observed crack growth rates are higher than those predicted by LEFM. Therefore, an approach based on Elastic-Plastic Fracture Mechanics (EPFM) is necessary: several models based on the applied plastic strain range, $\Delta\epsilon_p$, or the cyclic J-Integral, ΔJ, have been proposed in the literature and have been included in several procedures.

In this section, an overview of state of the art of fatigue crack growth is provided, considering both HCF and LCF conditions.

1.2 FATIGUE CRACK GROWTH IN HIGH CYCLE FATIGUE AND THE ROLE OF CRACK CLOSURE

When the plastic strains are confined in a small region ahead of the crack tip, crack growth rates, da/dN, are related to the applied stress intensity factor range, ΔK, through the Paris equation [8], as proposed in Eq. 1.1.

$$\frac{da}{dN} = C\left(\Delta K\right)^n \tag{1.1}$$

First large experimental campaigns [9], conducted on servo-hydraulic load frames, showed a marked dependence of material constants (C and n) to the applied load-ratio. In particular, experimental observations showed that higher load-ratios usually implied higher crack growth rates, as shown in Fig. 1.1a.

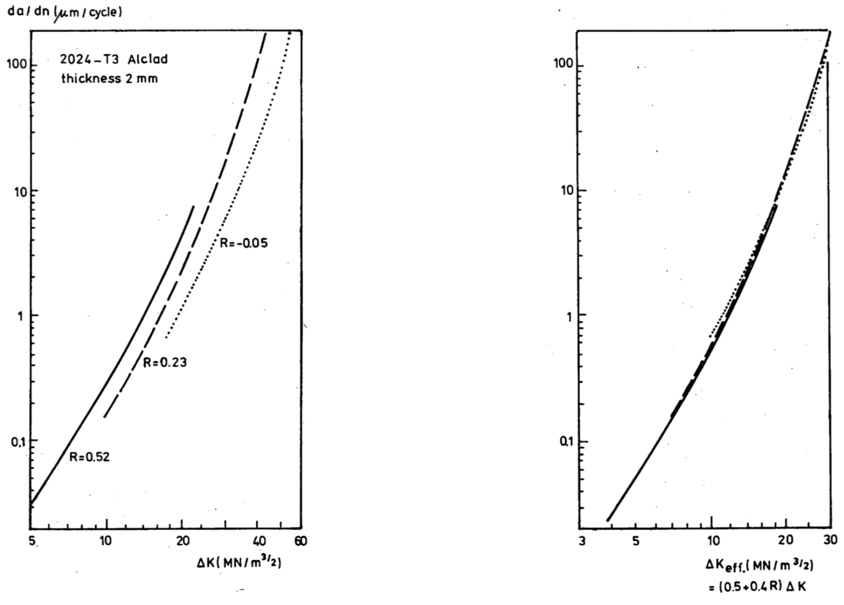

(a)

(b)

Figure 1.1: *Crack propagation curves, for 2024-T3 aluminum alloy at different stress ratios. a) Crack growth rates as function of ΔK; b) Crack growth rates as function of ΔK_{eff} [1].*

In 1970, Elber [10] observed that a crack stays closed for a part of the fatigue load cycle, even if the applied stress is positive in tension. This phenomenon, also known as plasticity induced crack-closure, cannot be explained by the theory of elasticity and it is due to the plastic strains acting at the tip. During propagation, a plastically deformed area is generated at the tip, leaving a plastic wake along the crack length: this zone, characterized by residual compressive stresses, is the one responsible for crack-closure, since crack tip opening is possible only when the applied stress overcomes this residual stress field. Taking into account only the portion of ΔK after crack opening, Elber was able to remove the load-ratio effect, demonstrating plasticity induced crack-closure main role and that only a parameter, which he defined effective stress intensity factor range (ΔK_{eff}), can be used in crack growth rates prediction (Fig.1.1b).

Several other different mechanisms responsible for crack-closure have been recognized (i.e. roughness-induced, trasformation-induced, oxidation induced and many others [11]), which play a significant role especially in the near-threshold region or during in-plane shear propagation.

1.2.1 Crack closure measurements

After the introduction of ΔK_{eff}, many experimental methods have been developed to empirically evaluate crack-closure levels. All the experimental procedures described in the literature can be classified in two main categories, usually referred as 'global' and 'local' compliance methods. All the measurements based on Clip-Gages at the crack mouth or on Back Face Strain Gages [12] belong to the first category, whereas local strain measurements, obtained with dedicated strain-gages positioned in the vicinity or across the crack tip belongs to the second one. Examples of this methods are presented in [3, 13, 14].

The state-of-the-art procedures employed for crack-closure evaluation are reported in Fig. 1.2: the global load-strain method, proposed in [12], is reported in Fig. 1.2a, whereas the compliance offset method [15] is presented in Fig. 1.2b. Local compliance methods are proposed in the two remaining plots. In Fig. 1.2d the load cycle at the tip (Fig. 1.2c) is amplified into a load-strain offset one, for a more accurate measurement of crack-closure levels [16].

Talking about the 'global' methods, the opening load is evaluated by observing that the load-strain curve is linear when the crack stays open and becomes non-linear when it starts closing. Considering the compliance offset method, the crack is conventionally open when the line assumes a value of compliance offset equal to a fixed offset criterion (a level of 2% is usually employed). Regarding the 'local' methods, the original procedure proposed in [16] was modified by Toyosada and Niwa [17], for the evaluation of the opening and closing points of the cycle, P_{op} and P_{cl} respectively. P_{cl} is evaluated as the flexing point of the unloading branch of the hysteresis offset curve, whereas P_{op} is the point of the loading branch of the curve which has the same slope registered at the closing point, as shown in Fig. 1.2d.

In the literature, more than these mainly adopted methods can be found. Among them it is worth to remember those based onto optical interferometry [18], thermography [19], ultrasonic measurements [20] and digital image correlation [2]. A review of digital image correlation techniques is reported in Section 1.5.

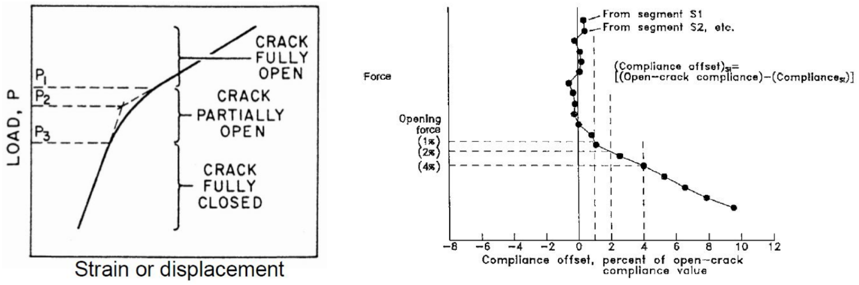

(a) Load-strain curve by global method [12]

(b) Compliance offset method [15]

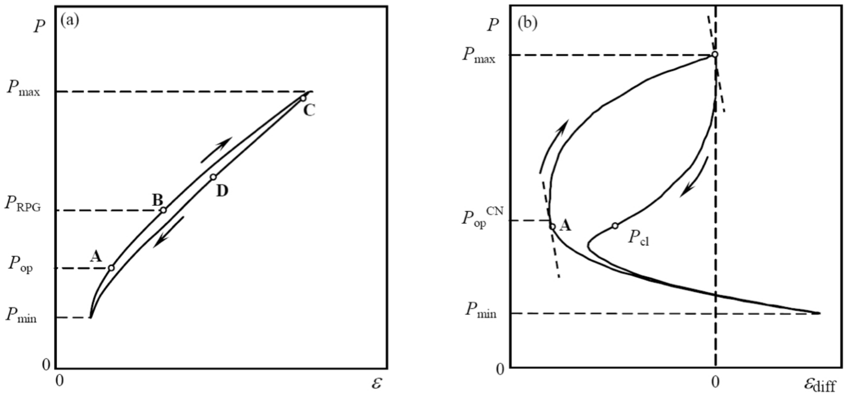

(c) Load-strain cycle by 'local method', adopting strain gages [16]

(d) Load-strain offset cycle [16]

Figure 1.2: *Experimental crack-closure measurements.*

1.2.2 Analytical models for crack closure evaluation

The wide amount of data present in the literature was employed to develop analytical models for the estimation of crack opening levels. In his original work, Elber [10] proposed the adoption of a reduction factor, U, which represents the percentage of the total stress intensity factor during which the crack stays open (Eq.1.2).

$$U = \frac{\Delta K_{eff}}{\Delta K} = \frac{\Delta \sigma_{eff}}{\Delta \sigma} \Rightarrow \frac{da}{dN} = C\left(\Delta K_{eff}\right)^n = C\left(U \cdot \Delta K\right)^n \tag{1.2}$$

One of the most adopted equations to describe U is the formulation proposed by Schijve, which is shown in Eq.1.3 and depicted in Fig.1.3 [21].

$$U = 0.55 + 0.35R + 0.12R^2 \tag{1.3}$$

This equation is valid in the $-1 \leq R \leq 0.54$ range and highlights the fact that at high R the reduction factor tends to 1, meaning that the crack during the fatigue cycle always stays open, whereas, during a test performed under fully-reversed loading conditions, the crack stays open only for 32% of the applied load range.

The state of the art, for crack-closure evaluation, is represented by the analytical model proposed by Newman [5]. The reduction in ΔK is calculated according to

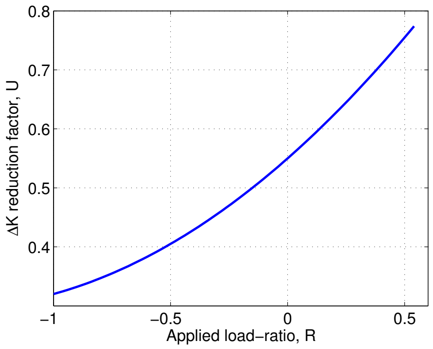

Figure 1.3: ΔK *reduction factor as a function of the applied load ratio R.*

Eq.1.4, where R is the applied stress ratio and f is the ratio between the opening stress, σ_{open}, and the maximum applied stress, σ_{max}, evaluated according to Eq. 1.5.

$$\Delta K_{eff} = \frac{1-f}{1-R}\Delta K \tag{1.4}$$

$$f = \frac{\sigma_{open}}{\sigma_{max}} = \begin{cases} max\left(R, A_0 + A_1 R + A_2 R^2 + A_3 R^3\right), & \text{if } R \geq 0 \\ A_0 + A_1 R, & \text{if } -2 \leq R < 0 \end{cases} \tag{1.5}$$

where the coefficients are evaluated as:

$$\begin{aligned} A_0 &= \left(0.825 - 0.34\alpha + 0.05\alpha^2\right)\left[cos\left(\frac{\pi}{2}\frac{\sigma_{max}}{\sigma_0}\right)\right]^{1/\alpha} \\ A_1 &= \left(0.415 - 0.071\alpha\right)\frac{\sigma_{max}}{\sigma_0} \\ A_2 &= 1 - A_0 - A_1 - A_3 \\ A_3 &= 2A_0 + A_1 - 1 \end{aligned} \tag{1.6}$$

In this set of equations, α is the costraint factor and σ_{max}/σ_0 is the ratio between the maximum applied stress and the flow stress.

Several formulations of σ_0 have been proposed. Newman [5] originally suggested to assume σ_0 as the average of the ultimate tensile strength, R_m, and the yielding stress, σ_Y. Savaidis [22] demonstrated that satisfactory results can be achieved by replacing Newman's proposal with the value of the cyclic yield stress. It has been demonstrated [23] that the adoption of σ_{max}/σ_0 as a constant produces acceptable results for positive stress ratios, where the effect of this parameter on the crack opening function is relatively small.

Models based on ΔK-controlled propagation and crack closure evaluation have been implemented in several fatigue assessment codes, which belong to the so-called 'Damage-tolerant' design. An approach based on ΔK-based propagation can be employed far all those components in which the applied plastic strains are negligible, such as railway axles. An example of this assessment procedure is presented in [24].

1.3 FATIGUE CRACK GROWTH IN LOW CYCLE FATIGUE

Traditional procedures based on ΔK cannot be applied in LCF, since defects usually grow in zones (i.e. near notches) where high plastic strains are present, violating LEFM main assumptions [25]. In the literature, two different approaches have been proposed in order to describe crack propagation in such a condition. The first one is based on EPFM: according to this approach, the stress intensity factor range, ΔK, is replaced in the Paris equation by a different parameter, the cyclic J-Integral, ΔJ, in order to characterize the different strain condition present at the tip. On the other part, phenomenological models have been developed. According to this models, crack propagation under LCF conditions can be described as a function of the applied plastic range. In this section an overview of the two different approaches is provided.

1.3.1 Models based on the cyclic J-Integral

Trying to find a parameter capable of describing the strain field around the tip during short crack propagation, Dowling [26] extended Rice's path independent J-Integral [27] to the cyclic case, proposing to modify the Paris relationship [8], by replacing the stress intensity factor range, ΔK, with ΔJ.

According to Dowling [28], ΔJ is calculated by replacing, in the analytical formulation of J, the applied stresses and strains, with the equivalent stress and strain ranges. This means that ΔJ is calculated by replacing the monotonic σ - ϵ curve, expressed as reported in Eq. 1.7, with the equivalent $\Delta\sigma$ - $\Delta\epsilon$ one, neglecting the unloading part of the fatigue cycle.

$$\epsilon = \epsilon_{el} + \epsilon_{pl} = \frac{\sigma}{E} + \left(\frac{\sigma}{k_i}\right)^{1/n_i} \tag{1.7}$$

Dowling's formulation also implies that ΔJ and J have the same main properties: it can be assumed that the cyclic J-Integral is the sum of an elastic and a plastic component. Starting from the works of Shih [29] and Shih and Hutchinson [30], Dowling [31] demonstrated that, in the cyclic case, the elastic part is function of the applied stress range, $\Delta\sigma$, whereas the plastic component is a function of $\Delta\epsilon_p$, the plastic strain range. In Eq. 1.8, the general formulation of ΔJ is reported: the elastic part of the cyclic J-integral not only depends on the applied stress range, but also on a constant, Y, which takes into account the geometry of the cracked component and on a, the crack length. It is also worth remarking that the elastic component is a function of the loading condition present at the tip: when plane stress conditions are considered, E' is replaced by E, the Young's modulus, whereas $E' = E/\left(1 - \nu^2\right)$ in case of plane strain.

$$\Delta J = \Delta J_{el} + \Delta J_{pl} = Y^2 \frac{\Delta\sigma^2}{E'} \pi a + g\left(n_i\right) \Delta\sigma \Delta\epsilon_p \pi a \tag{1.8}$$

On the other hand, the plastic component of ΔJ depends on a function, $g\left(n_i\right)$, which takes into account material inelastic behavior, since it depends on n_i, the exponent of the cyclic stress/strain curve. Several formulations of $g\left(n_i\right)$ have been proposed. The most employed formulations of $g\left(n_i\right)$ are reported in Eq. 1.9 [31], where it can be noted that the plastic correction function also depends on the loading conditions present at the tip.

$$g(n_i) = \begin{cases} \frac{1}{\sqrt{n_i}}, & \text{plane stress} \\ \frac{3}{4\sqrt{n_i}}, & \text{plane strain} \end{cases} \tag{1.9}$$

In the literature, several models based on ΔJ have been proposed to describe crack propagation in the LCF regime. Polak [32] was able to analyze the early propagation phase in an austenitic-ferritic duplex stainless steel by applying a ΔJ-based model, underlining the possibility to adopt cyclic J-integral models to describe short crack propagation. Harkegard [33] applied the J-integral model to assess fatigue life of specimens subjected to fully reversed strains in the LCF regime. In order to obtain conservative estimates, Harkegard considered a $da/dN - \Delta J$ curve obtained from crack propagation data at R=0: this was done in order to include the effects of crack closure.

Apart approaches based on ΔJ, it has been recognized that plasticity induced crack closure plays an important role even in LCF. Crack closure effects were implemented in ΔJ calculations by McClung and Sehitoglu [4,34] together with Seeger and Vormwald [3, 35]. The reduction of the J-Integral range was quantified by lessening stress and plastic strain ranges, considering only the portion of the load cycle in which the crack stays open.

Crack opening levels were calculated adopting the model proposed by Newman [5] for long cracks (see Eq. 1.5), where S_{op} for a given R depends on the constraint factor and the ratio $\sigma_{max}/\sigma_{flow}$. In these models, a value of α equal to 1 was usually taken into account, whereas different formulations of σ_0 have been proposed. In their works, Vormwald and Seeger [3, 35] proposed to modify Newman's original formulation by replacing the yield stress with the corresponding cyclic yield stress. On the other part, even McClung and Sehitoglu [4] suggested to modify the value of σ_0: not only they replaced the yield stress with the corresponding cyclic yield stress, but also replaced the ultimate tensile strength with the ultimate stress, calculated according to Eq. 1.10, where k_i and n_i are the values of Eq. 1.7 that describe the cyclic stress/strain curve.

$$\sigma_u = \frac{k_i \cdot n_i^{n_i}}{1 + n_i} \tag{1.10}$$

Lately, Zerbst $et\ al.$ [36, 37] proposed to apply the J-Integral calculation adopted in engineering fracture assessment [38, 39]. In particular, from the elastic stress intensity factor range, ΔJ is evaluated as a function of the yielding parameter $L_r = \sigma_{max}/\sigma_{ref}$ and then ΔJ_{eff} is calculated adopted the same concepts as Seeger & Vormwald. Another application of this model to short crack case and fatigue can be found in [40].

1.4 PHENOMENOLOGICAL MODELS BASED ON THE APPLIED STRAIN RANGE

Trying to follow a more phenomenological approach, several authors assumed that crack propagation, in the LCF regime, is a function of the applied plastic range, $\Delta\epsilon_p$. The main contribution in this field is the work published by Tomkins [41], who related crack growth rates to the plastic strain range through an exponential law. Tomkins proposal is reported in Eq.1.11, in which ϵ_{ap} is the applied plastic strain amplitude, a is the crack length and k_{g0} and d are material constants.

$$\frac{da}{dN} = k_{g0}\epsilon_{ap}^{d}a \tag{1.11}$$

Following these assumptions, Polak [42,43] was able to correctly assess fatigue life of specimens containing a micro-notch, deriving model parameters from the traditional Manson-Coffin curve constants.

A different formulation is the model proposed by Skelton [44], included in the British R5 procedure [45]. According to this model, the growth of short cracks in regions of cyclic plasticity can be described by an high strain fatigue crack growth law, given by:

$$\frac{da}{dN} = B'a^{Q} \tag{1.12}$$

where B' is a constant determined at unit crack depth and it is related to the total strain range and Q is a material constant, usually equal to 1. In the R5 standard, it is suggested that a conservative estimate of B', for tests performed in air, can be calculated as:

$$B' = 2.61 \cdot 10^{4} \cdot \Delta\epsilon^{2.85} \tag{1.13}$$

An interesting feature of this model is that it can be modified in order to divide the propagation process into nucleation and growth, following what proposed in Eq. 1.14, where a_{min}, the critical length which separates nucleation from growth, is equal to 0.2 mm.

$$\frac{da}{dN} = \begin{cases} B'a_{min}^{Q}, & a \leq a_{min} \\ B'a_{min}^{Q}, & a > a_{min} \end{cases} \tag{1.14}$$

It is worth remarking that, in this models, the effects of crack closure are neglected, meaning that they assume a crack fully open for the entire fatigue cycle. It should be noted, however, that the models based on Tomkins assumptions present a limit, since they are able to correctly predict crack growth rates and fatigue life only when a marked plastic strain range is present, while unconservative estimates are provided when the plastic part of the strain range tends to zero [46].

1.5 NON-CONTACT TECHNIQUES FOR LOCAL CRACK CLOSURE MEASUREMENTS

In the past, a variety of experimental techniques based on extensometers or strain gages has been employed to measure the phenomenon of crack closure. In section 1.2.1, a brief overview of these techniques is provided. Nowadays, the continuous advancement in computer vision has opened the way to the introduction and the development of new non-contact techniques, such as digital image correlation (DIC). In this section, a brief overview of DIC is provided, together with its application to fatigue crack growth.

1.5.1 Digital image correlation

DIC was originally developed in the early 1980s at the University of South Carolina [47–50], with the idea to measure full-field in-plane displacements and displacement gradients of a strained body. The main concept of this technique is that displacements can be calculated by comparing the position of the features present in two images of a target surface.

Technically speaking, the correlation software tracks the position of the pixels of a set of digital pictures. The first picture of the set is usually taken at zero load and it is referred as *reference* or *undeformed* image, while the other picture, usually acquired when the body is externally loaded, is usually referred as *deformed*. Since it is impossible to uniquely define the position of each pixel of the reference image in the deformed image, the correlation algorithm tracks the changes in position of small groups of pixels, called subsets. An example of how the correlation algorithm works is shown in Fig. 1.4, in which it is also highlighted the impossibility to track the displacement of single pixels.

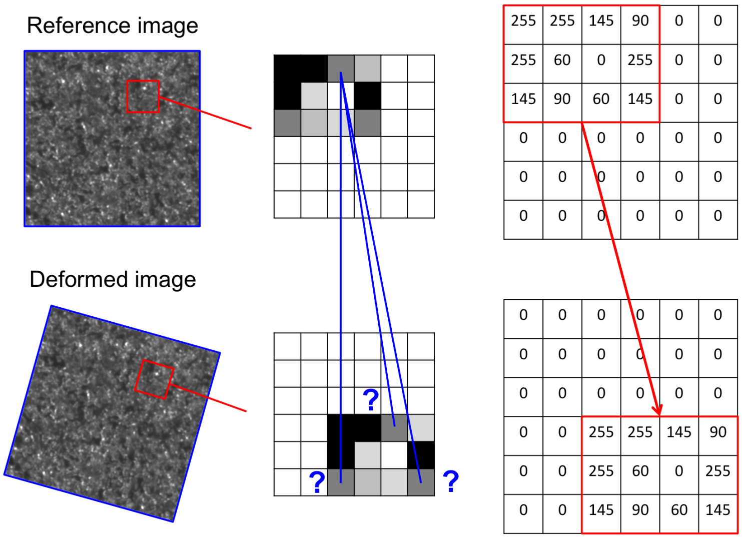

255	255	145	90	0	0
255	60	0	255	0	0
145	90	60	145	0	0
0	0	0	0	0	0
0	0	0	0	0	0
0	0	0	0	0	0

0	0	0	0	0	0
0	0	0	0	0	0
0	0	0	0	0	0
0	0	255	255	145	90
0	0	255	60	0	255
0	0	145	90	60	145

Figure 1.4: *Image correlation between a reference and a deformed image. The single pixel tracking is impossible, whereas subset tracking allows the calculation of the displacements.*

The dimension of the subset is a critical parameter for the correlation software. In order to achieve better results, subset dimension should be as small as possible, but it should also guarantee an accurate identification of the subset in the deformed picture.

It is evident that this strongly depends on the dimension of the features present on the measurement surface.

In order to improve the accuracy of the measurements, the target surface should be accurately prepared. The best results are usually obtained by adopting a random speckle pattern, which corresponds to a group of pixels on the gray scale (from 0, black, to 255, white) in the images acquired with a monochrome digital camera. The pattern can be applied by adopting different techniques, depending on the required measurement accuracy. In particular, the dimension and the distribution of the speckles on the target surface influence the accuracy and the resolution of the measured displacements. It has been proved [2] that the refined speckle pattern, obtained with an airbrush and black paint, gives satisfactory results in the measurements of displacements around crack-tips with high magnifications.

Another parameter which influences the quality of the measurement is *subset spacing*, which is the distance, expressed in pixels, between the centers of each subset. This spacing usually ranges from 3 to 10 pixels, with the former value providing a field with an higher number of readings, whereas the latter gives back a smoother field.

DIC can be employed following two different procedures: in the literature *Ex-Situ* and *In-Situ* DIC techniques can be found. In the first case, both the reference and the deformed images are acquired at zero load and out of the load frame. These displacement fields can be used to measure the residual strain field that remains on the target surface after the test. This procedure is useful to observe the evolution of local strain and phenomena such as slip and twinning at very high magnifications, since it allows the acquisition of the image with optical microscopes, that guarantee the adoption of high magnification, but cannot be used for real-time acquisition [48, 51, 52], a feature that makes *Ex-Situ* DIC not suitable for fatigue applications. In the second situation, the images are acquired during the experiment, when the specimen is mounted in the load frame, and the displacement fields can be measured in *real time*. This feature is interesting for fatigue, since it is useful to analyze the evolution of the displacement field around a crack during a fatigue cycle, allowing the measurement of crack opening and closing levels. In the next section, the application of *In-Situ* DIC to fatigue is discussed.

1.5.2 DIC setup for fatigue crack growth analysis

In-Situ DIC has been vastly employed for fatigue crack growth analysis, in particular to study the effects of crack-closure, since it allows the observation of the displacement and strain fields around a crack tip during a fatigue load cycle. In Fig. 1.5, a schematic of the experimental setup for a stress-controlled fatigue test is proposed: the load applied to the specimen is monitored by a load cell, which sends the signal to a computer. The computer not only controls the applied stress amplitude, but also a digital mono-chrome camera, responsible for picture acquisition. One interesting feature of this setup is that this configuration allows not only the acquisition of several pictures during each fatigue cycle, but also the measurement of the stress at which each picture is taken.

In order to characterize crack propagation, during a fatigue test, several pictures are acquired for each fatigue cycle. By applying the correlation algorithm, an accurate measurement of the evolution of the displacement field acting at the tip is possible. Ex-

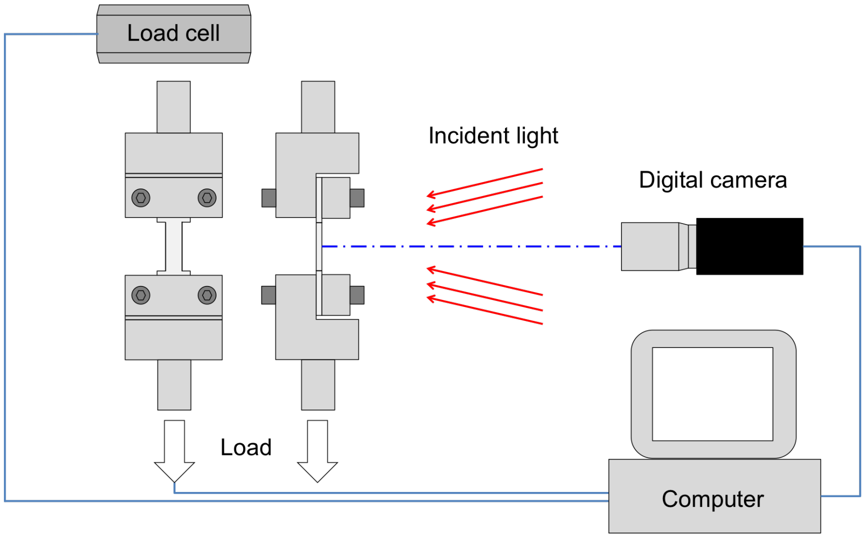

Figure 1.5: *Experimental setup for the In-Situ DIC methodology.*

perimental data can be analyzed by adopting two different techniques. By tracking the relative displacements of the crack flanks, crack opening and closing levels can be extracted and an estimate of crack closure evolution during propagation can be obtained. On the other part, the study of the singularity present at the tip can be employed to evaluate crack propagation driving forces. In the following sections, a review of these two techniques is provided.

1.5.3 Crack-closure characterization with two-points digital extensometers

The first application of DIC in fatigue is derived from the experimental techniques discussed in section 1.2.1. This method consists in applying a series of two point digital extensometers along a crack, in order to measure the relative displacements of the two crack flanks. Extensometers are placed perpendicular to the crack plane, in order to directly measure opening as the difference between the vertical displacements measured on the upper and the lower crack flank. An example of the disposition of the virtual gages along a crack is reported in Fig. 1.6.

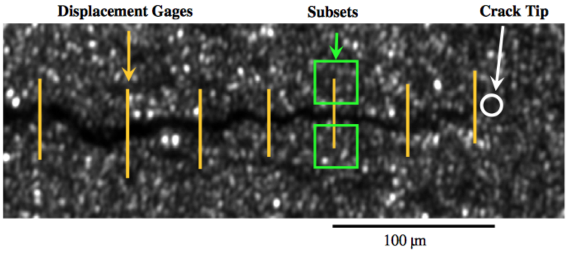

Figure 1.6: *Experimental crack-closure measurements with two point digital extensometers [2]: virtual displacement gages position along the defect.*

This technique, originally presented in [53, 54], is useful to measure crack opening levels and to calculate the effective stress intensity factor ranges, following Elber's proposal [10, 55]. In Fig. 1.7, a schematic of the evolution of crack flanks profiles during a fatigue cycle is provided, showing that DIC can be successfully applied to measure crack opening levels.

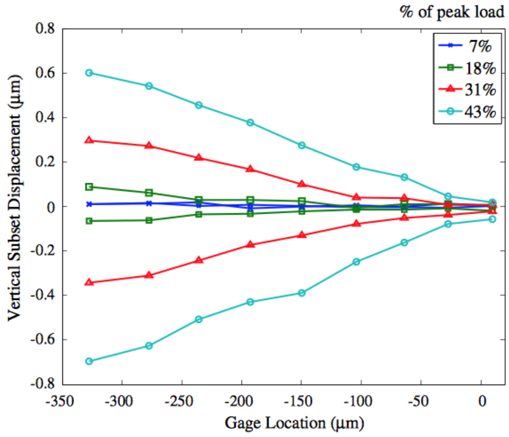

Figure 1.7: *Evolution of crack flanks displacements during a fatigue cycle [2].*

Two points digital extensometers can be also employed to study mixed-mode crack propagation: when a crack experiences a combined Mode I+II load, the difference between the horizontal displacements registered on the two flanks can be used to study the effects of sliding. Sangid et Al. [56] successfully applied this technique to study crack opening/sliding levels for a crack subjected to mixed mode loading (Mode I+II) in a 316L steel single crystal.

1.5.4 Stress intensity factor ranges extraction from the displacement field

The second approach is based on the original proposal of McNeill et Al. [57], who extracted K_I from the crack tip displacement field measured with DIC in a c-specimen. This technique, usually referred as *full-field regression*, allows the extraction of K by fitting the experimental displacements with the equations provided by continuum mechanics.

In order to correctly extract K, the analytical expression of the singular field proposed by Williams [58] was modified to take into account the effects of rigid body rotations and translations [2, 57]. Therefore, the vertical displacement field around a crack tip subjected to mode I opening in an isotropic body can be written as:

$$\begin{aligned} v =& \frac{k_I}{\mu}\sqrt{\frac{r}{2\pi}} sin\left(\frac{\theta}{2}\right)\left[\frac{1}{2}(k+1) - cos\left(\frac{\theta}{2}\right)\right] - \frac{1}{2\mu}\left(\frac{\nu}{1+\nu}\right) Trsin\left(\theta\right) + \\ &+ Arcos\left(\theta\right) + B \end{aligned} \tag{1.15}$$

where μ is the shear modulus, $k = (3-\nu)/(1+\nu)$, T is the T-stress and A and B are the terms related to rigid rotation and translation. This formulation was obtained considering a cylindrical coordinate system with the origin in the crack-tip, as depicted in Fig 1.8.

Carroll et al. [2] applied the regression technique to fatigue. In order to extract the values of ΔK, they acquired several pictures of the crack during each fatigue cycle and calculated the displacements starting from the picture taken at the minimum applied

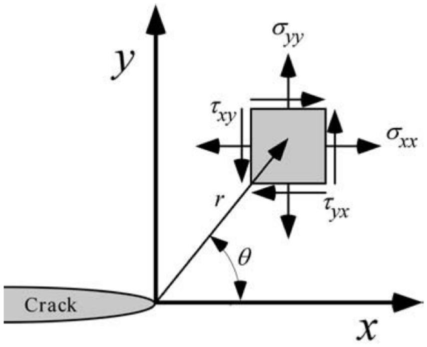

Figure 1.8: *Crack tip coordinate system.*

load: this allowed the extraction of the effective stress intensity factor range, ΔK_{eff}, since the crack-closure effect was inherently included in the displacements measured by DIC.

In Fig. 1.9a, a comparison between the experimental and the analytical vertical displacements is provided, showing that DIC is capable of measuring the singularity present at the tip and that the experimental field can be correctly fitted by the analytical one. Moreover, analyzing the evolution of ΔK during a single stress/strain cycle, it is also possible to evaluate the crack opening levels, as shown in Fig. 1.9b.

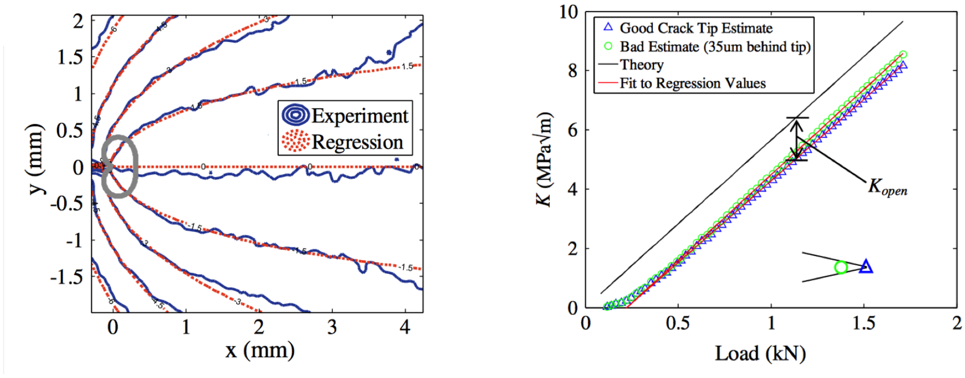

(a)

(b)

Figure 1.9: *Experimental crack-closure measurements with full-field regression [2]: a) comparison between regressed and experimental vertical displacement field; b) individuation of K_{open} during a fatigue load cycle.*

Recently, Yoneyama et Al. [59] were able to apply the regression algorithm during mixed mode propagation and to extract ΔK_I and ΔK_{II}, whereas Pataky et Al. [60] were able to analyze fatigue crack growth both at room and high temperature in Haynes 230 polycrystals.

CHAPTER 2

Short crack propagation in the LCF regime at Room and High Temperature

2.1 INTRODUCTION

Fatigue life assessment in presence of defects (inclusions, inhomogeneities, ..) is important for fatigue life design of massive components like turbine rotors and disks, which are subjected to LCF conditions. Residual life of a component subjected to cyclic loading in Low Cycle Fatigue (LCF) regime can be assessed considering a crack propagating from the first load cycle, together with an appropriate crack growth model. Traditional approaches based on Linear Elastic Fracture Mechanics (LEFM) cannot be applied in LCF, since defects usually grow in zones where high plastic strains are present, such as near notches, violating LEFM main assumptions.

In this work, fatigue crack growth in the LCF regime is investigated on three different quenched and tempered steels, usually employed for turbine disks and shafts. The main aim of this chapter is to develop a model capable of describing fatigue life in the range of 10000 cycles, the average number of start-ups and shut-downs experienced by gas turbines before maintenance inspections, taking into account environmental effects, such as temperature.

The chapter is divided into three different sections:

- In the first part of the chapter, a series of experiments performed under constant strain amplitude loading is discussed. Two different specimen geometries are tested: the results of the experiments performed on smooth cylindrical specimens are analyzed in order to evaluate the ϵ_a - N curves, whereas the tests performed on specimens with a 0.4 mm deep semi-circular defect are employed to observe short crack propagation.

- In the second part of the chapter, state-of-the-art crack propagation models are discussed. Models that describe crack propagation in terms of the applied plastic strain range are compared to those based on elastic-plastic fracture mechanics. In particular, several models based on the cyclic J-Integral range are presented, together with a discussion on the implementation of crack closure in ΔJ calculations.
- In the third and final section, experimental results are analyzed with the previously discussed models. Experimentally measured crack growth rates are compared to the reference curves obtained from tests performed on standard C(T) specimens. The effects of the temperature, together with those related to the applied mean strains, are discussed. Finally, a crack propagation model, which takes into account not only the effects of temperature, but also the transient behavior of crack closure, is implemented and checked, providing satisfactory results in terms of fatigue life assessment.

2.2 EXPERIMENTS

2.2.1 Test details

Fatigue crack growth behavior in LCF regime was investigated on three quenched and tempered CrMo steels adopted for manufacturing turbine disks and rotors. Steel #1, a bainitic steel, was tested at room temperature, since it is usually employed at low temperature, whereas steel #2 and steel #3 were tested at high temperature (490 and $500°C$ respectively), because they are commonly used for turbine disks. Steel #2 is a different bainitic steel, whereas steel #3 is a ferritic-martensitic steel.

All LCF tests were performed using a MTS 810 servo-hydraulic testing machine. An high temperature longitudinal extensometer with a 12 mm long gage was employed and temperature was obtained with induction heating. In Fig. 2.1a, the experimental setup for high temperature testing is shown. LCF tests were carried out at a frequency of $0.5Hz$.

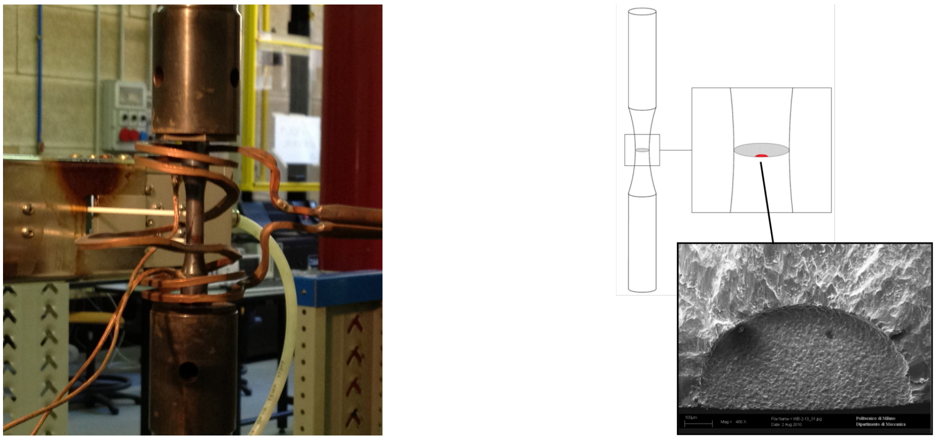

(a)

(b)

Figure 2.1: *LCF experimental tests: a) experimental setup for HT LCF tests; b) micro-notch shape and orientation (defect depth* $400\ \mu m$*).*

For each steel, two series of tests were carried out. In the first series, cylindrical specimens with a diameter of 8 mm and a gauge length of 20 mm were tested under constant strain amplitude loading at different amplitude levels, with a fixed strain ratio R = -1: Manson-Coffin curves were obtained from these datasets. In the second series, the same kind of tests were carried out on specimens containing artificial semicircular micro-notches, obtained by Electrical Discharge Machining (EDM): 400 μm depth notches were employed (Fig. 2.1b). Two additional experimental campaign were performed on steel #3 to confirm experimental observations. A new series of specimens, with an artificial defect of 100 μm, was tested at 350°C with a fixed strain ratio R = -1. Another batch of specimens was tested at 500°C with a fixed strain ratio R = 0.25 to check the influence of the applied mean strain on crack growth rates.

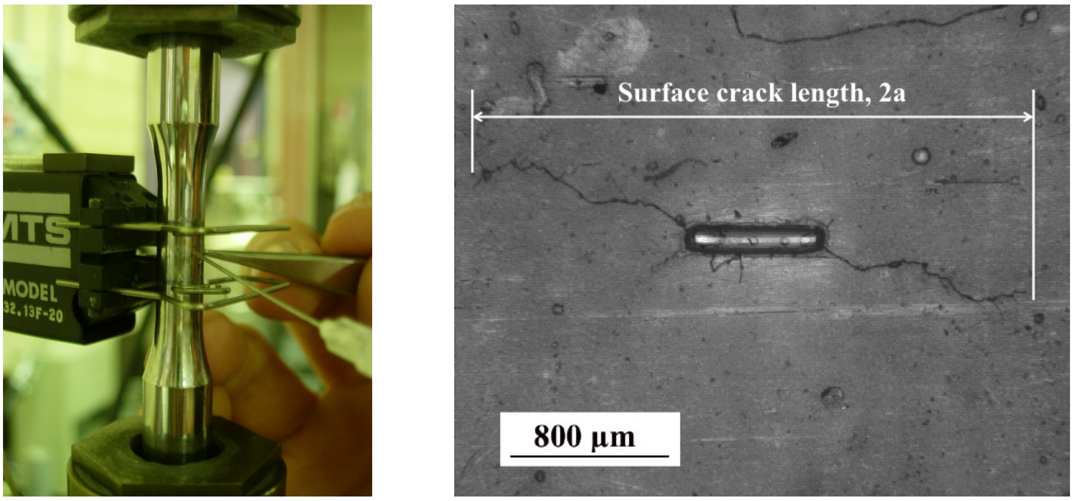

(a) (b)

Figure 2.2: *Plastic replica technique for crack length measurements during fatigue tests: a) replica preparation on the fracture surface, during a test interruption; b) surface crack propagation observed on a plastic replica, high temperature (defect depth 400 μm).*

Crack propagation in LCF experiments was measured using the plastic replicas technique. This method consists in applying on the specimen surface, during a test interruption, a thin foil of acetate. The acetate is then moistened with acetone, sprayed on the plastic foil with the needle of a syringe, as shown in Fig. 2.2a. At this point, the acetate sheet softens and assumes the shape of the fracture. After acetone evaporation, the foil regains his consistency and can be removed from the fracture surface. Finally, the replica can be placed on a slide under a microscope lens to analyze crack shape and length. An example of a so-obtained replica at high temperature is presented in Fig. 2.2b, where, starting from the artificial defect, the surface crack propagation can be observed. An important assumption made during this analysis is that cracks maintain a semi-circular shape during propagation: this was confirmed during specimens inspection after the end of the tests, since the fracture surfaces of the broken specimens exhibited a semicircular fatigue crack. Experimental crack length was plotted against cycles: da/dN data were then derived by the *secant method* and models parameters calculation was based on these growth rate data.

In order to obtain reference da/dN - ΔK curves, a series of fatigue crack growth tests was performed on compact tension (C(T)) specimens. These experiments were carried out following the constant amplitude (CA) procedure proposed in the ASTM E647 standard. Initially, a stress ratio R = 0 was employed to evaluate the propagation curve necessary for Harkegard's model. A load ratio equal to 0.7 was then employed to obtain closure-free propagation curves. During all the experiments, the load frequency was fixed at 0.5 Hz, the same frequency adopted for LCF testing. A summary of the different series of experiments is shown in Table 2.1.

Table 2.1: *Summary of the experimental tests.*

Material	T [°C]	Test method	Test control	R
		LCF - smooth specimens	Strain	-1
Steel #1	20	LCF - specimens with 400 μm defects	Strain	-1
		FCG - C(T) specimens	Load	$0-0.7$
		LCF - smooth specimens	Strain	-1
Steel #2	490	LCF - specimens with 400 μm defects	Strain	-1
		FCG - C(T) specimens	Load	$0-0.7$
	500	LCF - smooth specimens	Strain	-1
	500	LCF - specimens with 400 μm defects	Strain	-1
Steel #3	500	LCF - specimens with 100 μm defects	Strain	0.25
	350	LCF - specimens with 100 μm defects	Strain	-1
	350 - 500	FCG - C(T) specimens	Load	$0-0.7$

2.2.2 Strain life diagrams

All the experimental results at R = -1 are reported in Fig. 2.3a for steel #1, in Fig. 2.3b for steel #2 ($T = 490°C$) and in in Fig. 2.3c for steel #3 ($T = 500°C$). Solid black dots represent tests performed on smooth specimens, whereas other data points show the results of tests conducted on micro-notched specimens. The number of cycles to fracture, N_f, is the number of cycles necessary to reach a load drop of 25%, corresponding to a final crack length $a_f = 3$mm. Notched specimens were tested at four different strain levels, identified in Figs 2.3a, b and c. Due to confidentiality issues, experimental results are presented in normalized form.

As it can be observed, micro-notches cause a marked drop in fatigue life, therefore it s a very important to have engineering tools for life assessment of engineering components. The different models for crack growth under LCF will then be discussed in terms of their ability to predict the $\epsilon - N$ diagram for specimens with $a_o = 400\mu m$.

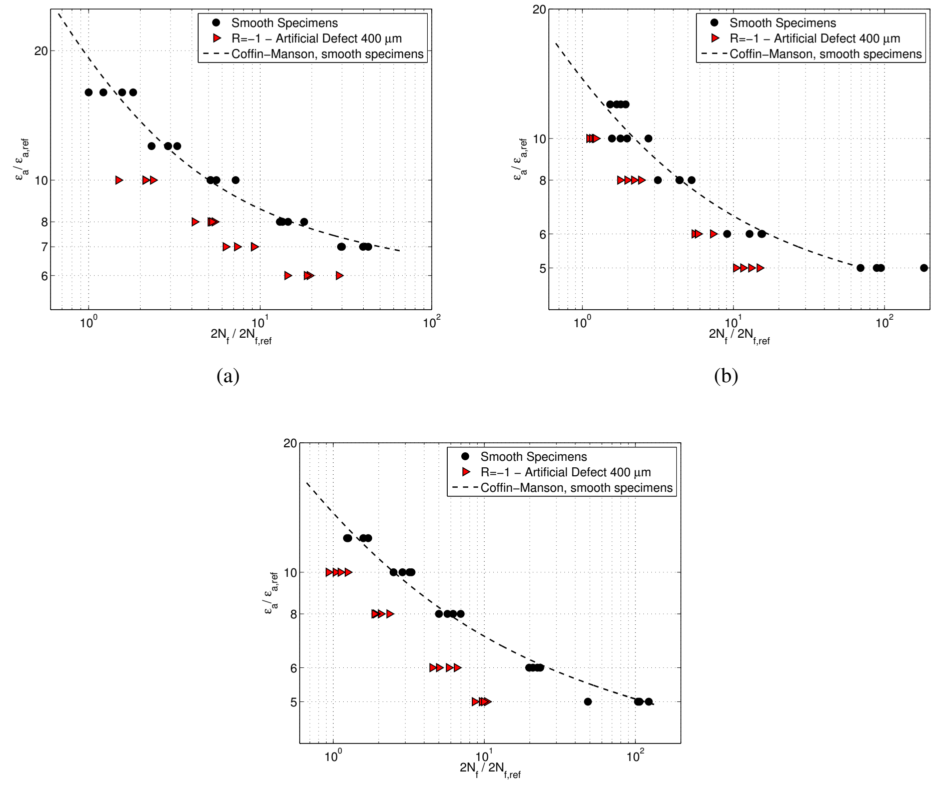

(a)

(b)

(c)

Figure 2.3: *Low Cycle Fatigue tests results. a) Steel #1, room temperature; b) Steel #2, T = 490°C; c) Steel #3, T = 500°C.*

2.3 CRACK GROWTH ANALYSIS

2.3.1 Analytical approach based on plastic strain range

Crack growth rates in LCF can be described as a function of the applied plastic amplitude, ϵ_{ap}. The main contribution in this field is the work published by Tomkins [41], who related crack growth rates to ϵ_{ap} with an exponential law. According to this model, the increase of defect size during propagation follows the exponential law proposed in Eq. 2.1, where a is the crack length observed at the N-th cycle, a_i is the initial crack length and k_g is a non-dimensional parameter which depends on the applied strain range.

$$a = a_i\, exp\,(k_g N) \tag{2.1}$$

Crack growth rates can be calculated by deriving Eq. 2.1 with respect to N: Eq. 2.2 shows that crack growth rates are proportional not only to the defect size, but also to k_g. Tomkins proposed the formulation of k_g proposed in Eq. 2.2, where k_{g0} and d are two material-related constants that can be calculated considering the Coffin-Manson curve obtained from smooth specimens testing.

$$\frac{da}{dN} = k_g a \;\; with \; k_g = k_{g0}\, \epsilon_{ap}^d \Rightarrow \frac{da}{dN} = k_{g0}\, \epsilon_{ap}^d a \tag{2.2}$$

Fatigue lives obtained at different strain ranges can be calculated by integrating Eq. 2.2, considering crack propagation from an initial length, a_0, to the final one measured at failure, a_{fin}. Following this consideration, the number of cycles to failure, N_f, can be expressed as shown in Eq. 2.3:

$$\frac{da}{a} = k_{g0}\, \epsilon_{ap}^d\, dN \Rightarrow \int_{a_0}^{a_{fin}} \frac{da}{a} = \int_0^{N_f} k_{g0}\, \epsilon_{ap}^d\, dN \Rightarrow N_f = \frac{1}{k_{g0}\, \epsilon_{ap}^d} ln\left(\frac{a_{fin}}{a_0}\right) \tag{2.3}$$

N_f can be calculated even by rewriting Coffin-Manson law, as proposed in Eq. 2.4:

$$\epsilon_{ap} = \epsilon_f^{'}\,(2N_f)^c \Rightarrow N_f = \frac{1}{2}\left(\frac{\epsilon_{ap}}{\epsilon_f^{'}}\right)^{1/c} \tag{2.4}$$

Starting from Eq. 2.3 and Eq. 2.4, k_{g0} and d can be calculated, as shown in Eq. 2.5.

$$d = -1/c, \quad k_{g0} = 2(\epsilon_f^{'})^{1/c}\, ln\left(\frac{a_{fin}}{a_0}\right) \tag{2.5}$$

Material constants determination is related to the choice of a_0 and a_{fin}. In this work, the initial defect length a_0 was chosen equal to 20 μm, since it is the average dimension of the inclusions present in the considered family of alloys. The defect final size, a_{fin}, was chosen equal to 3 mm, since it is the average crack size measured after the end of fatigue tests.

2.3.2 Elastic-plastic facture mechanics approach

Cyclic J-integral formulation

The cyclic J-integral, ΔJ, can be described as the sum of an elastic and a plastic component [31]. The elastic part, considering plane strain conditions, can be calculated starting from LEFM [61]:

$$\Delta J_e = \frac{\Delta K^2 \left(1-\nu^2\right)}{E} = \frac{\left(Y \Delta\sigma \sqrt{\pi a}\right)^2 \left(1-\nu^2\right)}{E} = Y^2 \frac{\Delta\sigma^2 \left(1-\nu^2\right)}{E} \pi a = \\ = 2\pi Y^2 \left(1-\nu^2\right) \Delta W_e a \tag{2.6}$$

where Y is a factor that accounts for crack geometry, a is the crack length, $\Delta\sigma$ is the applied stress range, E is the Young's modulus and ν is the Poisson's ratio. Consequently, ΔJ_e is a function of ΔW_e, the elastic strain energy density, evaluated as proposed in Eq. 2.7 and depicted in Fig. 2.4.

$$\Delta W_e = \frac{\Delta\sigma^2}{2E} \tag{2.7}$$

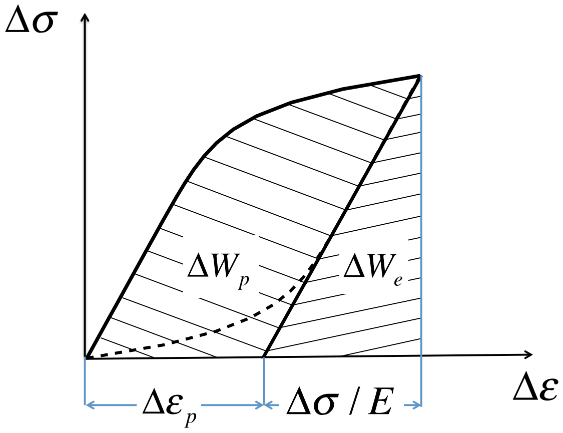

Figure 2.4: *Elastic and plastic strain energy densities employed in ΔJ calculations.*

The evaluation of the plastic part of the J-Integral range, ΔJ_p, follows the same path. Dowling postulated that ΔJ_p is proportional to ΔW_p, the plastic strain energy density [62], depicted in Fig. 2.4.

In these calculations, material plastic behavior is described by a pure power hardening law, as expressed in Eq. 2.8.

$$\Delta\epsilon = \frac{\Delta\sigma}{E} + 2\left(\frac{\Delta\sigma}{2k_i}\right)^{1/n_i} \tag{2.8}$$

Therefore, ΔW_P can be calculated as expressed in Eq. 2.9, where it is shown that the plastic strain energy density is a function of n_i, the hardening exponent, $\Delta\sigma$ and $\Delta\epsilon_p$, the plastic strain range.

$$\Delta W_p = \frac{\Delta\sigma\Delta\epsilon_p}{1+n_i} \tag{2.9}$$

Thus, ΔJ_p can be written as:

$$\Delta J_p = 2\pi Y^2 f\left(n_i\right) \Delta W_p a \tag{2.10}$$

where $f\left(n_i\right)$ is a function that takes into account crack geometry and material elastic-plastic behavior. Several formulations of $f\left(n_i\right)$ are proposed in [30] and in [31]. Following these observations, the general formulation of ΔJ can be written as:

$$\Delta J = \Delta J_e + \Delta J_p = 2\pi Y^2 a \left[\left(1-\nu^2\right) \Delta W_e + f\left(n_i\right) \Delta W_p\right] \tag{2.11}$$

Eq. 2.11 shows that ΔJ is a function of both elastic and plastic strain energy density, a feature that makes the J-integral range a parameter capable of measuring the characteristic crack-tip strain field. This means that, in elastic-plastic fracture mechanics, ΔJ can play the same role of the stress intensity factor range, ΔK, in LEFM [62]. Moreover, following this description, ΔJ can be computed directly from the hysteresis loops, by fitting the upper branch of the stress/strain fatigue cycle with the Ramberg-Osgood equation, as shown in Fig. 2.4. This definition is in line with the $Z - integral$ concept presented in [63].

The ΔJ formulations proposed by Polak [32] and Harkegard [33] are here reported. For the given geometry, Polak modified Eq. 2.11, proposing the formulation:

$$\Delta J = \frac{\Delta K^2}{E} + 1.72 g\left(n_i\right) \sigma_a \epsilon_a a \tag{2.12}$$

where σ_a and ϵ_a are stress and strain amplitudes, ΔK is the stress intensity factor range and $g\left(n_i\right)$ is evaluated as [30]:

$$g\left(n_i\right) = \left(1 - n_i\right)\left(3.85\sqrt{\frac{1}{n_i}}\left(1 - n_i\right) - \pi n_i\right) \tag{2.13}$$

Even Harkegard's formulation is derived directly from Eq. 2.11 and, for the given geometry, is expressed as:

$$\Delta J = Y^2 \pi a \Delta\sigma\left(\Delta\epsilon_e + 2\Delta\epsilon_p\right) \tag{2.14}$$

Effective cyclic J-Integral formulation

Starting from Dowling's proposal [26], effective elastic-plastic J-Integral range is calculated by considering the part of the stress/strain cycle in which the crack stays open. Two different proposals, formulated by Vormwald and Seeger [3, 35] and McClung and Sehitoglu [4, 34] can be found in the literature.

In these models, crack opening stress is calculated from Newman's equations (see section 1.2.2 [5]). Experimental results, reported in [3, 34], showed that, during LCF propagation, a satisfactory estimate of crack opening levels can be obtained by considering plane stress (i.e. $\alpha = 1$), since significant out-of-plane constraint is less likely under general yielding [34]. The cyclic flow stress, a parameter necessary for the calculation of crack opening stress in Newman's model, is estimated as the average of the cyclic yield stress and the ultimate strength [64].

The main difference between the models is the evaluation of crack opening and closing levels. Vormwald and Seeger [3], observed that, during LCF propagation, crack opening and closing occurs at the same strain level. Therefore, according to this model, σ_{cl}, the crack closing stress, is lower than σ_{open}. This implies that, according to Vormwald and Seeger, the effective stress range should be calculated as proposed in Eq. 2.15:

$$\Delta\sigma_{eff} = \sigma_{max} - \sigma_{cl} \tag{2.15}$$

where σ_{max} is the stress peak value.

Following these experimental observations, the part of the stress-strain cycle considered for ΔJ-calculation is represented by the hatched area in Fig. 2.5a, where a summary of the significant points of Vormald and Seeger′s model is also depicted. For the given geometry, ΔJ_{eff} can be evaluated as [3]:

$$\Delta J_{eff} = a\left[1.24\frac{\Delta\sigma_{eff}^2}{E} + \frac{1.02}{\sqrt{n_i}}\Delta\sigma_{eff}\Delta\epsilon_{p,eff}\right] \tag{2.16}$$

where a is crack length, E is Young's modulus, n' is the exponent of the cyclic stress-strain curve, $\Delta\sigma_{eff}$ and $\Delta\epsilon_{p,eff}$ are, respectively, the effective stress range and the effective plastic strain range. $\Delta\epsilon_{p,eff}$ is calculated as proposed in Eq.2.17, where $\Delta\sigma_{eff}$ is computed as reported in Eq. 2.15.

$$\Delta\epsilon_{p,eff} = \Delta\epsilon_{eff} - \frac{\Delta\sigma_{eff}}{E} \tag{2.17}$$

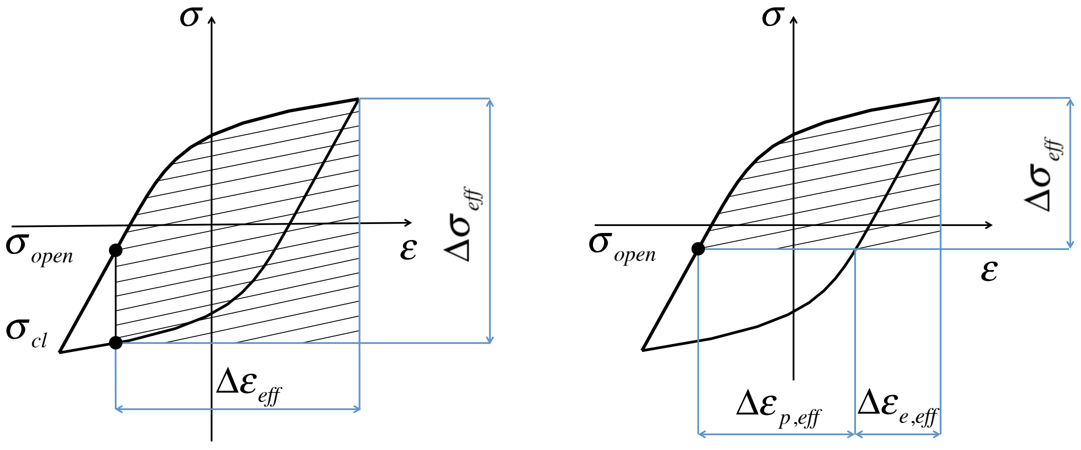

(a)

(b)

Figure 2.5: *Definition of the significant part of the stress/strain cycle for ΔJ_{eff}. a) Seeger and Vormwald [3]. b) McClung and Sehitoglu [4].*

On the other hand, McClung and Sehitoglu assumed that crack opening and closing occur at the same stress level: this means that the portion of the fatigue cycle considered in ΔJ-calculations is represented by the hatched area of Fig. 2.5b. For the given geometry, McClung and Sehitoglu [4] proposed the formulation shown in Eq.2.18, where $h\left(n_i\right)$ is calculated according to Eq.2.19 [30] and $\Delta\sigma_{eff} = \sigma_{max} - \sigma_{open}$.

$$\Delta J_{eff} = 1.25a\left[\frac{\Delta\sigma_{eff}^2}{E} + \frac{h\left(n_i\right)}{\pi}\Delta\sigma_{eff}\Delta\epsilon_{p,eff}\right] \tag{2.18}$$

$$h\left(n_i\right) = 3.85\left(1 - n_i\right)\sqrt{1/n_i} + \pi n_i \tag{2.19}$$

Effective J-Integral formulation based on the limit load theory

According to european SINTAP/FITNET procedure, elastic-plastic J-Integral is related to the elastic stress intensity factor, through a function, $f\left(L_r\right)$, which describes the yielding status of the ligament:

$$f\left(L_r\right) = \left[\frac{E\cdot\epsilon_{ref}}{L_r\cdot\sigma_Y} + \frac{L_r^3\cdot\sigma_Y}{2\cdot E\cdot\epsilon_{ref}}\right] \tag{2.20}$$

where L_r is the ratio between the applied load and the load which causes section plastic collapse, E is Young's modulus, σ_Y is the cyclic yielding stress and ϵ_{ref} is the strain at which yielding occurs.

The relationship between elastic-plastic J-integral and elastic stress intensity factor range is shown in Eq. 2.21:

$$J = \frac{K^2}{E}\left[f\left(L_r\right)\right]^{-2} \tag{2.21}$$

Eq. 2.20 has been modified [40] to take into account cyclic loading and crack-closure, substituting L_r with ΔL_r, as proposed in Eq. 2.22:

$$\Delta L_r = \frac{\Delta\sigma_{eff}}{2\sigma_Y} = \frac{\sigma_{max}-\sigma_{cl}}{2\sigma_Y} \tag{2.22}$$

Following these changes, the effective J-integral range can be calculated as:

$$\Delta J_{eff} = \frac{\Delta K_{eff}^2}{E}\left[f\left(\Delta L_r\right)\right]^{-2} \tag{2.23}$$

where, for the given geometry,

$$\Delta K_{eff} = 2\frac{1.12}{\pi}\Delta\sigma_{eff}\sqrt{\pi a} \tag{2.24}$$

Data analysis and comparison of the models

In order to extract the effective J-integral range, all the experimental datas were analyzed considering experimental stresses and strains extracted from the stabilized stress/strain loop, taken at $N_f/2$. The upper branch of the fatigue load cycle was fitted with the Ramberg-Osgood equation proposed in Fig. 2.4: this allowed the direct estimation of ΔJ from the hystheresis loops, following Dowling's initial proposal.

The different models have then been compared in terms of description of the estimated $da/dN - \Delta J$ (or $da/dN - \Delta J_{eff}$ data) and their ability to predict the $\epsilon - N$ diagram for specimens with defects. In particular, for the differently estimated da/dN curves, life prediction for micronotched specimens have then been calculated as:

$$N_f = \int_{a_o}^{a_f}\frac{1}{da/dN}da \tag{2.25}$$

assuming $a_o = 400\mu m$ (cracks grew from the micronotches almost from the first load cycle) and $a_f = 3\,mm$ (average crack depth for the broken specimens).

2.4 RESULTS AND DISCUSSION

2.4.1 LCF tests at Room Temperature

Experimental results for steel # 1 were compared with those provided by Tomkins' model in Fig. 2.6, where crack growth rates are plotted against crack lengths: the model correctly predicts crack growth rates only when high plastic strains are present (Fig. 2.6a), whereas loses accuracy at low strains (Fig. 2.6b). This is related to the main assumptions of the model, since it considers only the plastic part of the applied strain range. The same observations can be made considering fatigue life assessment, as proposed in Fig. 2.6c: the model proposed by Tomkins provides conservative estimates only at high strain amplitudes, providing unconservative assessments when the plastic strain amplitude tends to zero. This means that a fatigue life assessment, obtained considering $\Delta\epsilon_p$-based models, is conservative only in presence of high plastic strains and not in the range of 10000-20000 cycles, which is the target for turbine disks.

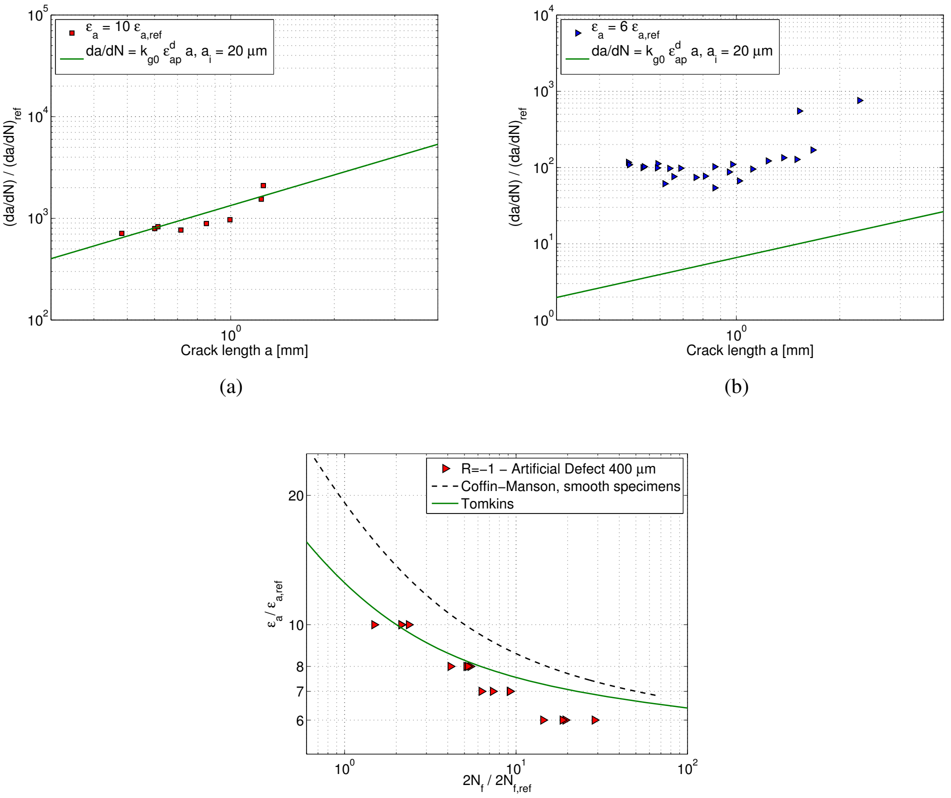

(a)

(b)

(c)

Figure 2.6: *Fatigue crack growth analysis based on Tomkins model, steel #1 at room temperature: a) Comparison between experimental and predicted crack growth rates, high strain amplitude; b) Comparison between experimental and predicted crack growth rates, low strain amplitude; c) Fatigue life prediction for micronotched specimens (a_0 = 400 μm).*

At this point, experimental data-points were analyzed considering the propagation models based on ΔJ. In Fig. 2.7a experimental results are reported in terms of crack growth rates for steel #1, considering Polak's formulation (Eq. 2.12). This model introduces a large scatter, a feature present even when Harkegard's formulation (Eq. 2.14) is considered (Fig. 2.7b): this is due to the fact that models based on the cyclic J-integral range neglect the effects of crack closure during propagation.

The experimental points, obtained considering Polak's and Harkegard's formulations, can be fitted by a modified Paris law (Eq. 2.26):

$$\frac{da}{dN} = c \cdot \Delta J^m \tag{2.26}$$

where c and m parameters were estimated by a least squares interpolation of experimental data points. Fatigue life was estimated from Eq. 2.26 adopting these parameters.

The results in terms of fatigue life prediction, obtained considering Polak's formulation, are represented in Fig. 2.7c by a light gray line: the scatter observed in Fig. 2.7a is responsible for the unconservative assessment, in particular for those tests performed at high strain ranges whose experimental growth rate data are higher than the average $da/dN - \Delta J$ curve.

Much better results could be obtained with Harkegard's model. In details, in order to obtain conservative estimates, the author [33] suggested to consider the crack propagation curve obtained testing fracture specimens at R = 0 (the dark grey line in Fig. 2.7b). As it can be seen, this propagation curve is an upper bound for the experimental data-points. This means that a fatigue life prediction based on Harkegard's formulation (the dark gray line in Fig. 2.7c) is conservative for all the considered strain ranges. Such an approach, however, provides very conservative results (in a factor 3) at low strain levels.

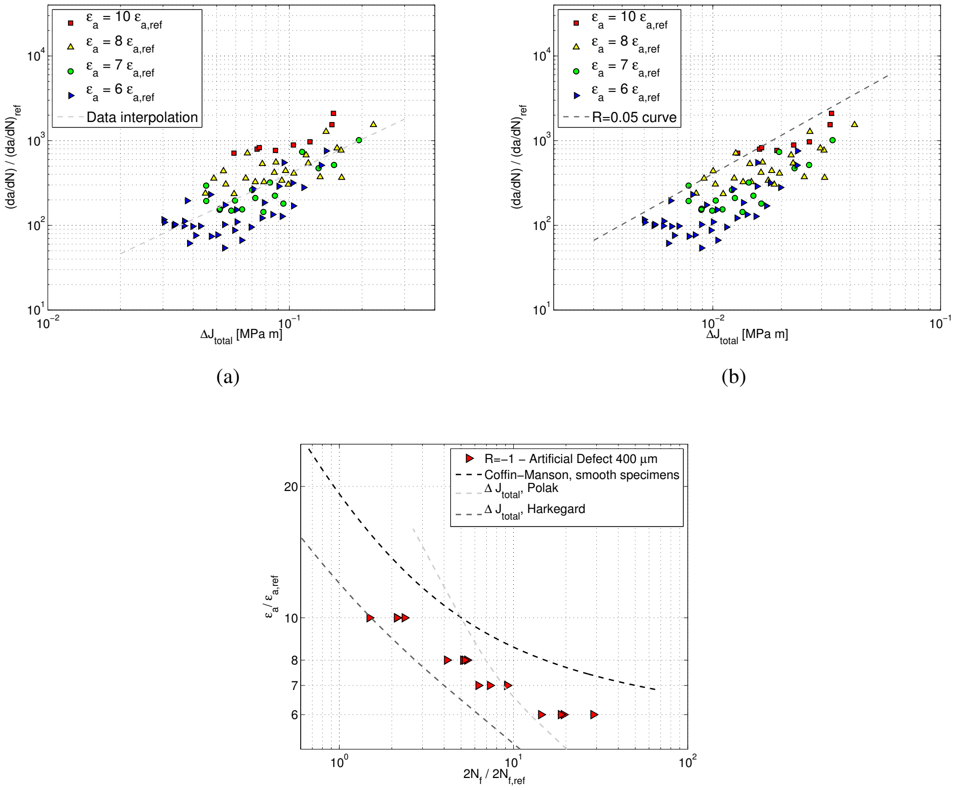

(a) (b)

(c)

Figure 2.7: *Fatigue crack growth analysis based on ΔJ_{tot}, steel #1 at room temperature: a) Crack growth rates vs. ΔJ_{tot} according to Polak; b) Crack growth rates vs. ΔJ_{tot} according to Harkegard; c) Fatigue life prediction for micronotched specimens ($a_o = 400\,\mu m$).*

At this point, crack propagation models based on ΔJ_{eff} (Eq. 2.16 and Eq.2.18) were implemented. Models were modified to take into account that, in the early propagation stage, cracks are open even at the minimum applied load. This phenomenon, observed in [34], is due to the transient build-up of crack-closure and can be implemented by considering the model by McEvily [65] as proposed in [40]. This model describes crack opening load, as dependent on crack advance as:

$$\sigma_{open,tr} = \sigma_{min} + (\sigma_{open} - \sigma_{min}) \left\{ 1 - exp \left[-k_{op} (a - a_o) \right] \right\} \tag{2.27}$$

where k_{op} is a material dependent constant and a_o is initial notch size. This parameter was estimated interpolating experimental data and it has resulted to be close the value obtained in [40].

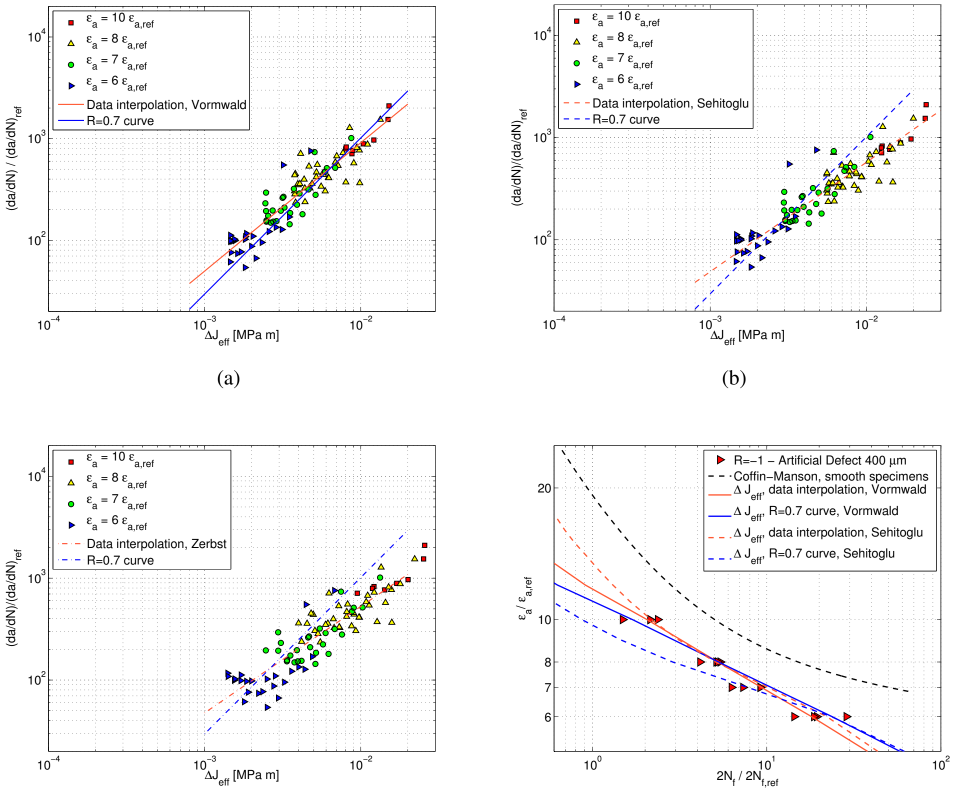

(a)

(b)

(c)

(d)

Figure 2.8: *Fatigue crack growth analysis based on ΔJ_{eff}, steel #1 at room temperature: a) Crack growth rates vs. ΔJ_{eff} according to Vormwald; b) Crack growth rates vs. ΔJ_{eff} according to Sehitoglu; c) Crack growth rates vs. ΔJ_{eff} according to Zerbst; d) Fatigue life prediction for micronotched specimens ($a_o = 400\,\mu m$).*

Final results for steel #1 in terms of crack growth rates, obtained considering ΔJ_{eff} (Eq. 2.16 and Eq. 2.18), are reported in Fig. 2.8a and b: experimental points tend to move on a single line and a much smaller scatter is observed. In the same pictures, experimental results are compared with the reference $da/dN - \Delta K_{eff}$ curve, obtained testing C(T) specimens at high load ratio (R = 0.7). As it can be seen, experimental points are very close to the $da/dN - \Delta K_{eff}$ curve: this is due to the fact that models based on ΔJ_{eff} consider and remove crack closure effects.

The same trend can be observed when the formulation proposed by Zerbst (Fig. 2.8c) is considered, even if a bigger scatter is introduced. Because of this, only the formulations proposed by Vormwald and Sehitoglu were considered for the prediction of the $\epsilon - N$ curve for micronotched specimens. Fatigue life assessments are reported in Fig. 2.8d, in which the dashed lines represent the estimates obtained considering Eq. 2.18, whereas the continuous ones represent the assessment obtained by adopting Eq. 2.16. The model proposed by Vormwald and Seeger provides more accurate estimates and it is able to correctly predict the slope of the R = 0.7 curve in the da/dN-ΔJ_{eff} diagram: because of this, in the following calculations, only Vormwald and Seeger's model will be considered. It is also worth remarking that the predicted $\epsilon - N$ curve, due to the improvement offered by Eq. 2.27, is very close to experimental results (both considering $da/dN - \Delta J_{eff}$ average interpolation or $da/dN - \Delta K_{eff}$ curve) also at very low strain amplitudes, where $\Delta\epsilon_p$ becomes negligible. This means that ΔJ_{eff} models are able to describe well fatigue life also in the region, very interesting for engineering applications like turbines whose target life is 10000-20000 cycles, a condition in which Tomkins' model provides unconservative estimates.

At this point, Vormwald's model was employed to estimate fatigue life of smooth cylindrical specimens. Assuming an initial defect size of $20\mu m$, the average size of the inhomogeneities present in unnotched specimens and also the initial crack length employed in Tomkins calculations, and considering the experimentally obtained c and m constants, the model was able to correctly assess fatigue life even in case of smooth specimens, as shown in Fig. 2.9.

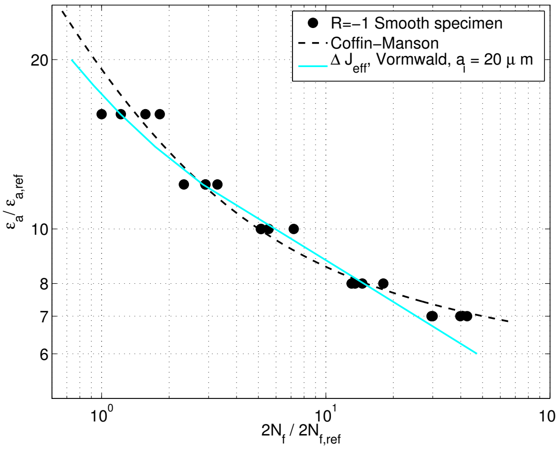

Figure 2.9: *Fatigue life prediction for smooth specimens with ΔJ_{eff}(Eq.2.16).*

2.4.2 LCF tests at High Temperature

The analysis of fatigue crack growth at room temperature underlined the fact that the model proposed by Tomkins accurately describes crack growth rates and provides conservative fatigue life assessments only when high plastic strain are present. The same observations can be made even at high temperature: considering steel #2, experimentally measured crack growth rates are in good agreement with those analytically calculated, only when high strain amplitudes are applied (Fig. 2.10a), whereas wrong estimates are obtained when low strain amplitudes are considered (Fig. 2.10b). Consequently, the model is not capable of providing conservative fatigue life predictions when the applied plastic strain amplitude tends to zero, as shown in Fig. 2.10c. The same trend can be observed even for steel # 3: this means that Tomkins' model is consistent, providing the same trend in fatigue life assessment, even if different temperatures are considered. The model, however, is not suitable for the loading conditions investigated in this chapter, since it provides wrong estimates when a target life of 20000-30000 cycles is considered.

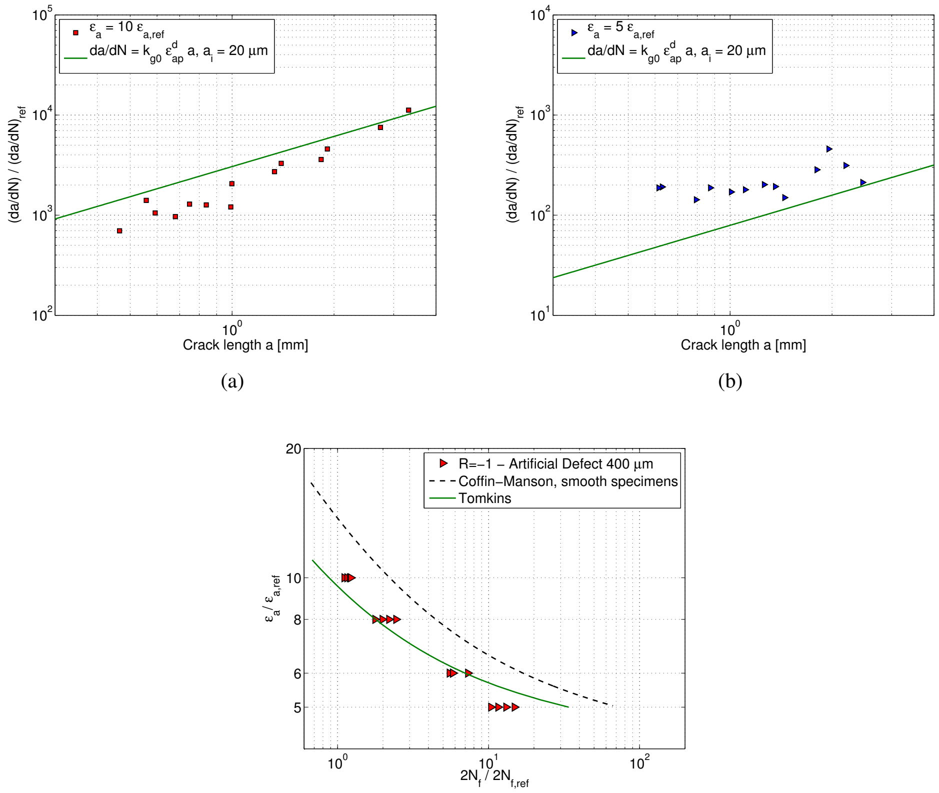

(a)

(b)

(c)

Figure 2.10: *Fatigue crack growth analysis based on Tomkins formulation, steel #2 at T = 490 °C: a) Comparison between experimental and predicted crack growth rates, high strain amplitude; b) Comparison between experimental and predicted crack growth rates, low strain amplitude; c) Fatigue life prediction for micronotched specimens (a_0 = 400 μm).*

At this point, experimental data-points obtained at HT were analyzed following the EPFM approach, considering only the model based on ΔJ_{eff} (Eq. 2.16), since it has proven to be very precise. Experimental results for steel #2 and #3 are shown in Figs 2.11 and 2.12. At high temperature, fatigue crack growth rates measured in notched specimens do not match with those observed in C(T) testing, as shown in Figs 2.11a and 2.12a. A marked speed increment is evident for all the considered models, meaning that fatigue life prediction based on $da/dN - \Delta K_{eff}$ curves can lead to unconservative results, as shown in Figs. 2.11b and 2.12b, where fatigue life estimates are reported.

The presence of the speed increment was confirmed even by the tests performed at R = 0.25 on steel #3 at 500°C (Fig. 2.13a): experimental data points obtained testing specimens with an applied mean strain, lie on the same line of those tested at R = -1. This confirms the enhanced crack growth at 500°C.

Another series of tests at 350°C were carried out on steel #3, in order to check a

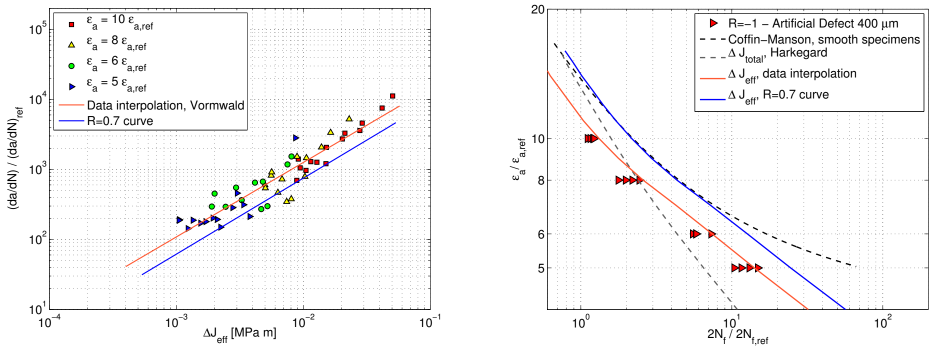

(a) (b)

Figure 2.11: *Fatigue crack growth analysis for steel #2, T = 490°C. a) Crack growth rates against effective J-Integral range, Vormwald; c) Fatigue life prediction for micronotched specimens (a_o = 400 μm), Vormwald.*

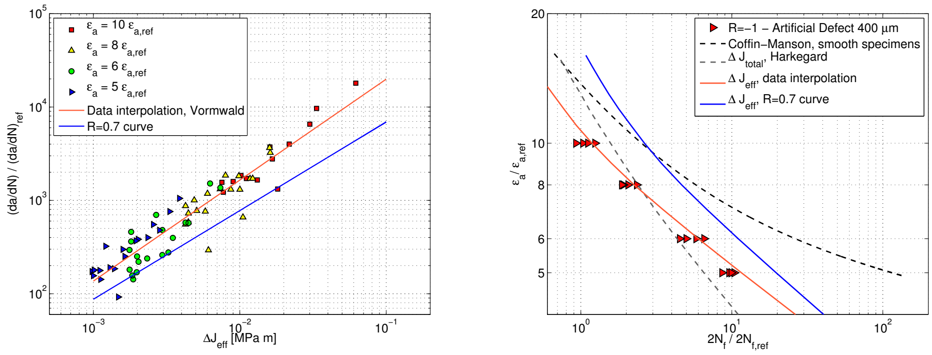

(a) (b)

Figure 2.12: *Fatigue crack growth analysis for steel #3, T = 500°C. a) Crack growth rates against effective J-Integral range, Vormwald; c) Fatigue life prediction for micronotched specimens (a_o = 400 μm), Vormwald.*

possible temperature dependence of the crack growth rates increment. Results for the new series are shown in Fig. 2.13b: the $da/dN - \Delta J_{eff}$ data are only slightly higher than the ΔK_{eff} curve, but the growth enhancement tends to disappear and it is much lower than the scatter of the data.

The fact that at high levels of ΔJ the growth rate of small cracks is higher than the one of long cracks was already noted by Earthman [66] in LCF tests similar to the present results (steel similar to #3 tested at 600 °C), who attributed it to an increased contribution of plastic deformation at the crack tip. Fractographic analyses of crack surface give a more robust explanation for the registered speed increment: in Fig. 2.14, a comparison between low temperature (350°C) and high temperature (500°C) fracture for steel #3 is shown. As it can be seen, at 500°C several micro-cracks are present, propagating from defect main body. Moreover, at high temperature, the material presents a damaged area ahead of the crack tip, meaning that, at high temperature, the material is damaged even before crack propagation. The shape of the fracture surface at

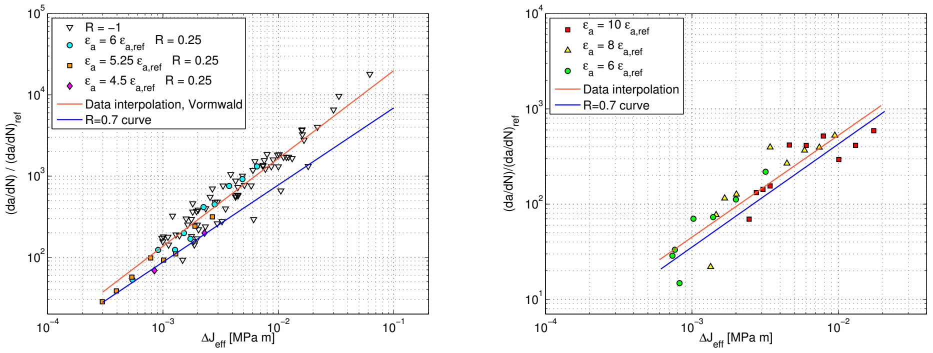

(a) (b)

Figure 2.13: *Additional tests for steel #3: a) tests at R = 0.25, T= 500°C; b) tests at R = -1, T= 350°C.*

500°C shows that the crack doesn't follow a straight pattern, but propagates in weak regions at grain boundaries for steel #3 [67]. After testing, the specimens surface was mechanically polished, in order to remove the superficial oxide layer: as it can be seen in Fig. 2.14c, the micro cracks present around the main crack body are not present only in the oxide layer, but propagate even under the surface. Crack growth rates increment is then significant at 500°C because of this damage mechanism ahead of the crack tip: this possibly explains why the enhanced growth rate is temperature dependent. Oppositely, experiments on long cracks for a steel with the same composition as #3 [68] have shown that crack surface oxidization at high temperature tends to increase the closure level (respect to an inert atmosfere) and to increase ΔK_{th}.

Fractographic observations confirmed a similar damage mechanism also for steel #2, as shown in Fig. 2.15, even though the patterns of microcracking looks to be different. The crack tends to follow a steeply pattern and, all around the crack main body, several micro cracks, extending both in the horizontal and vertical direction, are present, as depicted in Fig. 2.15a. The presence of this pattern, which can be related to stress biaxiality or thermal fatigue, was present even in the case of the specimens tested without replica interruptions, meaning that the thermal load cycles were not the main cause of this phenomenon. At this point, the oxide layer was removed from the specimen surface, in order to check if the damage mechanism was a surface one. In Fig. 2.15b, crack profile after oxide removal is reported. It is worth remarking that the stepway pattern is present even under the oxide layer, meaning that this damage mechanism does not occur only on specimens surfaces, possibly explaining the observed increment in crack growth rates.

It is of some importance also to remark that Harkegard's model, which usually provides conservative results (see Fig. 2.7c), underestimates the life at the higher strain amplitudes both for steel #2 and steel #3 (see dashed grey line in Figs 2.11b and 2.12b). This confirms the systematic crack growth acceleration at evidenced by the $da/dN - \Delta J_{eff}$ graphs and the need of incorporating this *enhanced short crack growth* into life prediction.

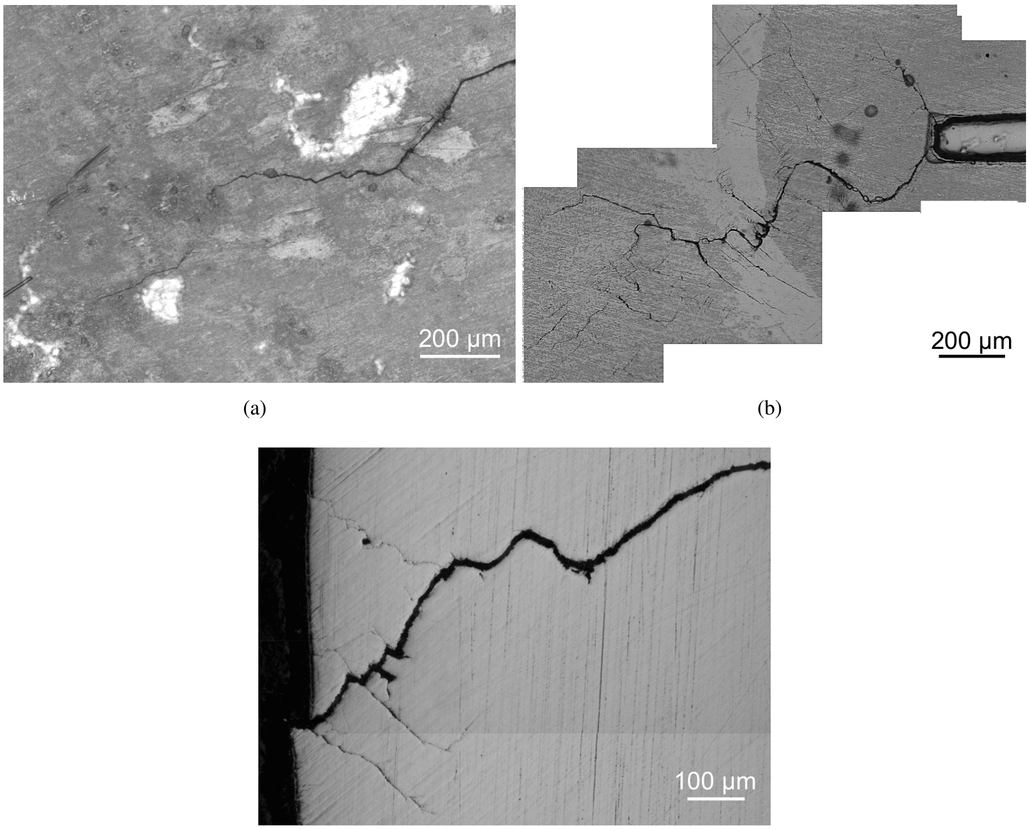

(a) (b)

(c)

Figure 2.14: *Comparison between fracture surfaces at different temperatures, steel #3. a) Steel # 3, T=350°C; b) Steel # 3, T = 500°C; c) Steel # 3, T = 500°C after surface polishing.*

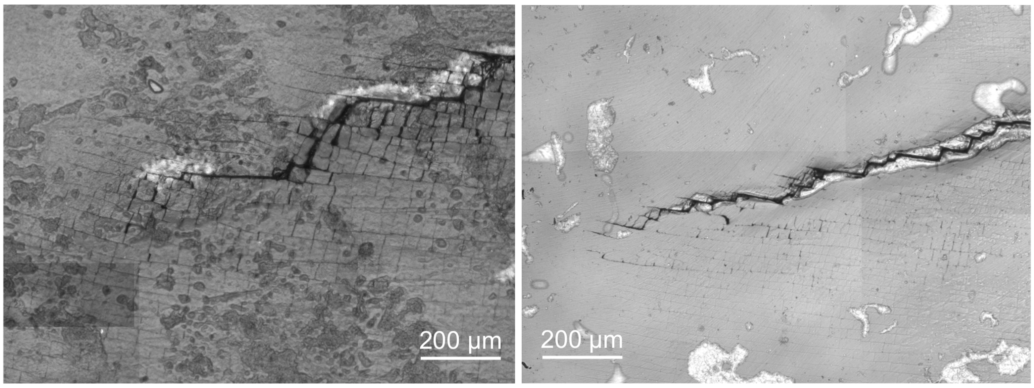

(a) (b)

Figure 2.15: *Comparison between fracture surfaces at different temperatures, steel #2. a) Steel # 2, T=490°C; b) Steel # 2, T = 490°C, after surface polishing.*

2.4.3 Correction of growth rate for damage at the crack tip

Summarizing results on steel #3, an average speed factor s_f could be expressed as:

$$s_f = \frac{(da/dN)_{exp}}{(da/dN)_{R=0.7}} \tag{2.28}$$

where da/dN_{exp} is the experimental growth rate and $da/dN_{R=0.7}$ is the growth obtained from long crack at R = 0.7. In particular data were interpolated with Eq. 2.26 power law and the s_f factor was evaluated on the interpolating curve at the mean value of ΔJ_{eff} range (its scatter was similarly evaluated from 5% and 95% percentiles of the experimental data). The s_f factor is shown in Fig. 2.16, where it is clear that the enhanced growth rate can be neglected for temperatures below 300°C (the scatter at RT was taken from data of *steel* #1).

The meaning of this speed factor is that, for a correct life estimation based onto ΔJ_{eff}, the growth rate *effective curve* (the $da/dN - \Delta K_{eff}$ curve) should be multiplied by s_f.

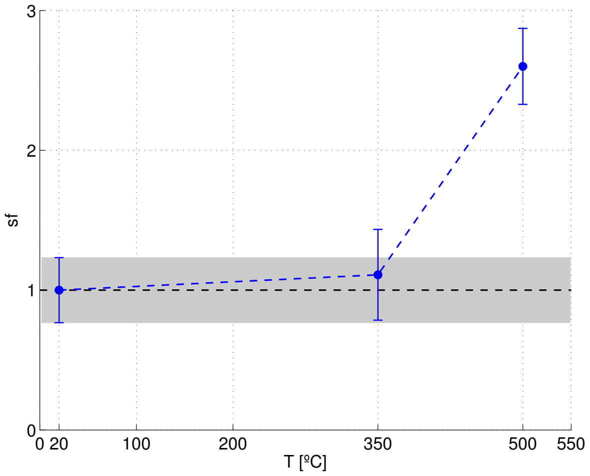

Figure 2.16: *Speed increment factor against testing temperature together with 90% scatter band ($5\% - 95\%$ percentiles): the grey area corresponds to the scatter evaluated at RT for steel #1.*

2.5 CONCLUSIONS

In this chapter, the methods for predicting LCF fatigue life in presence of micro-defects for three Q & T CrMo rotor steels have been investigated. LCF tests at different temperatures were carried out on different cylindrical specimens: smooth samples were employed for Coffin-Manson curve evaluation, whereas notched specimens were used to measure crack growth rate.

Two different approaches were implemented and checked against experimental crack growth rates and predictions of the $\epsilon - N$ diagram. The first approach, based on the work published by Tomkins, showed that models, which consider crack propagation as a function of the applied plastic strain range, give conservative estimates only when the plastic part of the total applied strain is important, whereas unconservative assessments are provided when the applied plastic strain range tends to zero. This means that models based on $\Delta\epsilon_p$ can be used to assess fatigue life only when very high strains are present.

A second approach, based on elastic-plastic fracture mechanics, was considered. Five different J-integral models (two based onto ΔJ and the other three onto ΔJ_{eff}) were implemented and checked against experimental crack growth rates and predictions of the $\epsilon - N$ diagram. The $da/dN - \Delta J$ data obtained with the formulation proposed by Polak were affected by a large scatter. This scatter was then responsible for inaccurate fatigue life predictions, in particular when high plastic strains were applied. Even Harkegard's model provided scattered data, but the proposed growth curve (obtained from $da/dN - \Delta K$ data at R = 0) gave a conservative description of the growth rate. In terms of $\epsilon - N$ diagram, such an approach provided conservative results, especially at low strain amplitudes.

Taking into account crack-closure effects, ΔJ_{eff}-based models were able to condense the growth rate onto a single $da/dN - \Delta J_{eff}$ curve. At room temperature this propagation curve matched with the one obtained from tests conducted on compact tension specimens at $R = 0.7$. At high temperature a marked speed increment was observed. An accurate analysis of the fracture surfaces showed that a peculiar damage mechanism, which consists of a diffuse cracking ahead of the crack tip, was present at high temperature. The phenomenon was temperature dependent, since experimental tests performed at lower temperatures did not show the same damage mechanism. The presence of this damage ahead of short cracks makes it necessary to adopt a suitable crack growth rate correction factor, otherwise the models would provide unconservative life estimates at high temperature.

CHAPTER 3

Short crack propagation in the dovetail attachment of a compressor disk

3.1 INTRODUCTION

In this chapter, fatigue crack growth in the blade attachment of a compressor disk of a turbogas machine is investigated. Nowadays, gas turbines are widely adopted, since they require very short times to reach the base-load condition, a situation that makes them the preferable choice for the energy industry: because of this, turbogas are usually employed to meet the peak loads requested by users; as a consequence, each plant component withstands, in its lifetime, several start-up and shut-down cycles, up to 10000 cycles without significant maintenance actions. This cyclic loading may induce plastic deformations in some critical regions of the components, such as near notches.

Talking about the design of massive turbine components, such as disks and shafts, it is also necessary to consider that, due to the technological processes (forging and machining) and fretting damages, micro-defects and damages can be present inside the components. Accordingly, the correct approach to face the design problems of these massive components is the ‘Flaw Tolerant’ approach.

It should also be considered that, before service, each machine is usually tested at a speed significantly higher than the nominal one, in order to test each component with a significant safety margin. The initial overload may cause yielding in critical regions, such as notches. In this situation, the material response, registered during nominal in-service conditions, is consequently different form the response of a component loaded only at nominal conditions, without first having endured an overload.

Taking into account all these observations, an experimental and numerical activity was performed. The main aim of this work is to discuss the effects of a plastic strain gradient during the fatigue crack growth of short cracks. The results presented and discussed in this chapter are summarized into three different sections:

- In the first part, the results of a numerical simulation of the compressor disk of a gas turbine are presented. In particular, the stress field present in the dovetail attachment of the blades is investigated. Material elastic-plastic behavior is considered: both isotropic and kinematic hardening are taken into account during the simulations, in order to provide a correct estimation of the evolution of the stress field during cycling.

- In the second part of the work, the procedure followed to design a companion specimen is discussed. The companion specimen is a sample designed to reproduce, in its thickness, the plastic strain gradient observed in the most critical part of the component, considering only a single axial force. The advantages of employing this new specimen geometry are related to the fact that testing this configuration is a cost efficient solution, since it avoids the use of full scale disks.

- In the third and final part of the chapter, the experimental results obtained testing the companion specimens are reported and compared to the numerical results calculated by applying a modified crack propagation model, based on the effective stress intensity factor ranges.

3.2 COMPANION SPECIMEN DESIGN

3.2.1 Numerical analysis of the stress field acting at the dovetail attachment of the compressor disk of a gas turbine.

In this section, the description of the numerical model, implemented to describe the stress field acting at the root of the blade attachment of a compressor disk, is presented. The FEM solver employed for calculations was Abaqus/CAE, release 6.12. The model used during this analysis is reported in Fig. 3.1a: in order to reduce computation time, all the present symmetries were taken into account. This allowed to consider only a small angular section of the total geometry, equivalent to $1/33^{th}$ of the disk. Talking about boundary conditions, radial symmetry conditions were applied on the symmetry planes, whereas a contact constraint was imposed between the blade and the disk. Contact was modeled considering the small sliding formulation, in order to reduce numerical issues. Contact normal behavior was modeled with the $hard-contact$ formulation implemented in Abaqus, whereas tangential behavior was considered by adopting a friction coefficient equal to 0.3. The only load considered in the model was the one associated to rotational body forces.The mesh was refined around the attachment, as shown in Fig. 3.1b, in order to increase the accuracy of the model: 10-nodes quadratic tetrahedral elements were adopted, with a minimum element size equal to 2 mm.

In order to correctly represent material cyclic response at the first overyielding loads, material cyclic behavior was modeled using a combined cyclic elastic-plastic model, which considered both isotropic and kinematic hardening. Isotropic hardening was assumed through the Voce equation [69], while kinematic hardening was modeled with the non-linear Chaboche model [70] considering 5 backstresses.

The load steps were set to reproduce the real load condition of the disks, considering rotational body forces, consequence of the rotational speed, as the main load. The first

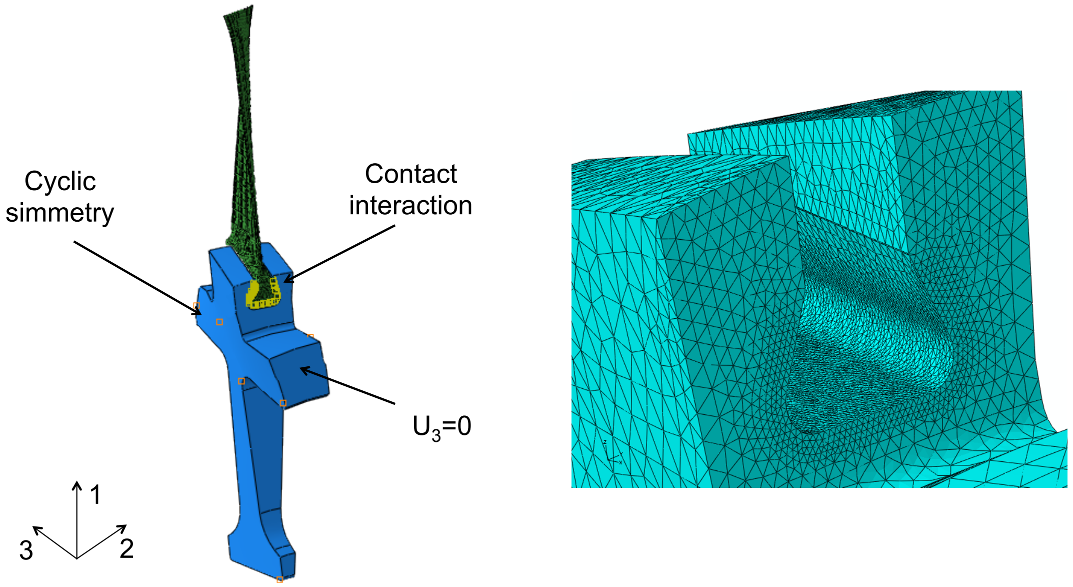

(a) (b)

Figure 3.1: *Finite element analysis of the compressor disk of a gas turbine. a) FEM model with boundary conditions; b) Refined mesh at the root of the blade attachment.*

step, as in Fig 3.2, implements the overspeed due to the spinning test (O→A→B), whereas the following cycles reproduce two start-ups and shut-downs performed at nominal speed (B→ $A^I \rightarrow B^I$).

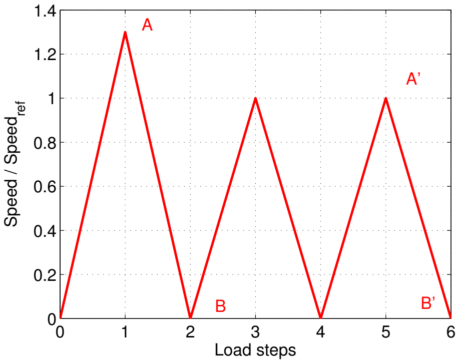

Figure 3.2: *Load steps implemented for representing the initial overspeed (spinning test) followed by nominal speed cycles.*

The results of the FEM analysis of the disk are shown in Fig. 3.3. Due to confidentiality issues, all the results are presented in a normalized form. The first cycle, performed with an increased rotational speed, induces a plastic strain field at the root of the blade attachment, as depicted in Fig. 3.3a. During unloading, the yielding condition is not met: because of this, residual compressive stresses are present at the end of the first cycle, as shown in Fig. 3.3b. The presence of the local stress field induces a shakedown condition [71]: the following cycles, performed at nominal speed, exhibit a completely elastic behavior.

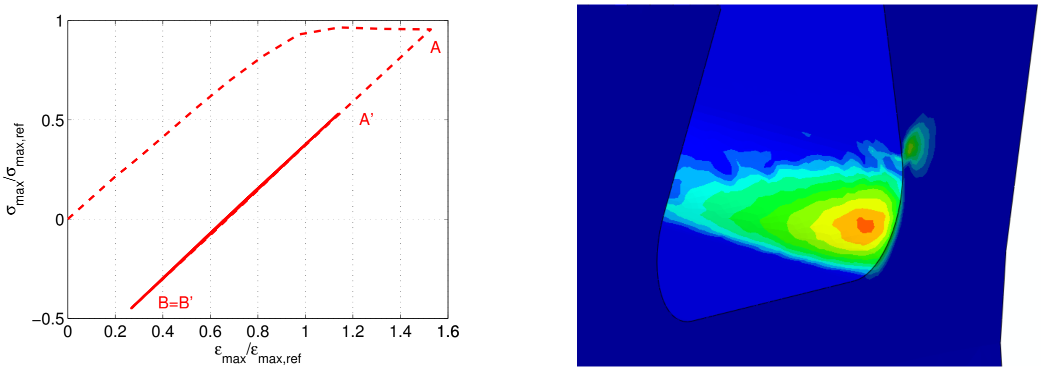

(a) (b)

Figure 3.3: *FEM results of the disk sector: a) Stress-strain behavior, b) Plastic strain field after the first unloading.*

3.2.2 Companion specimen

To experimentally reproduce the stress-strain field experienced in the blade attachment, a notched specimen was designed (Fig. 3.4). The conditions required for the specimen geometry were the following: it had to reproduce the same equivalent plastic strain, PEEQ, field induced by the cycle performed during the spinning test and the maximum principal stress, σ_{max}, experienced by the disk in the following two cycles, considering a stress ratio, R, equal to 0. In order to fulfill these requirements, several geometries were checked. Good agreement was obtained considering a specimen with a semicircular notch with a 9 mm radius onto a 30mm x 18 mm rectangular section. The final geometry used for testing is depicted in Fig. 3.4. The comparisons between the numerical results of the disk and of the companion specimen, in terms of PEEQ and σ_{max}, are reported in Fig. 3.5a and Fig. 3.5b. The specimen geometry best reproduces the plastic gradient and the principal stress in the 30 mm deep direction. However, differences in terms of triaxiality between the disk and the companion specimen can be present.

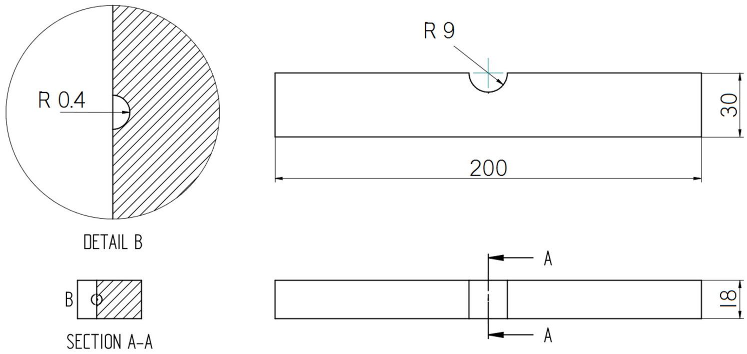

Figure 3.4: *Specimen geometry and EDM micronotch orientation. All dimensions are expressed in millimeters.*

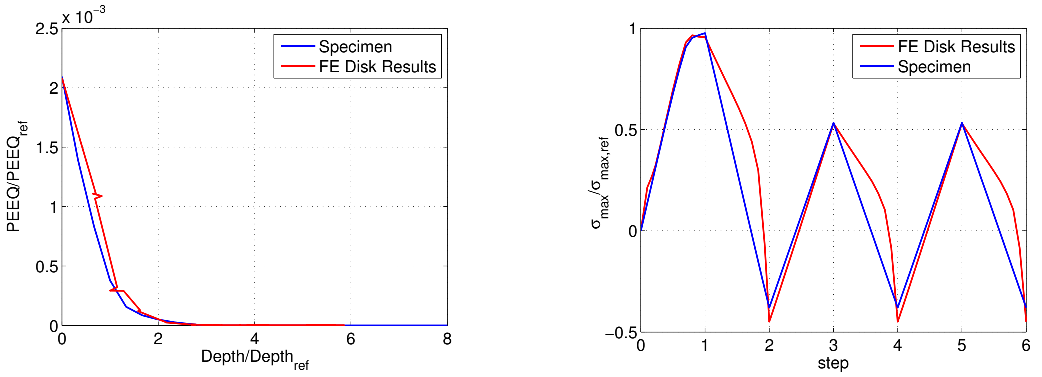

(a) (b)

Figure 3.5: *FEM analysis of the companion specimen. a) Equivalent plastic strain field; b) Maximum principal stress field.*

3.2.3 Stabilized hysteresis loops at the root of the specimens notch

Three different loading conditions were investigated, as shown in Fig. 3.6a. The first case consisted in an overload cycle, performed with a rotational speed higher than the nominal one, followed by two cycles performed at nominal speed. In the following, this condition, which reproduces the in-service conditions of the disk, will be referred to as OL+BL. In the second condition (afterwards referred to as BL), cycles were only performed at the nominal rotational speed, whereas in the third case (hereinafter referred to as OL) only overload cycles were considered. In the OL and BL load cases, 100 start-up and shut-down cycles were simulated, in order to check material stress/strain transient behavior.

The results of the FE analysis, performed considering the OL+BL case, are shown in Fig. 3.6b. As expected, the elastic shakedown condition is reached. The following cycles remain elastic and exhibit a stress ratio R very close to -1, because of the high residual strains present, generated by the initial overload. Even in the BL condition (Fig. 3.6c), the material experiences elastic shakedown, soon after the first load cycle. Due to the modest plastic strain present after the first load and the consequent low residual stresses, the stabilized load cycle is close to a stress ratio R = 0. In the OL case, the elastic shakedown condition is reached after some initial mean stress relaxation, as depicted in Fig. 3.6d: the 100th cycle is stabilized and exhibit a stress ratio equal to -1, as in OL+BL case.

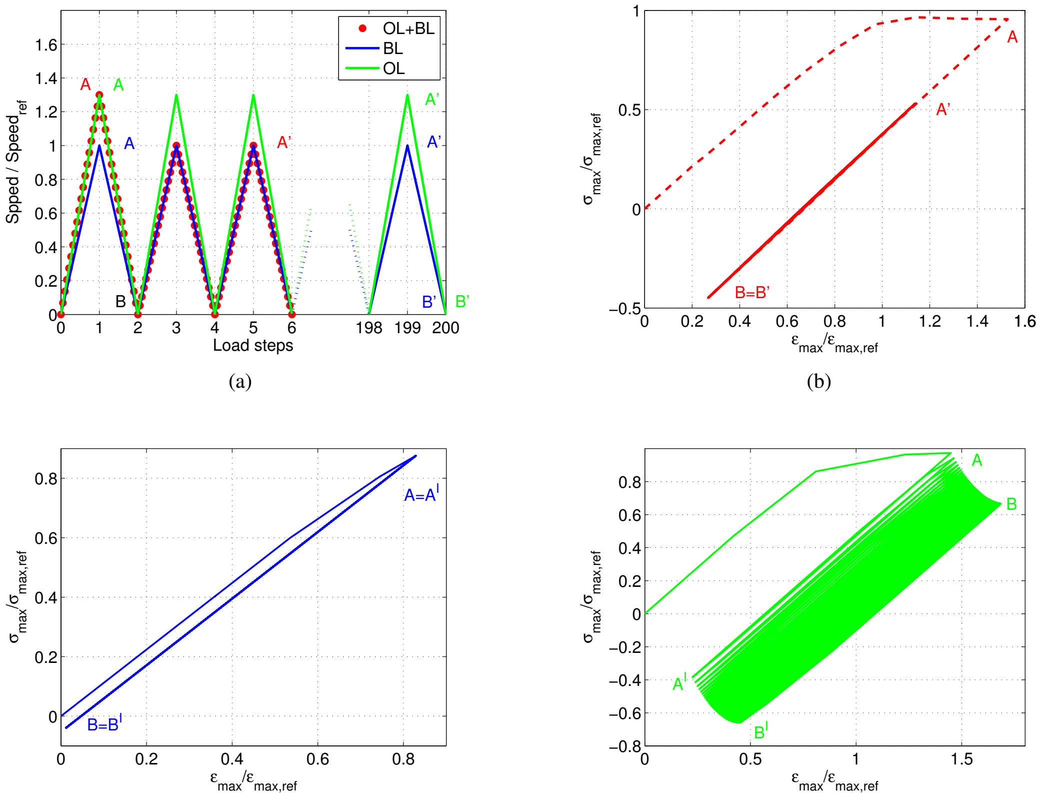

(a) (b) (c) (d)

Figure 3.6: *Results of the FE analysis: a) Load conditions considered b) with first overload (OL+BL), c) only nominal speed (BL), d) only overload (OL).*

3.3 FATIGUE EXPERIMENTS PERFORMED ON COMPANION SPECIMENS

In order to simulate the presence of a defect, a small semi-circular electrical discharge machining (EDM) micronotch was introduced at the deepest point of the semicircular notch, as depicted in Fig. 3.4. Considering the typical resolution [72] of the magnetic particle inspection (MPI) technique commonly adopted for inspecting rotor disks (together with ultra-sonic (US) scans), the depth of the defect was set to a_0 = 0.4 mm (a detail of the micronotch is shown in Fig. 3.7).

Six uniaxial fatigue tests were performed, two for each of the three load cases considered. A 250 kN servo-hydraulic load frame was employed for testing. Tests were performed under load control with a frequency of 0.5 Hz. Each test was regularly interrupted to measure crack length, adopting the plastic replica technique discussed in Chapter 2 and depicted in Fig. 3.8. This technique allowed the measurement of the surface crack length $2c$, as shown in Fig. 3.8b. In Fig. 3.9a the crack advancement, in terms of surface crack length c vs. number of cycles N, is reported. Crack growth rates were calculated by applying the $secant\ method$.

Experimental results, in terms of crack growth rates are shown in Fig. 3.9b, in which it can be observed that the rates registered during BL experiments almost doubled those experienced in the OL+BL. This fact shows the beneficial effect of the residual

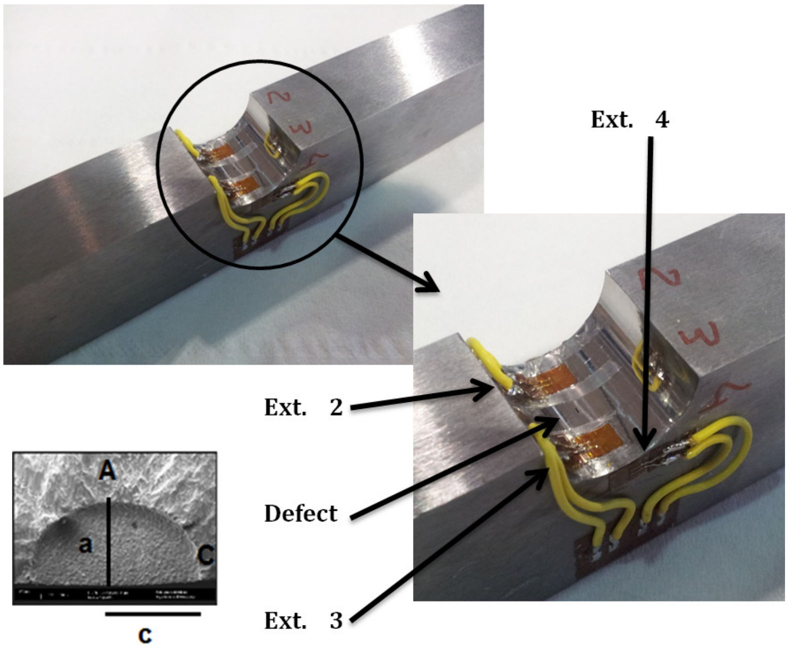

Figure 3.7: *Companion specimen with defect and strain gauges*

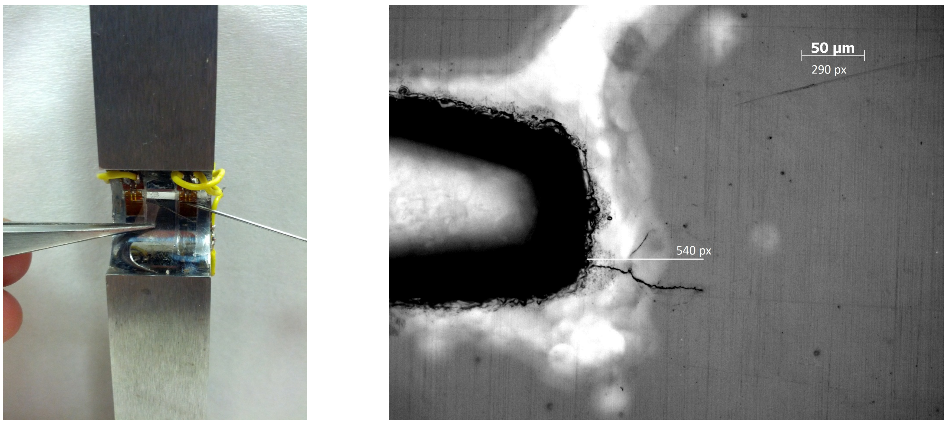

(a)

(b)

Figure 3.8: *The plastic replica technique; a) Plastic replica preparation; b) Measurement of the surface crack from the replica under a microscope.*

stress field generated during the spinning tests. Talking about the OL case (load cycles corresponding to start-ups up to overspeed), registered crack growth rates were higher than those observed in the previous cases, approximately three times faster than those experienced during the OL+BL experiments.

All the samples were equipped with four strain gauges (gage length equal to 2.5mm), to check specimen alignment and to record the force-strain response of the material in the 9 mm notch root during the test, as shown in Fig. 3.7. All the gauges were positioned in order to measure axial strains. Experimental results, obtained from one of the two tests performed under OL+BL loading conditions, are shown in Fig. 3.10: experimental data, in terms of load vs. strain at the root of the notch, confirm the

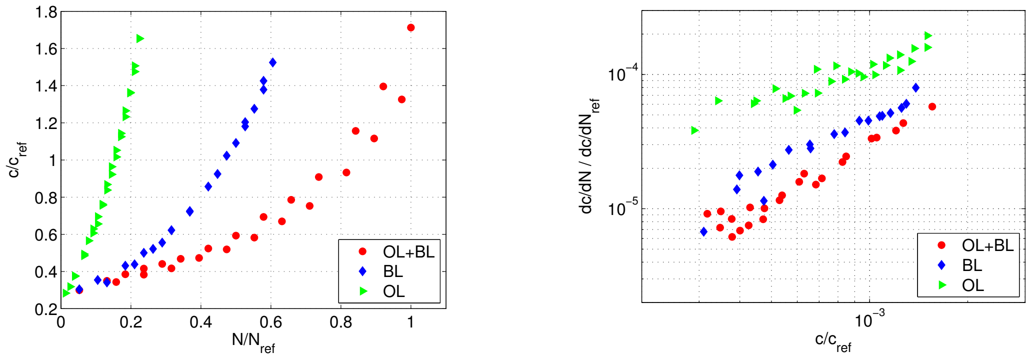

(a)

(b)

Figure 3.9: *Experimental results. a) Crack length evolution during the tests; b) Crack growth rates vs surface crack length.*

shakedown condition that had been numerically predicted. It was not possible to make this comparison for all the specimens and for the entire duration of the tests, because of early gauge failures due to the high strains present.

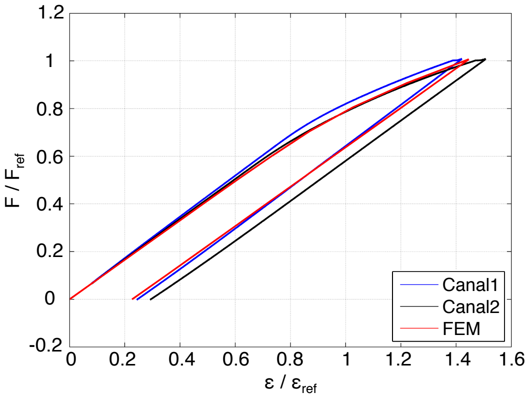

Figure 3.10: *Experimentally registered force/strain behavior during a OL+BL test.*

After the end of the tests, each specimen was broken in liquid nitrogen to observe the shape of the fatigue crack. An example of the fracture surface is reported in Fig. 3.11. The average aspect ratio, a/c, measured at the end of the fatigue tests, was 0.9 for all the specimens. This value was different from the initial shape factor, which was equal to 1 (semicircular EDM micronotch). The change in crack shape, registered during fatigue propagation, was due to the different value of ΔK applied at the deepest point of the crack and at the specimen surface. The relationship between a and c was calculated considering that the ratio between a and c changes linearly during the propagation, from 1 (beginning of the test), to 0.9 (test termination). Consequently, the experimental measurement of the surface crack length c allowed the direct estimation of the crack depth a during propagation experiments.

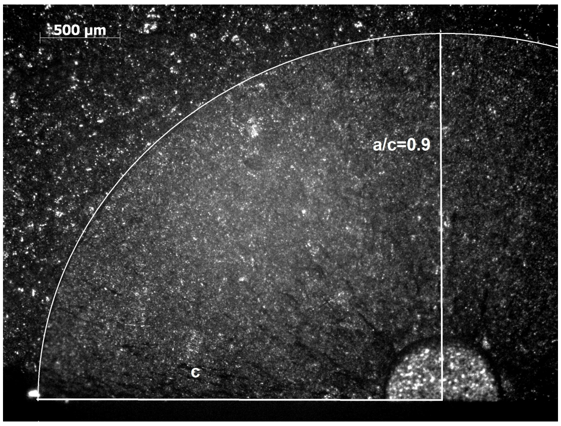

Figure 3.11: *Fracture surface after the end of a fatigue test.*

3.3.1 Nucleation

An EDM micronotch with a depth of 0.4 mm can be modeled as a short crack [73]. The elastic shakedown condition implies that the short cracks are subjected to fully elastic load cycles. This means that specimens fatigue life can be treated as an initial nucleation/incubation and a consequent propagation problem [74].

In this work, it was assumed that nucleation is the minimum surface crack length necessary to have a unique stable crack front around the initial defect, as schematically depicted in Fig. 3.12. By means of microscopic observations (at the specimen surface and at the bottom of the micronotch), the minimum crack advance for a stable propagation for the initial defect has been estimated between 50 and 80 μm, different for the three load cases:

$$\Delta c_{nuc} = \Delta a_{nuc} = 65 \pm 15 \mu m \tag{3.1}$$

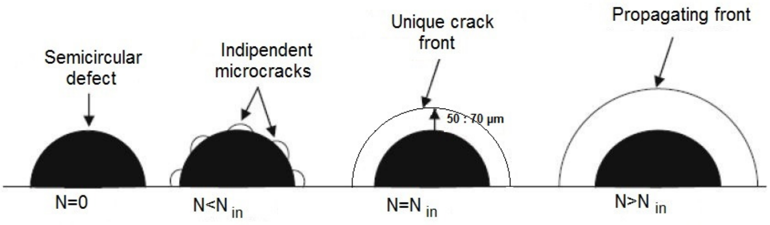

Figure 3.12: *Schematic of crack formation from the artificial defect.*

3.4 FATIGUE CRACK GROWTH

3.4.1 Stress intensity factor calculations

According to Feng and Gross [75], shakedown problems of cracked structures can be modeled in terms of the stress intensity factor K. Accordingly, the value of the SIF at crack tip has been calculated through a suitable weight function (WF). In particular, the stress intensity factor K at the deepest point A of the crack (as shown in the detail of Fig. 3.7) was expressed as:

$$K_A = \int_0^a h_a\left(x, a\right) \sigma\left(x\right) dx \tag{3.2}$$

where $h_a\left(x, a\right)$ is the WF by Wang and Lambert [76] for the tip A of a semielliptical surface crack in a finite thickness plate. Similarly, the Stress Intensity Factor K at the surface point C (as depicted in the detail of Fig 3.7) of the crack was:

$$K_C = \int_0^a h_c\left(x, a\right) \sigma\left(x\right) dx \tag{3.3}$$

where $h_c\left(x, a\right)$ is again the WF for tip C of a surface semi-elliptical crack [76]. This WF was chosen because of the modest curvature of the notch with respect to crack size: a comparison with a series of elastic FEM analyses onto semicircular cracks showed good predictions by Eq. 3.2 and 3.3.

In order to apply Eqs. 3.2 and 3.3, it was necessary to fit the stress distributions, calculated from the numerical analysis performed on the companion specimen, with appropriate polynomial functions. In this phase, the final cycle (corresponding to load steps A' and B') was considered. Starting from this polynomials, it was possible to accurately calculate the values of K_{max} and K_{min} (corresponding to points A' and B' respectively).

3.4.2 Crack closure implementation

At this point the effects of crack closure were considered. Following the suggestions reported in [77], the load ratio R was substituted by the applied K-ratio:

$$R = \frac{K_{min}}{K_{max}} \tag{3.4}$$

Consequently, even the definition of the closure factor f, was modified, as originally proposed in [78]:

$$f = \frac{K_{op}}{K_{max}} \tag{3.5}$$

so that

$$\Delta K_{eff} = K_{max} - K_{op} = \frac{1-f}{1-R} \Delta K \tag{3.6}$$

Finally, the crack growth rate at crack tips A and C was described as [10]:

$$\frac{da}{dN} = c_{07}\left(\Delta K_{eff}\right)^{n_{07}} \tag{3.7}$$

where C_{07} and n_{07} are the parameters of the effective crack propagation curve, obtained testing the material at a load ratio R equal to 0.7. These parameters were obtained following the requirements proposed in the ASTM E647 standard.

The closure factor, f, was calculated through Newman's expressions [79], as reported in Eq. 1.5. The analytical model by Newman, which was developed for a through crack, provides satisfactory results even for semi-elliptical surface cracks, as described in [3] and [34]. Such an approach is also adopted to evaluate closure levels for surface cracks in the short crack propagation model proposed in the European SINTAP / FITNET Procedure [39]. Because of the complexity of the geometry of the specimen, the normalized stress σ_{max}/σ_0 has been replaced with the normalized Stress Intensity parameter K_{max}/K_0, as proposed in [78] and [80]:

$$f = function\,(K_0, K_{max}, \alpha) \tag{3.8}$$

where K_0 is the flow stress intensity factor, as in [78] and [81], and α is the constraint factor, whose value will be discussed below. Different expressions have been proposed to define σ_0 [4, 5, 22], but because of the very high level of σ_{max}, in this work it was calculated assuming Newman's original formulation [5]:

$$\sigma_0 = \frac{R_m + R_{p,02}}{2} \tag{3.9}$$

3.4.3 Constraint factor calculation

In order to determine the constraint factor, the plastic zone at the crack tip of a crack propagating from the EDM notch was estimated by a series of FEM analyses. In particular, considering a semi-circular crack on the symmetry plane, only one fourth of the specimen with the EDM micronotch was modeled, together with different prospective crack sizes, as shown in Fig. 3.13. The analyses were performed by employing the same solver and the same cyclic plasticity model previously discussed. The constraint factor α at P_{max} was calculated as [82]:

$$\alpha = \frac{\int_{A_0} \sigma_n dA_n}{\sigma_0 A_0} \tag{3.10}$$

where σ_n is the stress in the $n-th$ yielded element of the plastic zone, A_n is the projected area of the same element on the ligament and A_0 is the projected area of the whole plastic zone on the ligament.

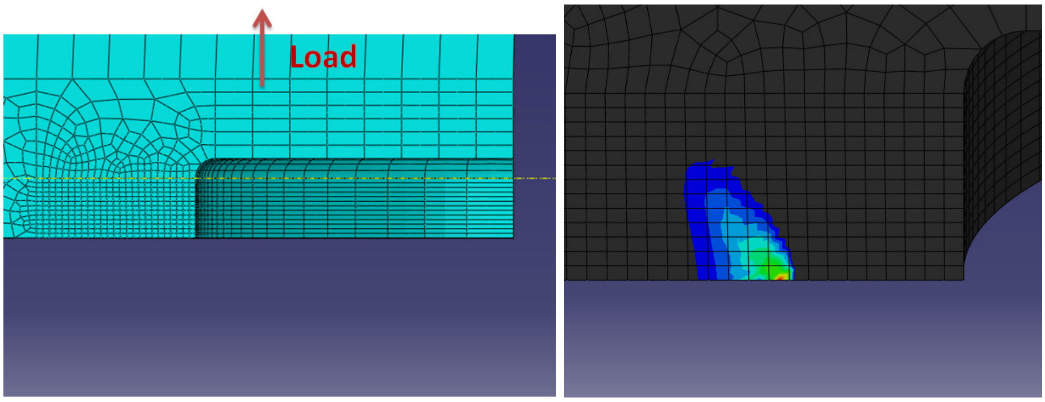

(a) (b)

Figure 3.13: *FEM model for the calculation of constraint factor α: a) Refined mesh at the crack tip, b) Plastic zone at the crack tip at the maximum load (stabilized cycle).*

The analyses have been carried out for different crack depths and for all the three load cases. In Tab. 3.1 results in terms of α, for the OL+BL case, are reported. The influence of the parameter α on life prediction is generally low, as depicted in Fig. 3.14, in which the OL+BL case was considered. Consequently, in the crack growth simulations an average value $\bar{\alpha}$ was considered, to correctly represent the constraint factor during the entire crack propagation.

Table 3.1: *Constraint factor - α - calculated through FE analyses for the OL+BL load case.*

a/a_{ref}	α
0.17 0.3 0.6	1.38 1.49 1.65
$\bar{\alpha} = \frac{1}{n}\sum_{i=1}^{n} \alpha_i$	1.51

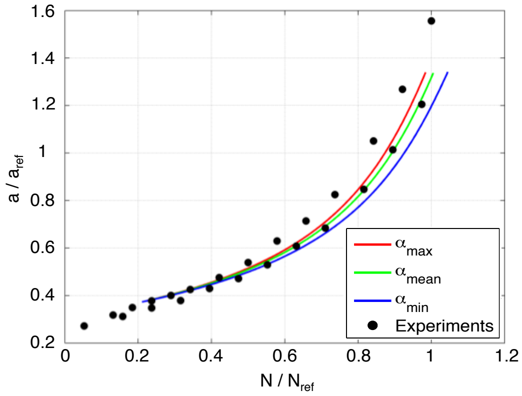

Figure 3.14: *Influence of the constraint factor α on the life prediction in OL+BL case.*

3.4.4 Results and discussion

A propagation algorithm was implemented to iteratively calculate crack advancement for the two crack tips from initial crack length:

$$a_{start} = c_{start} = a_0 + \Delta a_{nuc} \tag{3.11}$$

and then:

$$\begin{cases} a_{i+1} = a_i + da = a_i + \frac{da}{dN}\Delta N \\ c_{i+1} = c_i + dc = c_i + \frac{dc}{dN}\Delta N \end{cases} \tag{3.12}$$

The comparisons between prediction and experimental data (expressed in terms of the estimated crack depth) are shown in Fig. 3.15a (crack growth rate) and Fig. 3.15b (crack depth). In crack growth calculations, the predicted aspect ratio was approximately 0.92, close enough to the average experimental value.

Crack propagation model is capable of correctly estimating both the OL+BL and the OL case, whereas it is very conservative when the BL condition is considered. The difference between predicted and experimental fatigue life, in the BL case, is equal to 40%.

This behavior can be explained by considering that Newman's f factor, as discussed in [83], is not very precise when K_{max} is similar to the limit value K_0: this condition occurs in the BL case, where the plastic strain field is very low and the maximum value of σ_{max} is close to the limit value σ_0, resulting in less accurate predictions. In OL+BL and OL cases, the residual compressive stress fields in the elastic-shakedown condition significantly decreases the value of K_{max} reached during the cyclic load, with respect to the BL case, reducing the value of K_{max}/K_0 and thus increasing the accuracy of Newman's analytical model.

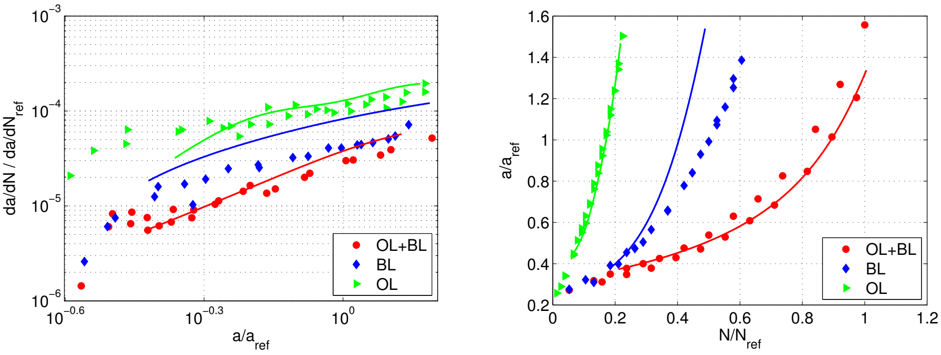

(a) (b)

Figure 3.15: *Crack growth model results: a) crack growth rates; b) crack length.*

Moreover, it is worth remarking that the ΔK cycles registered under OL+BL conditions are less severe than the ones observed in the BL case, since in the first case a stress ratio similar to R=-1 is observed, whereas in the BL situation a stress ratio equal to 0 is applied to the crack (this effect can be appreciated also from Fig. 3.6). This is the most likely reason of the difference registered in propagation lifetime between the OL+BL and BL conditions, which is approx. 50% greater in the former case, respect to the latter. The accuracy of the results presented in this section, however, is mainly related to the correct estimation of the applied stress ratio applied to the crack. In particular, it was found that the analytical model proposed by Newman provides satisfactory results only at R= -1, the loading conditions found in the OL and OL+BL cases.

On the other hand, a fatigue life assessment of OL and OL+BL cases, performed considering Masing's hypotheses, would have provided very conservative results, since it would have considered a positive load ratio (R $\geq$ 0). In particular, the adoption of Harkegard's formulation [84,85] to the OL case would have provided very conservative results, since it would have considered crack growth rates three or four times faster than the ones experimentally observed.

3.5 CONCLUSIONS

In this chapter, fatigue crack growth of short cracks in presence of a plastic strain gradient was investigated. In the first part of the chapter, a numerical model of a compressor disk was implemented, in order to evaluate the stress field acting at the dovetail attachment of the blades. The analysis highlighted the fact that an elastic shakedown condition is reached at the bottom of the blade attachment: this means that all the cycles performed after the spinning tests are fully elastic.

At this point, a companion specimen was designed, in order to reproduce the stress condition registered at the root of the blade attachment. The companion specimen allowed the analysis of three different loading conditions. In the first case (OL+BL), the loading conditions considered for the disk simulation were employed: an initial overload followed by cycles performed at nominal load were considered. In the second case (BL) the strain field of a disk subjected to cycles performed at nominal speed was considered (BL), whereas, in the third situation (OL), the effects of a series of cycles performed considering only the overload condition were evaluated (OL).

A series of crack growth tests were performed on the companion specimens. Specimens contained, at the root of the notch, a 0.4 mm deep EDM micro notch, in order to simulate the presence of a potential defect. Before testing, four strain gages were applied at the root of the 9 mm-deep notch, in order to measure the local strains and to check specimen alignment. Experimental results, in terms of strain/stress cycles, were compared to those numerically calculated, showing good agreement. Moreover, the experiments showed that the residual stress field induced by the OL cycle was able to significantly increase the fatigue life of the notched specimens, since the crack growth rates measured during the tests performed under the BL conditions were almost the double of those registered during the experiments performed considering the OL+BL case. As expected, the experimental campaign also underlined the fact that the most critical condition considered is the OL one, since the experimental rates were almost three times higher than those registered in the OL+BL case.

A crack propagation algorithm, based on Newman's closure function, was developed in order to assess fatigue life. Crack propagation was described in terms of the effective stress intensity ranges, calculated from the numerical models by applying a WF method. The analytical model proposed by Newman was modified, to take into account the effect of the non-uniform stress field: the ratio between σ_{max} and σ_0 was replaced in the model by the equivalent K-ratio. The modified model was able to correctly describe both the OL and the OL+BL conditions, whereas it provided a very conservative estimate when the BL condition was considered. This was related to the fact that, for the latter situation, the registered value of K_{max}/K_0 was approaching the value of 1, a condition in which the Newman's usually provides bad closure estimates.

CHAPTER 4

Fatigue crack growth in Ni-based superalloy single crystals

4.1 INTRODUCTION

The continuous research for sustainable and efficient energy has led to the renewed interest in nickel-based alloys in the power generation industry. In particular, nickel based superalloys exhibit good resistance to creep and corrosion, properties that make them the preferable choice for components working in aggressive conditions.

A further enhancement in materials properties can be obtained by not only changing the alloying elements, but also the crystal structure. In order to increase creep properties, single crystals are the most adopted structure for components such as turbine blades, since such a structure does not include polycrystalline grain boundaries. Grain boundaries are the location in which voids, responsible for creep failure, originate and grow.

On the other hand, the adoption of single crystal components requires an accurate design, since single crystals exhibit a marked anisotropic behavior and crack propagation occurs along directions related to the crystal slip plane orientations.

In this chapter, fatigue crack growth in single crystals of a commercially available nickel based superalloy, Haynes 230, is investigated at room temperature in order to remove environmental effects, such as oxidation. The main focus of this research is to accurately analyze fatigue crack growth in order to implement Haynes 230 single crystals into a damage tolerant design.

The chapter is divided into four different parts:

- In the first part of the chapter, the experimental procedure adopted for testing Haynes 230 single crystal specimens is discussed. Experimental results, obtained testing two different crystal orientations, are presented. The influence of crystal orientation is discussed in terms of crack propagation direction.

- In the second part of the paper, the displacement field acting at the crack tip during propagation is measured with digital image correlation. Crack opening and sliding levels are evaluated from the relative displacements of the crack flanks. A regression algorithm, based on the analytical K-field, is modified to take into account the effects of crystal anisotropy and it is employed to extract crack propagation driving forces.
- In the third section, the effective stress intensity factor ranges are employed to measure the strain irreversibility at the crack tip. An anisotropic yield criterion is employed to measure the extension of the cyclic plastic zone for the two different crystal orientations.
- In the final part of the chapter, a numerical model, which takes into account single crystal plasticity, is implemented. Cyclic plastic zones are evaluated from FEM results and compared to those calculated from the regressed stress intensity factor ranges. Good agreement, both in terms of shape and extension, is found, underlining the capability of the presented regression algorithm to describe fatigue crack growth in single crystals.

4.2 EXPERIMENTS

4.2.1 Material and fatigue testing

Commercially available Haynes 230 was used for testing. Haynes 230 is a nickel-based superalloy, which exhibits good corrosion and creep resistance due to the addition of chromium, molybdenum and tungsten. Haynes 230 chemical composition is provided in Table 4.1.

Table 4.1: *Chemical composition (%wt) of Haynes 230.*

Al	B	C	Co	Cr	Cu	Fe	La	Mn
0.35	0.005	0.1	0.16	22.14	0.04	1.14	0.015	0.5
Mo	Ni	P	S	Si	Ti	W	Zr	
1.25	bal.	0.005	0.002	0.49	0.01	14.25	0.01	

Single crystals were obtained from a seed, adopting the Bridgman technique in vacuum: initial crystal orientation was determined using electron backscatter diffraction (EBSD): at this point slices parallel to $\{1\ \bar{1}\ 0\}$ were cut. The choice of this plane is due to the fact that it contains both of the crystallographic orientations of interest, i.e. $[0\ 0\ 1]$ and $[1\ 1\ 1]$.

Single edge notch tension specimens were employed for the experimental campaign. Notches were made by electrical discharge machining (EDM). The specimens width, gage length and notch depth were 3, 8 and 0.5 mm, respectively; the $[1\ 1\ 1]$ oriented specimen thickness was 1.3 mm, whereas the $[0\ 0\ 1]$ oriented crystal was 1.09 mm thick. A schematic of the specimen geometry is shown in Fig. 4.1. Tensile properties of the two orientations of interest, obtained from monotonic tests on untouched specimens, are shown in Table 4.2.

Table 4.2: *Selected tensile properties of Haynes 230 alloy specimens*

Crystallographic orientation	Yield stress, 0.2% offset [MPa]	Elastic modulus [GPa]
[0 0 1]	274	137
[1 1 1]	428	330

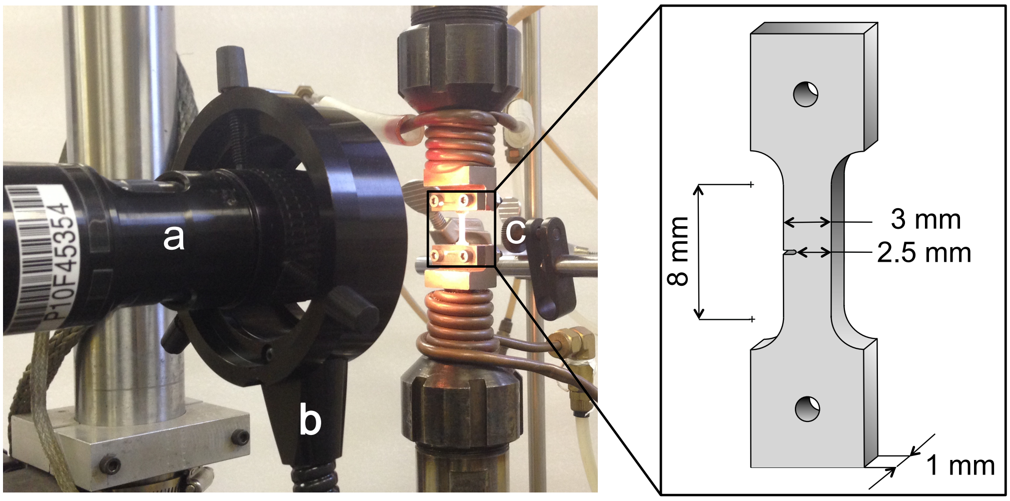

Figure 4.1: *The experimental setup and a schematic of specimen geometry. a) Camera and lens; b) light source; c) specimen.*

Before testing, specimens were prepared by mechanically polishing the surface to a mirror finish with abrasive paper, up to a grit of P2400. A speckle pattern, necessary for digital image correlation, was then applied onto each specimen using black paint. In order to obtain a refined speckle pattern, necessary for high quality measurements, an airbrush with a 0.18 mm wide nozzle was employed for painting. Images were acquired by a digital camera, whose resolution and maximum frame rate were, respectively, 1600 by 1200 pixels and 15 fps. A magnification of 2.7X, obtained using an adjustable lens with a 12X magnification range and a 2X adapter, was employed during the tests. This setup allowed a resolution of 0.63 $\mu m/pix$. The experimental setup is shown in Fig. 4.1. Tests were performed with a cyclic frequency of 5 Hz on a servo-hydraulic load frame with a fixed load ratio R equal to 0.05. $[1\ 1\ 1]$ oriented specimen was subjected to a cyclic load with a stress range of 181 MPa. The stress range was reduced to 133 MPa for the $[0\ 0\ 1]$ crystal, since this orientation exhibited a lower yield stress.

Image acquisition and the servo-hydraulic load frame were controlled by a computer, which recorded images and their applied loads, measured by a 7.5 kN load cell. After crack initiation, measurement cycles were run periodically at a rate of 0.25 Hz to obtain a greater number of images per cycle, providing the possibility of a more accurate fatigue cycle analysis.

After the end of the fatigue test, EBSD was performed on the specimens, in order to verify their orientations. For the $[0\ 0\ 1]$ oriented specimen, the normal was determined to be $[4\ \bar{3}\ 0]$ and the transverse direction was $[3\ 4\ 0]$, The $[1\ 1\ 1]$ specimen had a normal direction of $[0\ \bar{1}\ 1]$ and thus the transverse orientation was $[2\ \bar{1}\ \bar{1}]$. A schematic of the two specimens indicating the loading directions in the crystal frame is shown in

Fig. 4.2. $(1\ 1\ 1)$ slip planes are shown in cyan, whereas crack propagation planes are represented in purple.

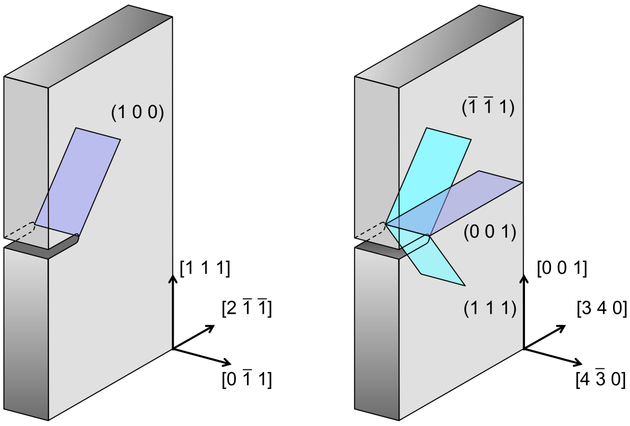

Figure 4.2: *A schematic of the samples in the crystal frame showing the loading directions.* $(1\ 1\ 1)$ *slip planes in cyan and crack propagation planes in purple.*

Crack propagation is due to the irreversibility of slip, which is also responsible for inelastic deformations. In single crystals, fatigue crack growth strongly depends on crystal orientation, which determines the number of slip systems active during propagation and the plane in which the crack extends [86]. In particular, dislocations are emitted from the crack tip during loading and are not fully reversed during unloading [87], leaving marks on the specimen surface, usually referred as slip-plane traces. These features can be observed during propagation when high plastic strains are present, i.e. when the ligament is small respect to defect size, and can be used to confirm the crystal orientation given by EBSD. On the surface of the $[0\ 0\ 1]$ oriented crystal it was possible to observe these traces, that extend from the crack plane at an angle of 54°, as depicted in Fig. 4.3. This angle is in agreement with the crystal orientation given by EBSD, since it corresponds, with an error of 0.4° (54° instead of 54.4°), to the analytically calculated traces of the $(1\ 1\ 1)$ and $(\bar{1}\ \bar{1}\ 1)$ slip planes.

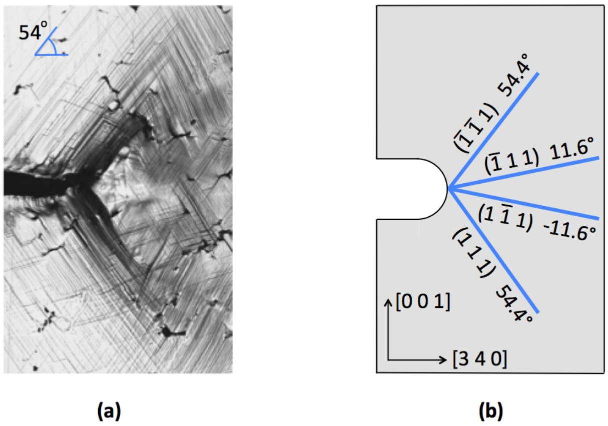

Figure 4.3: *Slip plane traces analysis: a) surface of the* $[0\ 0\ 1]$ *oriented crystal after the end of fatigue testing; b) analytical slip plane traces calculated from EBSD crystal orientation.*

4.2.2 Digital image correlation procedure

The experimental displacements measured by DIC are the starting point for the analysis presented in this chapter. DIC compares the differences in the speckle pattern light intensity between reference and deformed images to determine the displacements. Square group of pixels, called subsets, are tracked in order to get the best correlation between the images. A description of the correlation algorithm is reported in Section 1.5.1.

DIC analysis was performed using a commercially available image correlation software (Vic 2D produced by Correlation Solutions). The first picture of each measurement cycle, taken at the minimum applied stress, was used as the reference image for that cycle. Full field images were correlated to get horizontal and vertical displacements. This means that during calculations points before and beyond crack tip were considered. Displacements were calculated using square subsets, whose maximum dimensions were 51 by 51 pixels. These displacements were employed to evaluate stress intensity factor ranges, ΔK, following the procedure discussed in Section 4.2.3. An example of the vertical displacement field, registered for each of the two analyzed specimens, is reported in Fig. 4.4.

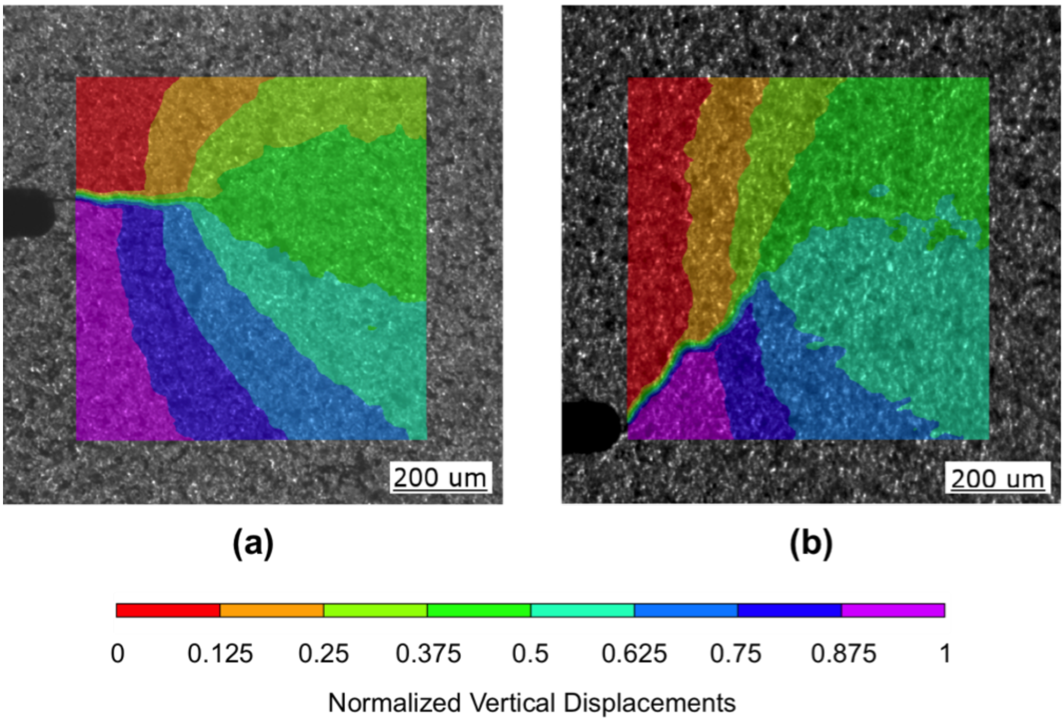

Figure 4.4: *Examples of vertical displacements of each specimen, calculated by digital image correlation a)* [0 0 1] *oriented single crystal specimen at R=0.05 and $\Delta\sigma$=133 MPa. b)* [1 1 1] *specimen at R=0.05 and $\Delta\sigma$=181 MPa.*

Two-point virtual extensometers were employed to measure crack opening/sliding loads. This feature tracks two subsets, one on each side of the crack flanks, as shown in Fig. 4.5a. Several virtual extensometers were placed on the length of the crack flanks, in order to get an accurate displacement profile during cyclic loading. In order to get the pure vertical (Δv) and horizontal (Δu) displacements, virtual extensometers were placed perpendicular to the flanks. Once rotated to the crack coordinate system

(Fig. 4.5c, the difference in the vertical crack tip displacements, $\Delta v = v_{upper} - v_{lower}$, was employed to describe Mode I opening, whereas the horizontal crack tip displacements, $\Delta u = u_{upper} - u_{lower}$, were used to describe Mode II crack sliding.

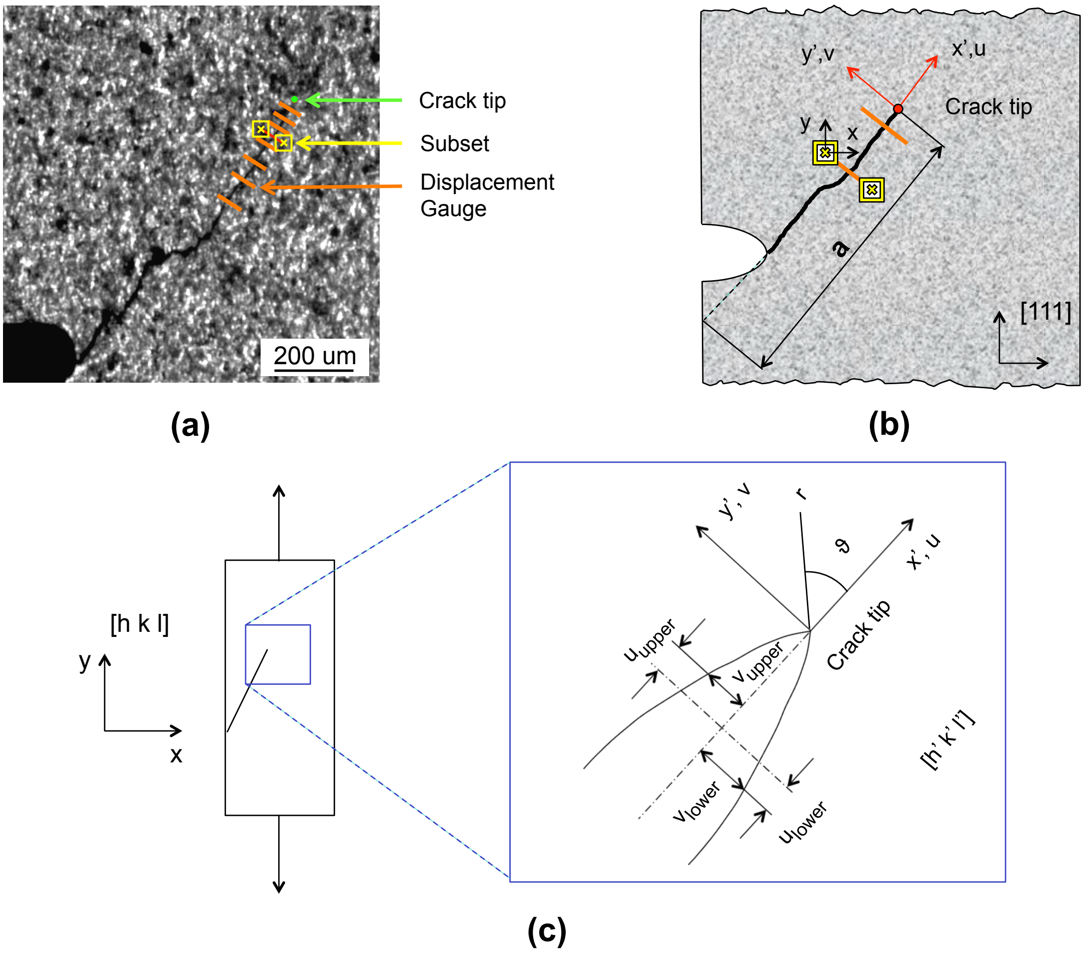

Figure 4.5: *a) An example of virtual-extensometers disposition on the* $[1\ 1\ 1]$ *specimen; b) A schematic showing the displacements measured by extensometers; c) Coordinate system for measuring crack opening and sliding displacements and for extracting* ΔK_{eff}.

4.2.3 Effective stress intensity factor ranges extraction

The adoption of DIC allows the determination of a full displacement field, which can be used to evaluate crack propagation driving forces without geometric considerations. A nonlinear least-squares regression can be used to determine effective stress intensity factor ranges and how they change during a load cycle. The procedure described in [88] was adopted.

During measurement cycles, test frequency was slowed down and the entire loading and unloading parts of the cycle were recorded. These displacements were the starting points for ΔK_I, ΔK_{II} and T-stress calculations. For a mixed-mode loaded crack, the crack-tip displacements for an orthotropic material are described by Eq. 4.1 and 4.2, as [89, 90]. In this set of equations, horizontal and vertical displacements, together with material elastic constants, are referred to the local crack tip coordinate system, as shown in Fig. 4.5c.

$$\begin{aligned} u =&K_I\sqrt{\frac{2r}{\pi}}Re\left\{\frac{1}{\mu_1-\mu_2}\left[\mu_1 p_2\sqrt{cos\theta+\mu_2 sin\theta}-\mu_2 p_1\sqrt{cos\theta+\mu_1 sin\theta}\right]\right\}+K_{II}\sqrt{\frac{2r}{\pi}}\times \\ &Re\left\{\frac{1}{\mu_1-\mu_2}\left[p_2\sqrt{cos\theta+\mu_2 sin\theta}-p_1\sqrt{cos\theta+\mu_1 sin\theta}\right]\right\}+a_{11}Trcos\theta-Arsin\theta+B_u \end{aligned} \tag{4.1}$$

$$\begin{aligned} v =&K_I\sqrt{\frac{2r}{\pi}}Re\left\{\frac{1}{\mu_1-\mu_2}\left[\mu_1 q_2\sqrt{cos\theta+\mu_2 sin\theta}-\mu_2 q_1\sqrt{cos\theta+\mu_1 sin\theta}\right]\right\}+K_{II}\sqrt{\frac{2r}{\pi}}\times \\ &Re\left\{\frac{1}{\mu_1-\mu_2}\left[q_2\sqrt{cos\theta+\mu_2 sin\theta}-q_1\sqrt{cos\theta+\mu_1 sin\theta}\right]\right\}+a_{12}Trsin\theta+Arcos\theta+B_v \end{aligned} \tag{4.2}$$

where Re stands for the real part of a complex number,

$$p_i = a_{11}\mu_i^2 + a_{12} - a_{16}\mu_i \tag{4.3}$$

$$q_i = a_{1w}\mu_i + \frac{a_2 2}{\mu_i} - a_{26} \tag{4.4}$$

K_I and K_{II} are the Mode I and Mode II stress intensity factors, T is the T-stress, A is the rigid body rotation, B_u and B_v are rigid body translations in the horizontal and vertical directions, r and θ are the polar coordinates considering the origin at the crack tip and a_{ij} are the elastic constants of nickel, as reported by Hertzberg in [91]. μ_1 and μ_2 are the two complex conjugate roots from Eq. 4.5 for which the imaginary parts are positive.

$$a_{11}\mu^4 - 2a_{16}\mu^3 + (2a_{12} + a_{66})\,\mu^2 - 2a_{26}\mu + a_{22} = 0 \tag{4.5}$$

In Eq. 4.2, the vertical displacements responsible for Mode I opening are perpendicular to the crack surface. Because of this, both the horizontal and vertical displacements obtained from DIC and the compliance tensor were rotated with respect to the crack propagation angle. An algorithmm was written to solve every displacement using Eq.4.1 and 4.2, to obtain the desired parameters (K_I,$K_I I$,T,A,B_u,B_v), using a non linear least square regression. The last two terms of Eq. 4.1 and 4.2 were employed to remove rigid motion and rotation from K evaluation.

4.3 RESULTS

4.3.1 Crack closure measurements

Horizontal and vertical displacements were recorded for each virtual extensometer during fatigue cycles. Since no Mode II sliding was observed in the $[0\ 0\ 1]$ specimen, only vertical displacements around the crack tip were observed. The measured vertical displacements for a crack size of 1.23 mm are provided in Fig. 4.6a. The crack starts opening at 10% of the maximum applied load, starting from the notch. At this point the crack tip still stays closed. The crack tip opening is evident only at 19.8% of the maximum applied stress.

The crack opening displacement profiles for the [111] single crystal specimen are shown in Fig. 4.7a and b. In this case both vertical and horizontal displacements are expected, since the crack grows at an angle. In Fig. 4.7a, vertical displacements are

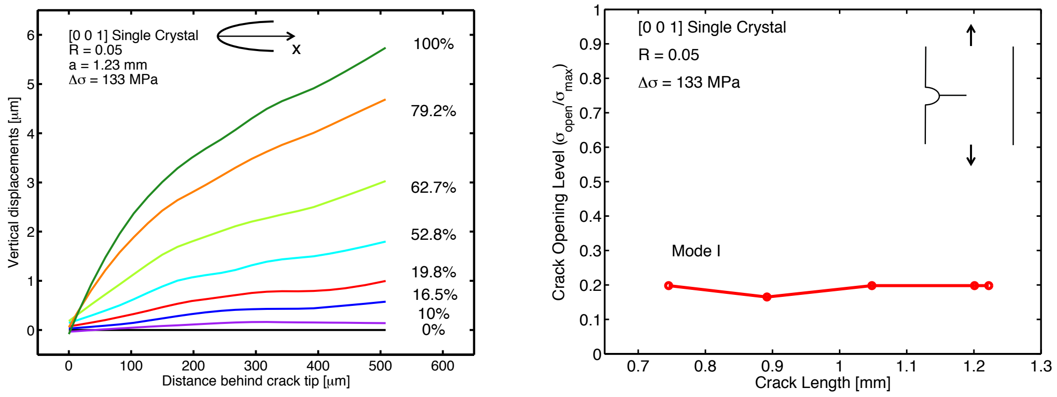

(a) **(b)**

Figure 4.6: *Virtual extensometers for the* $[0\ 0\ 1]$ *oriented specimen. a) The vertical crack opening displacement profiles of the* $[0\ 0\ 1]$ *single crystal specimen at R=0.05 and* $\Delta\sigma$*=133 MPa with a measured crack length of 1.23 mm. b) Crack opening levels for the* $[0\ 0\ 1]$ *oriented crystal.*

displayed: the crack starts opening from the notch at nearly 20% of the maximum load, but crack tip opening becomes evident only at 39.6%. Mode II displacement profiles are depicted in Fig. 4.7b: the crack starts opening at 10% of the maximum applied load, starting from the notch. At this point the crack tip is still closed. The crack tip starts opening at 19.8% of the applied load, whereas it appears fully open at 26.4% of the maximum applied stress.

Using the crack opening displacement profiles, the crack closure phenomena in both Mode I and II were measured and summarized in Fig. 4.6b for the $[0\ 0\ 1]$ oriented crystal, whereas the results of the $[1\ 1\ 1]$ oriented specimen are reported I Fig. 4.7c. The study of horizontal and vertical displacements allows for the quantification of the crack opening and sliding. The results of both the specimens tested shows that cracks were closed for approximately 20% of the loading cycle. Since in the $[1\ 1\ 1]$ oriented crystal, the crack propagated perpendicular to the loading axis, only pure Mode I was observed, as shown in Fig. 4.6b: crack opening level was constant during the propagation and was about 20% of the maximum applied load. The testing on $[1\ 1\ 1]$ oriented crystal allowed the study of mixed mode propagation, since the crack grew at an angle. As depicted in Fig. 4.7c, the crack exhibited a Mode I opening at about 40% of the maximum applied loading, whereas Mode II sliding was observed at approximately 20%.

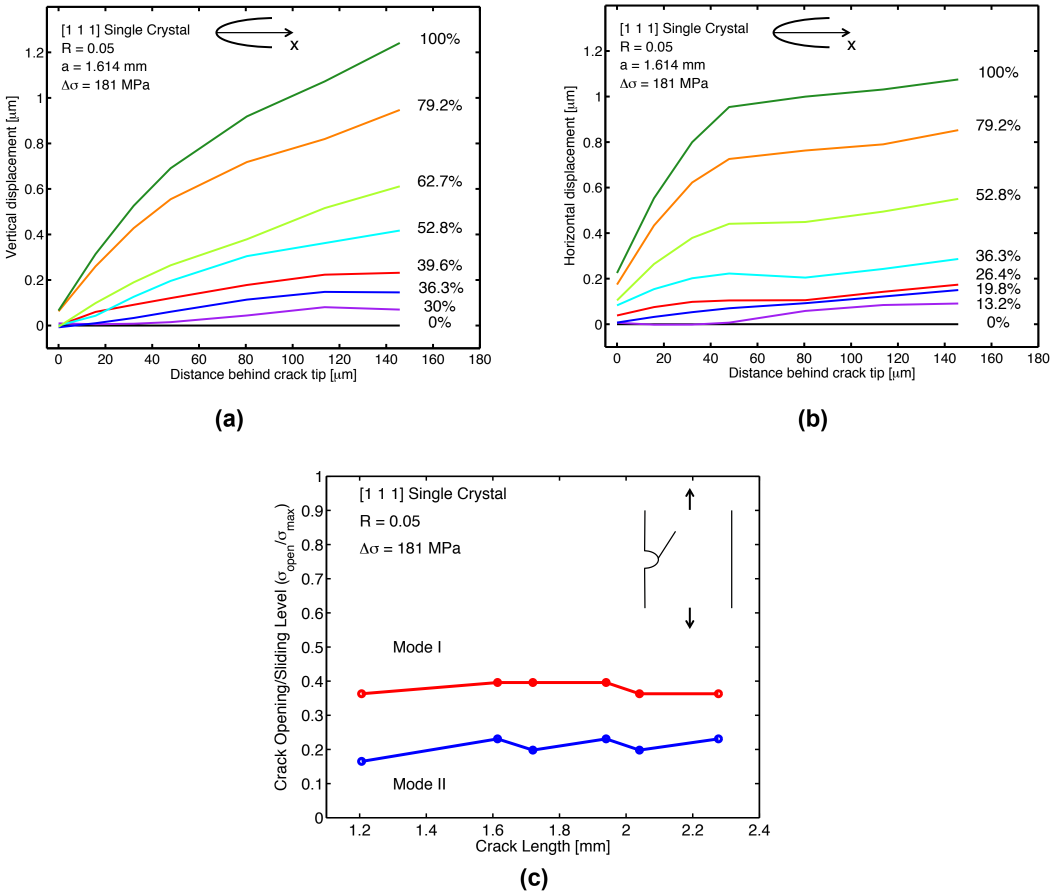

Figure 4.7: *Virtual extensometers for the* $[1\ 1\ 1]$ *oriented specimen. a) The vertical crack opening displacement profiles of the* $[1\ 1\ 1]$ *single crystal specimen at R=0.05 and* $\Delta\sigma$*=181 MPa with a measured crack length of 1.614 mm. b) The horizontal crack sliding displacement profiles of the* $[1\ 1\ 1]$ *single crystal specimen at R=0.05 and* $\Delta\sigma$*=181 MPa with a measured crack length of 1.614 mm. c) Crack opening levels for the* $[1\ 1\ 1]$ *oriented crystal.*

4.3.2 Effective stress intensity factor ranges and Paris curve calculations

The regression analysis calculates all the variables necessary to fit the displacements around the crack tip during a fatigue crack growth cycle, using Eqs. 4.1 and 4.2. These displacements will be referred to as the regressed displacements. The experimentally obtained displacements have been compared to those calculated by regression to show technique accuracy. In Figs. 4.8 and 4.9 the blue contours represent the displacements experimentally measured, whereas the regression displacements are represented by red lines. The crack tip position is described by a black mark and crack profile is represented by a solid black line. Crack tip position was chosen in order to minimize the mean square error between regressed and experimental displacements, since the presence of the speckle pattern made it difficult to find the exact tip location. This procedure does not invalidate the accuracy of stress intensity factor ranges measurements, because a few pixels error in positioning implies an error in crack tip estimation of only few microns. For each sample tested, a selected fatigue cycle is shown at the maximum applied load. When the regression was applied on the $[0\ 0\ 1]$ specimen, the Mode II stress intensity factor was nearly zero, mainly because of the absence of the shear component, due to the fact that the crack grew in a plane perpendicular to the applied load direction. In Fig. 4.8 the vertical displacements for the $[0\ 0\ 1]$ oriented specimen are depicted, showing good agreement between theory and experiments.

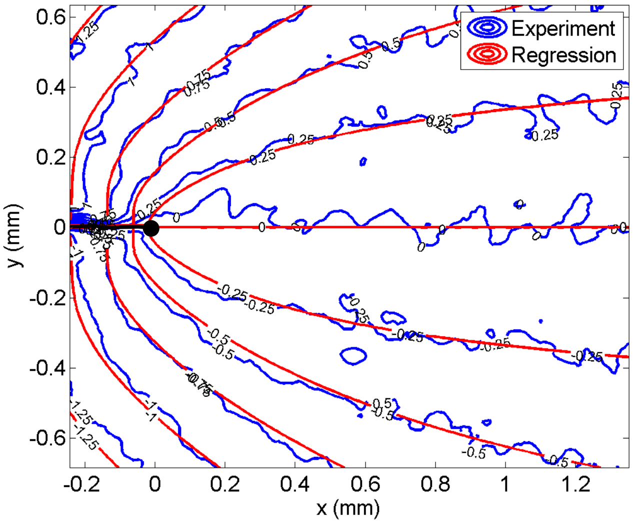

Figure 4.8: *Comparison of experimentally measured and regression vertical displacement contours in micrometers for the* $[0\ 0\ 1]$ *oriented single crystal. The crack length is 0.775 mm with a corresponding* ΔK_I *regression value of 10.78* $MPa\sqrt{m}$.

The specimen with the $[1\ 1\ 1]$ orientation was employed for the mixed mode propagation study: in Fig. 4.9a and b vertical and horizontal experimental displacements are compared to those provided by regression. The asymmetry in the horizontal displacement field underlines the presence of Mode II sliding. As in the previous case, the displacement fields obtained from regression are in good agreement with those experimentally measured.

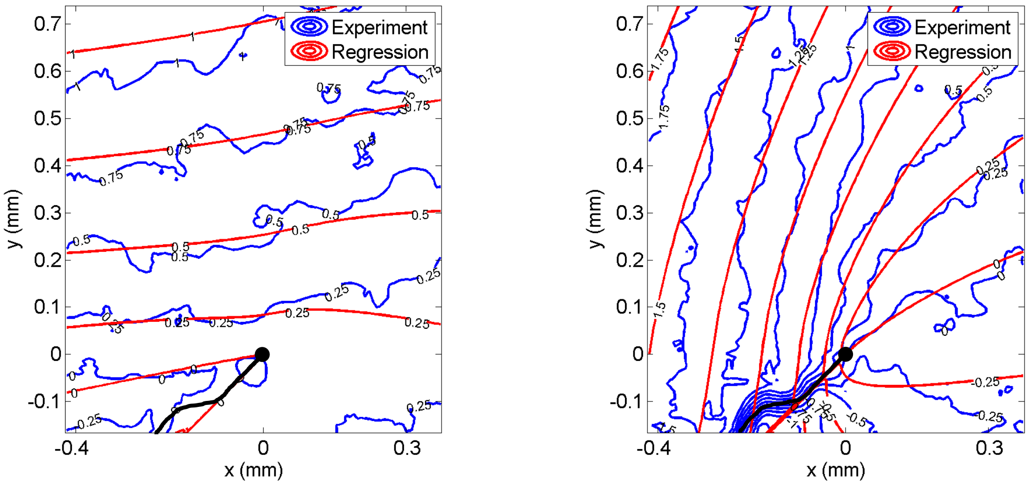

(a) **(b)**

Figure 4.9: *Comparison of experimentally measured and regression a) horizontal and b) vertical displacement contours for the* $[1\ 1\ 1]$ *oriented single crystal. The crack is 1.46 mm long with corresponding regression values for* ΔK_I *of 9.3* $MPa\sqrt{m}$ *and* ΔK_{II} *of 9.4* $MPa\sqrt{m}$.

The most general expression for combining ΔK_I and ΔK_{II} has the form [92]:

$$\Delta K_{tot} = \sqrt{(\Delta K_I)^2 + \alpha\,(\Delta K_{II})^2} \tag{4.6}$$

where α is the ratio of the energy release rates, $\Im$, for mode II and I respectively, calculated as proposed in Eqs. 4.7 and 4.8 [89]. In this study the values of α varied from 1.11 to 2.06.

$$\Im_I = -\frac{\pi \Delta K_I}{2} a_{22} Im\left[\frac{\Delta K_I\,(\mu_1+\mu_2)+\Delta K_{II}}{\mu_1\mu_2}\right] \tag{4.7}$$

$$\Im_{II} = \frac{\pi \Delta K_{II}}{2} a_{11} Im\left[\Delta K_{II}\,(\mu_1+\mu_2)+\Delta K_I\mu_1\mu_2\right] \tag{4.8}$$

Since the majority of the propagation occurred in the steady state region of crack growth, also known as region II propagation, the experimental data were fit to the Paris law, Eq. 4.9, and the constants C and n are given in Table 4.3.

$$\frac{da}{dN} = C\left[(\Delta K_{I,eff})^2 + \alpha\,(\Delta K_{II,eff})^2\right]^{n/2} \tag{4.9}$$

In Fig. 4.10 experimental points obtained from regression for the two experiments performed are compared to the results obtained from polycrystal testing, provided by [88]. Despite the different crystallographies, the material shows a common trend, demonstrating the importance of crack-closure in crack propagation. Haynes 230 shows a good fatigue crack growth resistance, compared to other Ni-based superalloys, such as Inconel 718, which exhibits an higher exponential coefficient n (≈4) [93]. The Data-Fitting coefficients proposed in Table 4.3 are in agreement with those reported in literature [60, 94] and demonstrate that fatigue crack growth in Haynes 230 at room temperature is similar to crack propagation in a traditional steel (n ≈3).

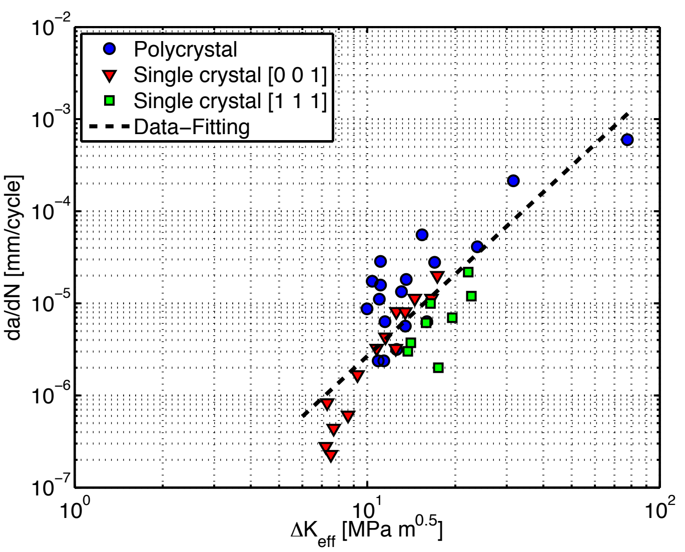

Figure 4.10: *Fatigue crack growth results for polycrystalline and single crystal Haynes 230 specimens at room temperature.*

Table 4.3: *Effective Paris Law fits from fatigue crack growth tests of Haynes 230 alloy. Crack growth rates measured in mm/cycle and stress intensity factor ranges in* $MPa\sqrt{m}$.

Specimen	C	n
[0 0 1] single crystal	1.79 10^{-9}	2.91
[1 1 1] single crystal	8.04 10^{-10}	3.48
Data-fitting	1.55 10^{-9}	2.96

4.4 STRAIN IRREVERSIBILITY AT THE CRACK-TIP

4.4.1 Cyclic plastic zones from extracted stress intensity factor ranges

The extraction of the effective stress intensity factor ranges allowed for the direct estimation of the stress fields acting at the crack tip. Starting from these fields, it was possible to determine the shape and the dimension of cyclic plastic zones [89]. The stresses were computed as:

$$\begin{cases} \sigma_x = \frac{K_I}{\sqrt{2\pi r}}\left(F_{Ix} + tF_{IIx}\right) \\ \\ \sigma_y = \frac{K_I}{\sqrt{2\pi r}}\left(F_{Iy} + tF_{IIy}\right) \\ \\ \tau_{xy} = \frac{K_I}{\sqrt{2\pi r}}\left(F_{Ixy} + tF_{IIxy}\right) \end{cases} \tag{4.10}$$

and the F terms in Eq. 4.10 were calculated as shown in Eqs. 4.11 and 4.12, where $t = K_{II}/K_I$.

$$\begin{cases} F_{Ix} = Re\left[\frac{\mu_1\mu_2}{\mu_1-\mu_2}\left(\frac{\mu_2}{\sqrt{cos\theta+\mu_2 sin\theta}}-\frac{\mu_1}{\sqrt{cos\theta+\mu_1 sin\theta}}\right)\right] \\ \\ F_{Iy} = Re\left[\frac{1}{\mu_1-\mu_2}\left(\frac{\mu_1}{\sqrt{cos\theta+\mu_2 sin\theta}}-\frac{\mu_2}{\sqrt{cos\theta+\mu_1 sin\theta}}\right)\right] \\ \\ F_{Ixy} = Re\left[\frac{\mu_1\mu_2}{\mu_1-\mu_2}\left(\frac{1}{\sqrt{cos\theta+\mu_1 sin\theta}}-\frac{1}{\sqrt{cos\theta+\mu_2 sin\theta}}\right)\right] \end{cases} \tag{4.11}$$

$$\begin{cases} F_{IIx} = Re\left[\frac{1}{\mu_1-\mu_2}\left(\frac{\mu_2^2}{\sqrt{cos\theta+\mu_2 sin\theta}}-\frac{\mu_1^2}{\sqrt{cos\theta+\mu_1 sin\theta}}\right)\right] \\ \\ F_{IIy} = Re\left[\frac{1}{\mu_1-\mu_2}\left(\frac{1}{\sqrt{cos\theta+\mu_2 sin\theta}}-\frac{1}{\sqrt{cos\theta+\mu_1 sin\theta}}\right)\right] \\ \\ F_{IIxy} = Re\left[\frac{1}{\mu_1-\mu_2}\left(\frac{\mu_1}{\sqrt{cos\theta+\mu_1 sin\theta}}-\frac{\mu_2}{\sqrt{cos\theta+\mu_2 sin\theta}}\right)\right] \end{cases} \tag{4.12}$$

Since the single crystal exhibits anisotropic behavior, Hill's extension of the von Mises' yield criterion was used [95]. The yield criterion in quadratic form is expressed as proposed in Eq. 4.13:

$$E\left(\sigma_y-\sigma_z\right)^2+G\left(\sigma_z-\sigma_x\right)^2+H\left(\sigma_x-\sigma_y\right)^2+2L\tau_{xy}^2+2M\tau_{xz}^2+2N\tau_{yz}^2=1 \tag{4.13}$$

where E, G and H are coefficients that characterize the anisotropy in the normal directions and L, M and N are the coefficients that characterize the shear anisotropy. These parameters can be calculated according to Eq. 4.14, where X, Y and Z are the yield stresses in the principal directions and S is the shear yield stress. Assuming plane stress since the specimens are thin, $\sigma_z=\tau_{xz}=\tau_{yz}=0$, Eq. 4.13 reduces to Eq. 4.15.

$$\begin{cases} 2E = -\frac{1}{X^2}+\frac{1}{Y^2}+\frac{1}{Z^2} \\ \\ 2G = \frac{1}{X^2}-\frac{1}{Y^2}+\frac{1}{Z^2} \\ \\ 2H = \frac{1}{X^2}-\frac{1}{Y^2}+\frac{1}{Z^2} \\ \\ 2N = \frac{1}{S^2} \end{cases} \tag{4.14}$$

$$\left(G+H\right)\sigma_x^2-2H\sigma_x\sigma_y+\left(E+H\right)\sigma_y^2+2N\tau_{xy}^2=1 \tag{4.15}$$

To find the plastic zone, Eq. 4.10 is substitute into Eq. 4.15 and solved for the plastic zone radius, r_p. As suggested by Rice [96], cyclic plastic zone radius, Δr_p is evaluated approximately as one quarter of the monotonic r_p, given in Eq. 4.16.

$$\begin{aligned}\Delta r_p=\frac{1}{4}r_p=\frac{\Delta K_{1,eff}^2}{8\pi}[&\left(G+H\right)\left(F_{Ix}+tF_{IIx}\right)^2-2H\left(F_{Ix}+tF_{IIx}\right)\left(F_{Iy}+tF_{IIy}\right)+ \\ &+\left(E+H\right)\left(F_{Iy}+tF_{IIy}\right)^2+2N\left(F_{Ixy}+tF_{IIxy}\right)^2]\end{aligned} \tag{4.16}$$

During measurement cycles, many images were acquired allowing for the observation of the evolution of stresses and strains around the crack tip. The cyclic plastic zone was evaluated according to Eq. 4.16, using the stress intensity factor ranges obtained from regression, while strains were evaluated using DIC. Strains were calculated from the partial derivatives of the displacement fields using Lagrange strain tensor equations. In order to obtain smooth results, displacements were locally approximated with a first-order polynomial. The strains inside the plastic zones are shown in Fig. 4.11 for the loading portion of a fatigue cycle up to maximum load for each specimen tested during this study. The $[0\ 0\ 1]$ crystal case, presented in Fig. 4.11a and b, showed a symmetric plastic zone, since the specimen is under pure Mode I loading. In contrast to the round polycrystalline shape obtained considering isotropic behavior, the anisotropic cyclic plastic zone for a pure Mode I loaded crack showed two marked lobes extending from the crack tip towards the crack flanks. At 50% of the maximum applied load, the cyclic plastic zone area is only 0.00307 mm^2, as shown in Fig. 4.11a. The maximum cyclic plastic zone is shown in Fig. 4.11b and its area is 0.0332 mm^2. In this condition strains around the crack tip are very concentrated and greater than 1%.

The presence of Mode II loading in the $[1\ 1\ 1]$ case caused the cyclic plastic zone shape to be asymmetric. The cyclic plastic zone exhibits two different lobes: the upper one extends at an angle of 87° respect to the horizontal, whereas the lower one is at 77°. At 50% of the maximum applied load (Fig. 4.11c), the cyclic plastic zone extension was 0.0104 mm^2, whereas the maximum area registered was 0.2410 mm^2 (Fig. 4.11 (d)). This is eight times bigger than the one measured in the $[0\ 0\ 1]$ case. Even in this case the strains measured around the crack tip were larger than 1%. The presence of sliding also influenced the strain field, which is asymmetric. An high strain zone started from the crack tip and covered the area in which the crack will propagate, together with a secondary strain area which stayed at 64° under the crack tip.

Cyclic plastic zones in single crystals can be described following several additional methods. In particular, a model based on double slip was employed to describe the effects of crystallographic orientations on the size and shape of the plastic zone in [97]. Haynes 230 being an FCC material, it has been demonstrated that $[1\ 1\ 1]$ oriented crystals can have up to 6 active slip systems and the number of active systems in a $[0\ 0\ 1]$ orientation can be 8. Taking into account the presence of significant slip, the adoption of a continuum model, such as Hill's yield criterion, and its results should only be used as an initial estimation. In the following paragraph the plastic zones obtained from FEM simulation considering single crystal plasticity are proposed and discussed.

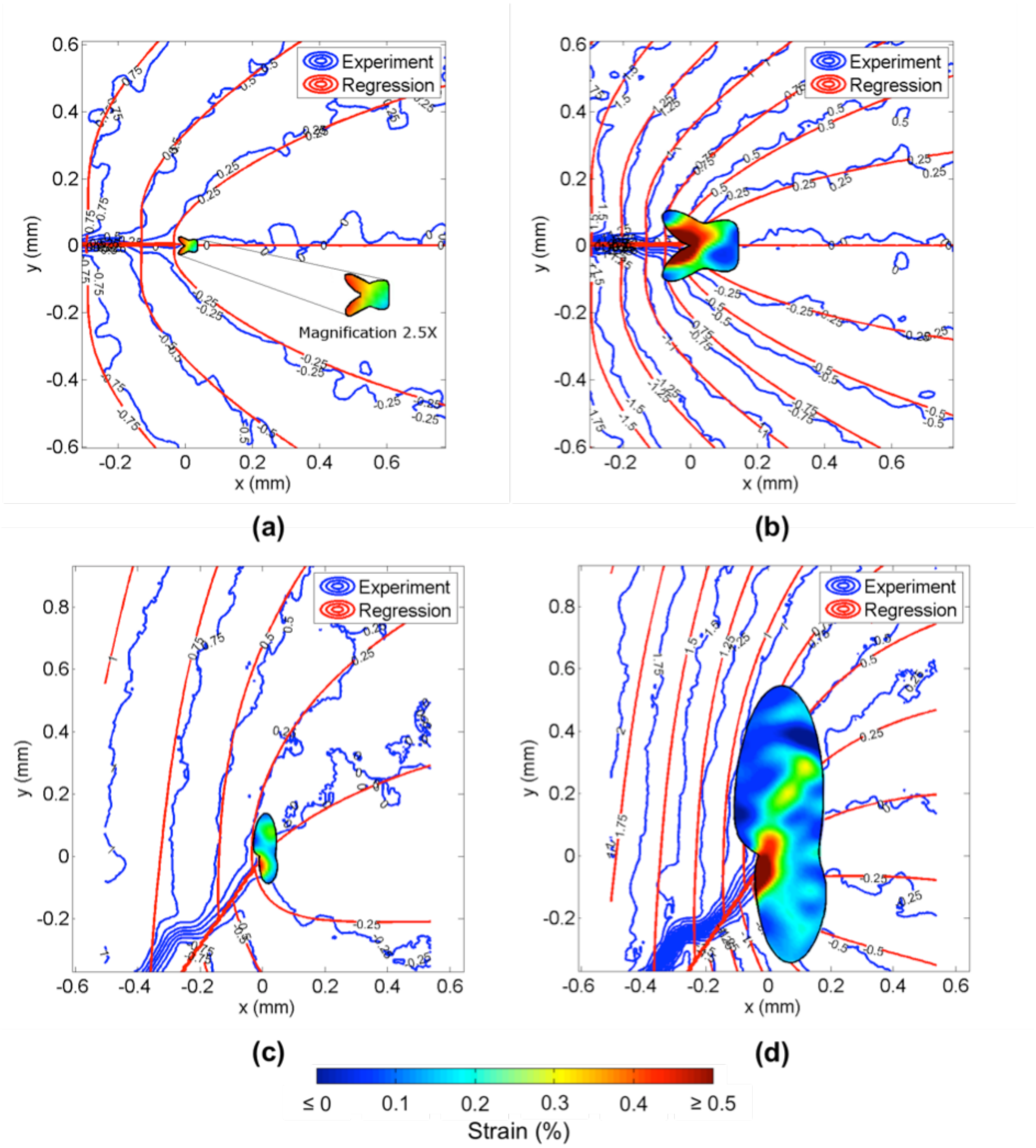

Figure 4.11: *Cyclic plastic zones calculated according to Hill's criterion and vertical contours in micrometers for the two considered orientations. a) and b) :* $[0\ 0\ 1]$ *oriented specimen with a crack length of 0.95 mm with an applied load equal to 50% and 100% of the maximum load, respectively. The cyclic plastic zone area,* $A_{\Delta R_p}$*, at the maximum load is equal to 0.03320* mm^2*. c) and d) :* $[1\ 1\ 1]$ *oriented specimen with a crack length of 1.66 mm with an applied load equal to 50% and 100% of the maximum load, respectively.* $A_{\Delta R_p}$ *at the maximum load is equal to 0.2410* mm^2

4.4.2 Cyclic plastic zones from numerical simulations with single crystal plasticity

Inelastic deformation and crack propagation in single crystals are related to the irreversibility of slip. An accurate analysis of the area surrounding the crack tip should take into account single crystal mechanical behavior and an approach based on continuum mechanics, like the one presented in the previous section, should be taken only as a preliminary result. In this section, a brief analysis of the crystal plasticity model adopted for plastic zone evaluation is given, together with the numerical results obtained for the two tested crystal orientations.

The kinematical theory of crystals is mainly due to the initial work of Taylor [98] and the mathematical formulations by Hill [99], Rice [100], Hill and Rice [101] and Asaro, Needleman and Peirce [102]. In this framework the crystal deforms by two distinct mechanisms:

- plastic deformation, which consists of material shearing relative to a crystal lattice;
- elastic deformation of the lattice and material together.

In crystal plasticity theory, the deformation gradient F is not given by the sum of an elastic and a plastic part, but is evaluated as the product of the deformation gradient associated to elastic loading, F^*, and of the deformation gradient that takes into account inelastic strains, F^p, adopting the multiplicative decomposition originally proposed by Lee [103]:

$$F = F^* \cdot F^p \tag{4.17}$$

The main assumption of this model is that inelastic deformation is solely due to plastic shearing in crystallographic slip systems, as proposed in Eq. 4.18, where $s^{(\alpha)}$ and $m^{(\alpha)}$ are respectively, the slip direction and the normal to slip plane of the α-th slip system, and $\dot{\gamma}^{(\alpha)}$ is the associated slip rate.

$$\dot{F}^p \cdot F^{p-1} = \sum_{\alpha} \dot{\gamma}^{(\alpha)} s^{(\alpha)} m^{(\alpha)} \tag{4.18}$$

The crystalline slip is modeled to obey Schmid's law: the slipping rate $\dot{\gamma}$ in each α-th slip system is related to the external applied stress through the Schmid stress, τ, which is the resolved shear stress when the elastic deformations can be neglected, as

$$\dot{\gamma}^{(\alpha)} = a \left(\frac{\tau^{(\alpha)}}{g^{(\alpha)}} \right)^{z} \tag{4.19}$$

where a is a constant, $g^{(\alpha)}$ is a variable describing the current strength of the α-th slip system and z is the rate sensitivity exponent. The increment in the yield strength of each slip system follows what is proposed in Eq. 4.20, where $h_{\alpha\beta}$ is the hardening matrix.

$$\dot{g}^{(\alpha)} = \sum_{\alpha} h_{\alpha\beta} \dot{\gamma}^{(\beta)} \tag{4.20}$$

The diagonal terms of the hardening matrix are called self-hardening moduli, whereas the extra-diagonal terms are defined as latent hardening moduli. Pierce, Asaro and Needleman proposed a simple form for the self-hardening moduli [102]:

$$h_{\alpha\alpha} = h_0 sec\, h^2 \left| \frac{h_0 \gamma}{\tau_s - \tau_0} \right| \tag{4.21}$$

where there is no sum on α and h_0 is the initial hardening modulus, τ_0 is the yield stress which equals the initial value of the current strength $g^{(\alpha)}(0)$, τ_s is the stress where large plastic flow initiates, and γ is the Taylor cumulative shear strain on all slip systems:

$$\gamma = \sum_{\alpha} \int_0^t \left| \dot{\gamma}^{(\alpha)} \right| dt \tag{4.22}$$

The latent hardening moduli are considered as a fraction of the self-hardening moduli, as expressed in Eq. 4.23.

$$h_{\alpha\beta} = q h_{\alpha\alpha} \qquad (\alpha \neq \beta) \tag{4.23}$$

In the case of this study the value of the constant q is assumed to be equal to zero, so no interaction between the slip systems is considered. Single crystal plasticity behavior is implemented in a commercially available software (Abaqus by Dassault Systemes) in terms of a UMAT external subroutine. A description of the subroutine is given in [104].

Numerical models implementing crystal plasticity were developed for the two tested crystal orientations. Material constants, necessary to simulate material inelastic behavior, were obtained by fitting experimental tensile stress/strain curves obtained from unnotched Haynes 230 single crystals. In particular, a numerical model was implemented to simulate the tensile test performed on the $[1\ 1\ 1]$ oriented crystal. Material constants were chosen in order to fit the experimental curve (Fig. 4.12a). At this point, a new model representing the $[0\ 0\ 1]$ crystal was implemented and checked with the constants obtained from the $[1\ 1\ 1]$ model. Numerical results are in good agreement with those experimentally obtained, as shown in Fig. 4.12b. Material constants obtained following this procedure are reported in Table 4.4.

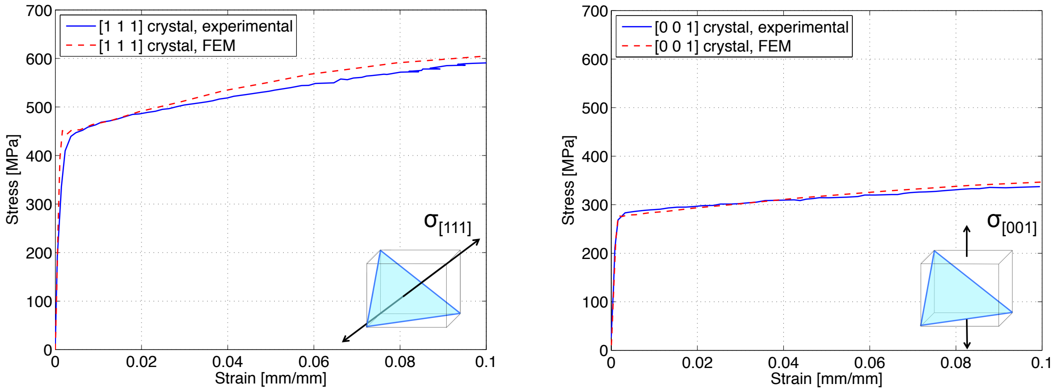

(a) **(b)**

Figure 4.12: *Comparison between experimental and numerical results of Haynes 230 single crystal tensile behavior. a)* $[1\ 1\ 1]$ *oriented crystal; b)* $[0\ 0\ 1]$ *oriented crystal.*

Table 4.4: *Coefficients employed for FEM simulations.*

a	z	h_0	τ_s	τ_0
0.001	10	155	130	80

At this point, models of the cracked specimens were implemented. Simulations were performed on 2D-models and plane stress was assumed, since the specimens are thin. Crack lengths considered in these simulations were the same as those analyzed in the previous section in order to make a comparison between the two. In Fig. 4.13, a schematic of the model employed for the simulation of the $[0\ 0\ 1]$ oriented crystal is reported. Only the part of the specimen which stays between the two clamps is modeled. The upper clamp is modeled by neglecting the horizontal and the vertical displacements of the upper edge of the model. The force is then applied to the model through a reference point, which constrains the vertical and horizontal displacements of the lower edge of the model. Horizontal and rotational degrees of freedom of the reference point are then neglected, in order to avoid horizontal translations and rotations. In order to increase model accuracy, 8-nodes quadratic elements were adopted and an element dimension of 5 μm around the crack-tip was considered.

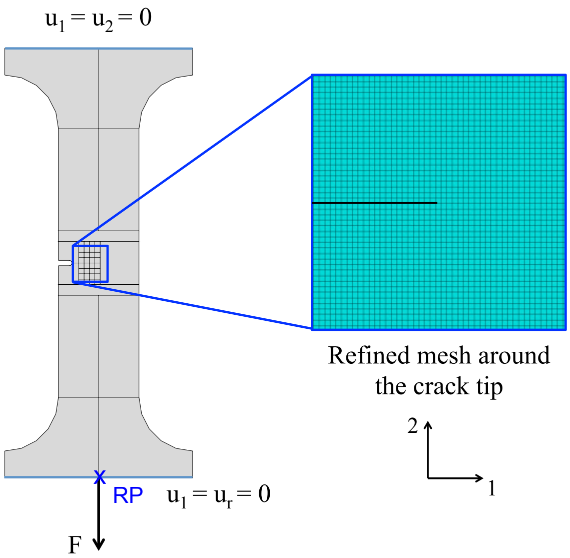

Figure 4.13: *FEM model for the simulation of the cyclic plastic zone of the* $[0\ 0\ 1]$ *oriented single crystal.*

Since in the considered plasticity model there is no explicit yielding, the extension of the plastic zone was evaluated considering Hill's anisotropic yield criterion. Eq. 4.16 was employed during these calculations. The cyclic plastic zone was obtained considering $\Delta r_p = 1/4 r_p$, as suggested by Rice [96].

In Fig. 4.14a the results obtained for the $[0\ 0\ 1]$ oriented crystal are presented. Respective to the cyclic plastic zone obtained from DIC displacements, the plastic zone presents a similar shape. In this case the lobes extending towards the cracks flanks are smaller. As expected, the plastic zone shape is symmetric, since no Mode II was experienced during the test, and its size is smaller, 0.0116 mm^2 versus the 0.0307 mm^2 measured according to DIC. The vertical strains measured by DIC inside the cyclic

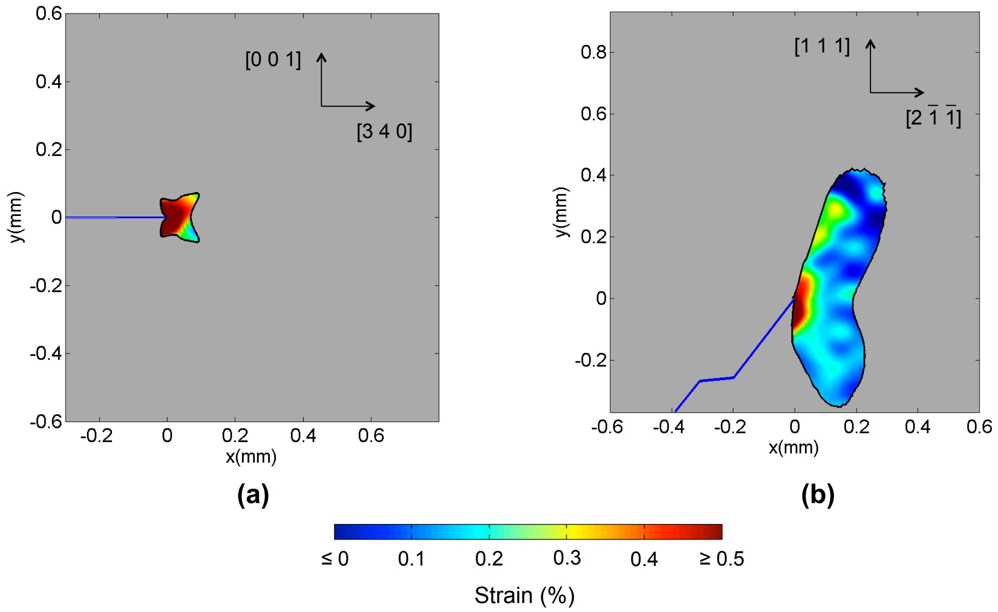

Figure 4.14: *Cyclic plastic zone calculated from single crystal plasticity simulation. a)* $[0\ 0\ 1]$ *specimen with a 0.96 mm long crack. Cyclic plastic zone extension,* $A_{\Delta r_p}$*, is equal to 0.0116* mm^2*. b)* $[1\ 1\ 1]$ *specimen with a 1.66 mm long crack. Cyclic plastic zone extension,* $A_{\Delta r_p}$*, is equal to 0.1455* mm^2*.*

plastic zone are in agreement with the numerical results, as strains are rapidly decreasing moving from the crack- tip. The maximum shear stress measured at the crack-tip is 324 MPa.

As observed in the previous section, the cyclic plastic zone obtained from numerical simulation for the $[1\ 1\ 1]$ orientation is also asymmetric, as shown in Fig. 4.14b: following the same pattern, the main lobe of the plastic zone extends in the upper part of the specimen. The farthest point from the crack tip is at 62° from the horizontal. The angle calculated by FEM analysis is smaller than the one provided by Hill's criterion. The same observations can be made with the small lobe, which extends under the crack-tip at 67°. The cyclic plastic zone calculated by FEM extends for 0.1455 mm^2 around the crack-tip and, confirming what observed in the [001] case, is smaller than the one calculated from experimental displacements. The cyclic plastic zones obtained from FEM for the two different orientations have a different extension, confirming the observations obtained analyzing the experimentally measured zones. The maximum shear stress is calculated at the tip and is 357 MPa.

4.5 CONCLUSIONS

In this study, fatigue crack growth at room temperature in Haynes 230 single crystals was analyzed. In particular, several different techniques were employed:

- Stress intensity factor ranges (Modes I and II) were calculated with a least-squares regression technique, starting from the displacements measured by DIC. Results were compared with those obtained from polycrystalline experiments, displaying a similar behaviour.

- Crack tip opening/sliding displacements were measured by observing the relative displacements of the crack flanks with two-point virtual extensometers. Both the cracks opened at 20% of the maximum applied load. During mixed mode propagation Mode II sliding was observed before Mode I opening.

- Anisotropic Hill's yield criterion was adopted to obtained an initial estimate of the cyclic plastic zone around the crack tip. Results were compared with the strains measured by DIC. The cyclic plastic zone calculated for the $[0\ 0\ 1]$ specimen was eight times smaller than the one observed for the $[1\ 1\ 1]$ orientation.

- Numerical simulations were carried out to calculate the plastic zone around the crack tip, considering single crystal plasticity. The results showed good agreement with the measured strains for the same effective K-loads. Consistent with the experimental results, the cyclic plastic zone around the crack tip of the $[1\ 1\ 1]$ was greater than the one observed in the $[0\ 0\ 1]$ case, underlining the importance of ΔK_{II} in cyclic plastic zone shape and size.

CHAPTER 5

Short crack propagation in line pipes material under severe loading conditions

5.1 INTRODUCTION

In this chapter, fatigue crack growth in line pipes material is investigated. Line pipes are employed in challenging harsh environments, where they have to sustain severe loading conditions. Especially when working in arctic-like environments, line pipe materials can be subjected to plastic straining cycles due to thermal cycling between service and shutdown and to occasional large plastic deformations induced by ice scouring in shallow water [105–107].

Fatigue properties (fatigue strength and life) can be conservatively predicted, assuming the presence of small shallow cracks with a depth corresponding to the NDT detection limit [108].

From this background, the effect of severe strain cycles onto line pipe steel was analyzed as propagation of prospective flaws in the very short LCF regime. Experimental results allowed the development of a crack propagation model for materials subjected to severe strain cycles.

The different phases of the experimental activity were:

- Short crack propagation on small scale specimens. In this phase, specimens with a net section of 12 mm x 7 mm were cyclically loaded. Semi-circular defects, whose depth was $400\mu m$, were used for testing. These experiments were performed in order to check both material cyclic behavior and the crack propagation model presented in Chapter 2;
- Crack closure measurement during short crack propagation. An experimental technique was developed to measure crack opening and closing levels and checked

on a new series of experiments performed on small scale specimens. These tests were employed to evaluate the accuracy of Newman's analytical model and to extract the da/dN - ΔJ_{eff} curve;

- Short crack propagation on large scale specimens. Crack closure levels were measured during fatigue tests performed on specimens with a net section of 43 mm x10 mm. In this phase, 0.7 mm deep and 7 mm wide notches were considered, in order to check crack propagation with constraint levels similar to those of pipelines. A specimen with a 1.4 mm deep defect was also tested, in order to analyze crack propagation under more severe loading conditions;
- Fatigue life assessment of large scale specimens. Fatigue lives of notched specimens were assessed by implementing a crack propagation model based on the effective J-Integral range. ΔJ formulation was modified in order to take into account the geometry of large scale specimens, whereas the experimental da/dN - ΔJ_{eff} curve evaluated from small scale testing, together with the closure levels measured on large scale specimens, was employed to evaluate crack growth rates evolution.

5.2 EXPERIMENTS ON SMALL SCALE SPECIMENS

5.2.1 LCF conditions

An activity carried out on heavy wall linepipes [105–107] identified a critical cycling sequence. Cycling has been defined as the superposition of one strain ramp in material plastic regime, up to 1%, superposed to a sub-cycling at 0.5% of the total strain, for a limited number of cycles (≈200). These multi-plastic straining cycles aim at reproducing situations that can occur during pipeline life in artic-like environments.

In order to set-up a crack propagation model for prospective flaws in linepipes subjected to severe straining cycles, two series of tests on small scale specimens were carried out:

- strain cycles from 1% to 0.5%;
- strain cycles at R = -1 with ϵ_a = 0.35%.

The latter test condition was chosen as a reference condition, since a good performance of the ΔJ_{eff} model was obtained under fully reversed strain cycles.

In Fig. 5.1, material cyclic behavior, recorded during the experiments performed under the two different strain conditions, is reported. As it can be seen, material exhibits a transient behavior. In particular, mean stress relaxation is observed during the tests performed at R = 0.5, as depicted in Fig. 5.1a, where it is also shown that, at the end of the test, the applied mean stress tends to zero.

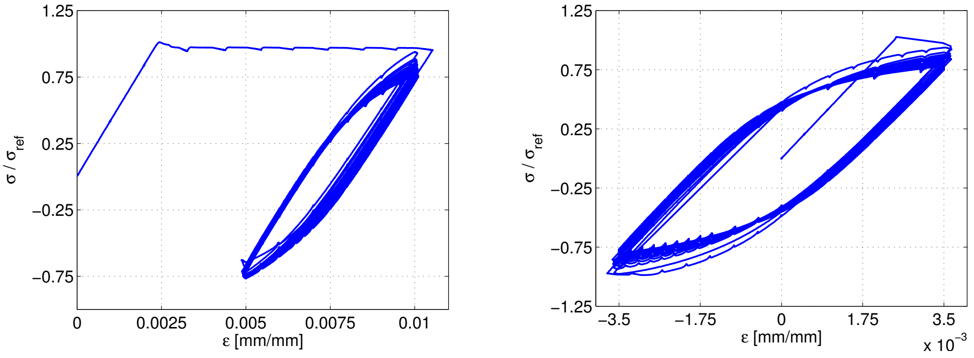

(a) (b)

Figure 5.1: *Hysteresis loop evolution during LCF testing. a) Test performed at R = 0.5 and ϵ_a = 0.0025 mm/mm; b) Test performed at R = -1 and ϵ_a = 0.0035 mm/mm.*

5.2.2 Specimen preparation

An experimental campaign was carried out to observe crack propagation in specimens containing artificial notches. 0.4 mm deep semi-circular defects, obtained by Electrical Discharge Machining (EDM), were employed during the experiments. The geometry of the specimens used for testing is reported in Fig. 5.2a, where artificial defect shape and orientation are also shown. Tests were performed on a MTS Landmark servo-hydraulic load frame: a longitudinal extensometer, with a 10 mm long gauge, was employed to control the applied strain amplitudes. The experimental setup is shown in Fig. 5.2b.

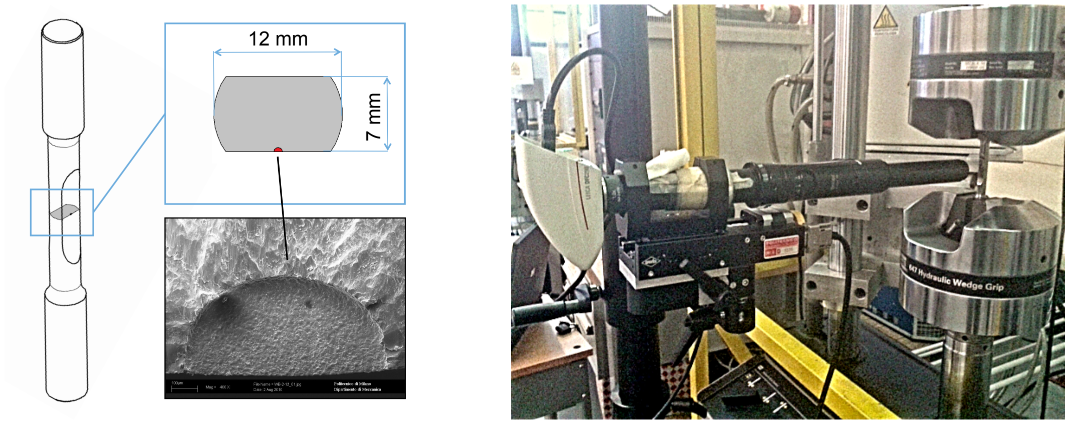

(a) (b)

Figure 5.2: *LCF testing under severe loading conditions. a) Specimen geometry and micro-notch shape and orientation (depth 400 μm); b) Experimental setup with the digital camera employed to observe crack propagation during the experiment.*

Before testing, specimens were precracked, in order to obtain a sharp fatigue crack. Precracking was deemed necessary, in order to remove crack nucleation time from the experiments. The compression pre-cracking constant amplitude (CPCA) technique, originally proposed by Newman [109], was employed in this phase. According to this technique, after compression pre-cracking the crack has the same size of the plastic zone generated around the notch during the first compressive load cycle. Because of this, a numerical analysis of one quarter of the specimen was performed to calculate the load that causes a plastic region of 100 μm, the desired size of the precrack. It was found that a remote compressive stress of 400 MPa generates a 120 μm-wide plastic zone around the notch, as depicted in Fig. 5.3a. Because of this, specimens were precracked in compression, with a fixed load ratio equal to 0 and a stress amplitude equal to 200 MPa. It was observed (Fig. 5.3b) that all the specimens, after precracking, exhibited an average 100 μm long defect extending from both the sides of the EDM notch, confirming the numerical observations.

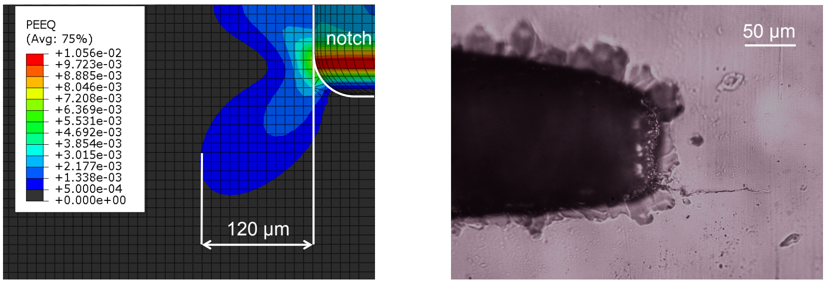

(a)

(b)

Figure 5.3: *Compression precracking. a) Plastic zone around the notch, FEM calculations with an applied compressive stress of 400 MPa; b) Fatigue pre-crack after 500000 cycles.*

5.2.3 Fatigue tests

Four samples were cyclically loaded: constant strain amplitude tests were performed under the loading conditions described in section 5.2.1. One specimen was tested at $R = -1$, whereas the other three were loaded at $R = 0.5$, the most demanding in-service condition. All the tests were performed with a frequency of 0.5 Hz and were interrupted when a surface crack length equal to 2 mm was reached.

A fifth specimen was tested at $R = 0.5$: this test was interrupted after 200 cycles, in order to analyze the fracture surface in the early propagation stage. A SEM analysis of the fracture of this specimen is reported in Fig. 5.4a, where it can be seen that the crack initially propagates in the direction of the plastic zone generated by the first strain step.

Crack length was measured during tests interruptions by adopting two different techniques: defect size was initially measured with the plastic replica technique discussed in chapter 2: an example of the fracture surface is presented in Fig. 5.4b. The so-obtained crack lengths were then compared to those measured from the pictures acquired by an HD digital camera, whose resolution was 1600x1200 pixels. After the end of the first test, crack length was measured only from the digital images, since this technique provided satisfactory results and it allowed to reduce the time required for testing. A magnification of 15X, obtained using an adjustable lens with a 6.5X magnification range and a 10X adapter, was employed during the experimental campaign. This setup allowed a resolution of 2 $\mu m/pix$.

After the end of the tests, specimens were broken in liquid nitrogen in order to

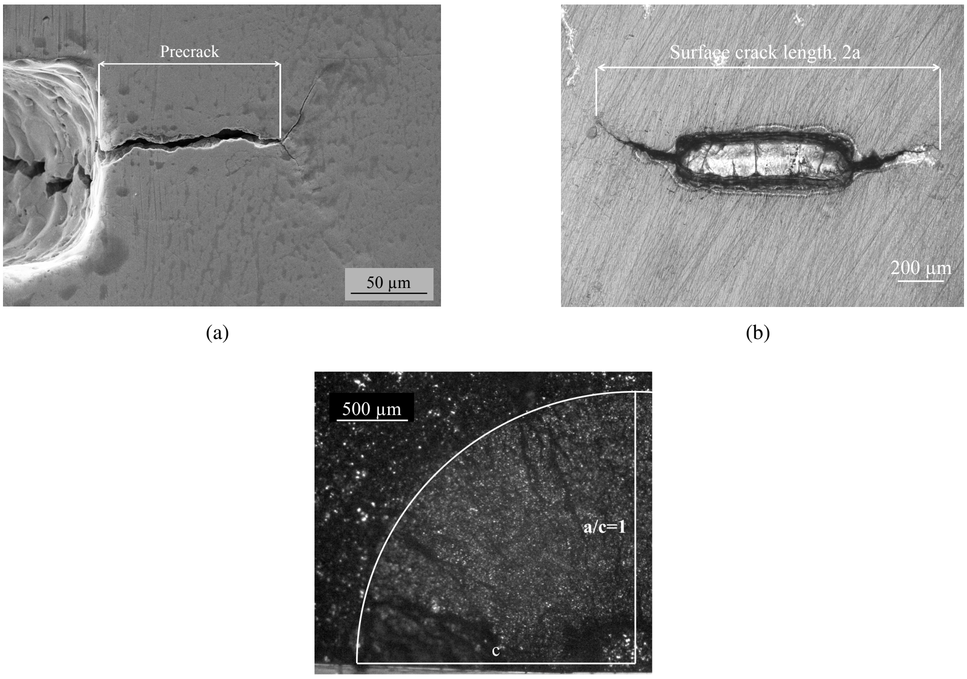

(a)

(b)

(c)

Figure 5.4: *Fracture surfaces during fatigue crack growth. a) Fracture surface in the early propagation stage; b) Surface crack propagation on a sample surface, observed on a plastic replica; c) Fatigue crack surface after the end of the experiment.*

observe the final shape of the defect. Since all the specimens exhibited a semi-circular fatigue crack, as shown in Fig. 5.4c, it was assumed that the aspect ratio remained constant during propagation (i.e. $a/c = 1 = const.$). Therefore, the defect size, a, was calculated as one half of the surface defect size, $2c$, and experimental crack growth rates, da/dN, were then derived by applying the $secant\ method$.

5.2.4 Test results

Experimental results were analyzed considering the model based on ΔJ_{eff} proposed in Chapter 2. Eq. 2.16 [3,35] was adopted, since it has been demonstrated to introduce the smallest scatter and to be consistent at room temperature. Effective J-Integral ranges were extracted from stress/strain hysteresis loops. In order to take into account material initial behavior, a feature that becomes important in very low cycle fatigue, the stress and strain amplitudes, necessary for ΔJ_{eff} calculations, were extracted from the cycle at which the crack length was measured. This allowed a more correct estimation of the effective J-Integral range, since the material, during the tests, presented a transient behavior, as shown in Fig. 5.1.

Crack closing and opening levels were calculated according to the model proposed by Newman [5], considering a constraint factor α equal to 1, whereas the flow stress, σ_0, was calculated following Vormwald's formulation [3], as expressed in Eq. 5.1, where $R'_{p,02\%}$ is the cyclic yield stress and R_m is the ultimate tensile strength.

$$\sigma_0 = \frac{1}{2}\left(R'_{p,02\%} + R_m\right) \tag{5.1}$$

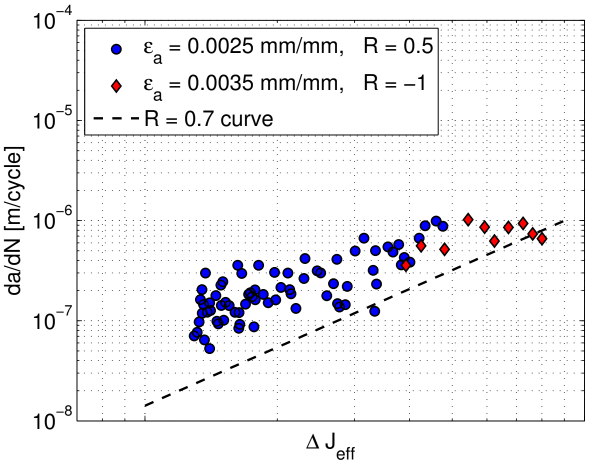

Figure 5.5: *Fatigue crack growth analysis based on ΔJ_{eff} [3]. Crack opening and closing levels calculated according to Newman [5].*

In Fig. 5.5 experimental crack growth rates are plotted against ΔJ_{eff} and are compared to the trend line from da/dN - ΔK_{eff} data obtained from a C(T) specimen tested at an high stress ratio (R = 0.7). As it can be seen, experimental data-points do not lie on the ΔK_{eff} curve.

Two possible reason were identified as responsible for a crack growth much higher than the predictions:

- A damaged zone ahead of crack, suggested by the appearance of intense plastic deformation during propagation (Fig. 5.6);
- A non correct evaluation of the closure levels.

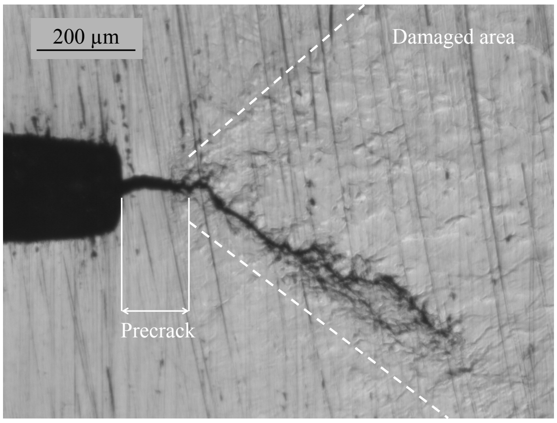

Figure 5.6: *An image of the fracture taken with the optical microscope during a fatigue test.*

A numerical analysis with the Gurson, Tvergaard and Needleman (GTN) model [110, 111] was performed to investigate the possible nucleation, growth and coalescence of small voids near the crack tip. The results of this investigation, provided in Appendix A, showed that the plastic strains present ahead of the tip are not responsible for the growth acceleration, since they are not high enough to initiate the damage mechanism in the crack tip region. Because of this, the attention was shifted on crack closure. A wrong estimate of crack opening and closing levels can change the value of the effective stress and strain ranges, implying a reduction of the calculated ΔJ_{eff}: because of this, a new experimental campaign was performed in order to evaluate crack closure levels. The results of this analysis are reported in the following section.

5.3 CRACK CLOSURE MEASUREMENTS IN LCF WITH DIGITAL IMAGE CORRELATION

An experimental campaign was performed in order to measure crack opening and closing levels during short crack propagation. Crack closure was characterized with digital image correlation. Four experiments were conducted on the specimen geometry presented in Fig. 5.2a: the first two tests were performed at R = -1, whereas the remaining two were cyclically loaded at R = 0.5, considering the strain amplitudes discussed in Section 5.2. The final surface crack length, necessary to consider a test as concluded, was increased to 4 mm, in order to acquire more data-points. Before testing, specimens were prepared by manually polishing the surface to a mirror finish with abrasive paper, up to a grit of P2500. A speckle pattern, necessary for digital image correlation, was painted onto each specimen with an airbrush, following the procedure discussed in Chapter 4. During test interruptions, necessary to measure crack advancement, a fatigue load cycle was manually performed in order to acquire several pictures of the crack. The displacement field was then calculated by correlating the images taken during the fatigue cycle with the reference image, which was the first picture of each measurement cycle, taken at the minimum applied strain.

In the literature, DIC has been widely adopted to evaluate crack closure. All the presented techniques, however, were implemented considering crack propagation during HCF, when LEFM conditions can be assumed: the full field regression algorithm [2, 59, 60, 88] presented in Chapter 4, for example, can be employed only when the plastic zone around the tip is small compared to the crack itself, since it fits experimental displacements with the analytical K-field, calculated considering material elastic behavior. On the other hand, it is important to develop a method to measure crack opening and closing levels when low cycle fatigue is considered, since it has been proved [3, 4, 34, 64] that crack closure plays an important role even in elastic-plastic propagation. Because of this, several techniques based on two-points digital extensometers and on strain gauges were applied. Experimental results are discussed in the following sections.

5.3.1 Virtual extensometers

In order to evaluate closure levels, the technique based on two-points virtual extensometers discussed in Chapter 4 was implemented, as shown in Fig. 5.7a. Such a technique, however, did not provide satisfactory results. In particular, it was not possible to evaluate crack opening and sliding levels, since the measured crack-opening displacement (COD) provided an hysteresis loop, as shown in Fig. 5.7b, where the measurements provided by a virtual extensometer positioned 50 μm behind the tip are presented.

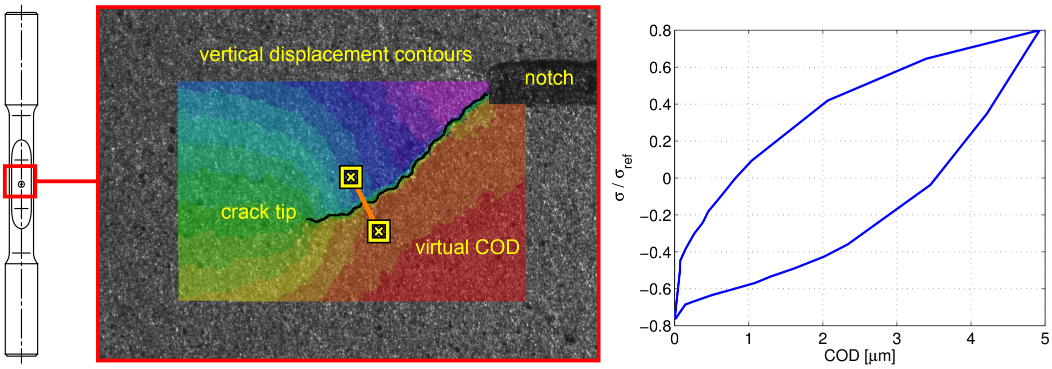

(a)

(b)

Figure 5.7: *Crack closure measurements with two-point digital extensometers. a) Disposition of the extensometer on the two crack flanks; b) Force vs COD plot. The extensometer was positioned 50 μm before crack tip.*

5.3.2 Virtual strain gauges

A different technique was implemented in order to evaluate crack closure. In one of their works [3], Vormwald and Seeger proposed an experimental technique to measure crack opening and closing levels during constant strain amplitude tests. This technique consists in placing a strain gage as close as possible to a fatigue crack: the so-measured local stress/strain cycle is compared with the global one, which is the fatigue cycle measured by the external extensometer, which controls test execution. Crack opening and closing levels can be estimated as the points in which local and global hysteresis loops start to differ. The difference between global and local behavior is related to the change of specimen compliance: when the crack stays closed, the zone surrounding the fracture behaves in the same way of those parts far from the defect, whereas it looses stiffness when the crack starts opening. In particular, when the crack stays open, the strains locally measured are smaller than those remotely recorded, since the gage stays in the strain shadow of the crack.

In this work, crack closure effects were experimentally investigated through a similar approach, but using an innovative technique based on DIC. Initially, a 300 μm-wide series of virtual strain gages was positioned under the EDM notch, as proposed in Fig. 5.8a. The gauges were set to read axial strains, following Vormwald's original proposal. The measurements provided by the virtual gage are compared to the remote strains measured by the extensometer in Fig. 5.8b: this approach does not provide any result, since that part of the specimen does not carry any load. Trying to obtain a correct estimate, the strain gauge was moved in the cyclic plastic zone, very near to the crack tip, as depicted in Fig. 5.8c: the strains evaluated in this zone are depicted in Fig. 5.8d, where it can be seen that even in this case it is not possible to assess opening and closing levels, due to the high strains present near the tip.

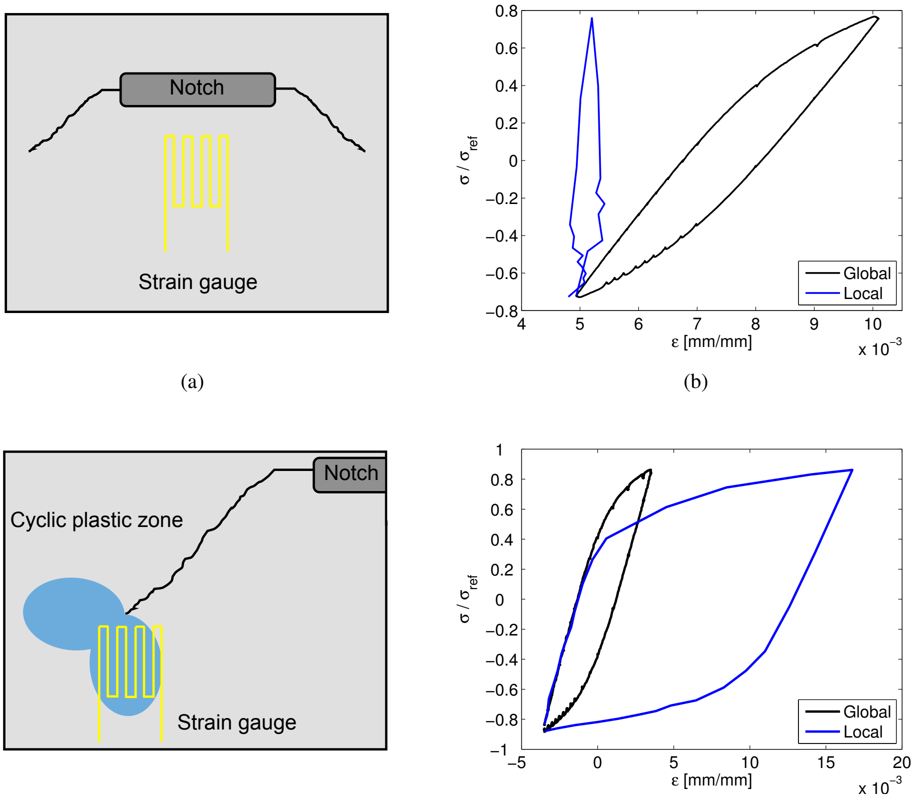

(a) (b)

(c) (d)

Figure 5.8: *Crack closure measurements in LCF with DIC. a) Virtual strain gauge position, Vormwald's proposal [3]; b) local stress/strain loop measured under the EDM notch; c) Virtual strain gauge position near crack-tip. d) local stress/strain loop measured in the cyclic plastic zone.*

In order to get an accurate measurement, the virtual strain gauge was moved between the cyclic plastic zone and the notch (Fig. 5.9a): the strain values measured in this zone can be used to calculate crack opening and closing levels, as it can be seen in Fig. 5.9b. Moreover, the method showed to be consistent: a 50 μm change in the horizontal position of the strain gauge did not affect the recorded closure levels, confirming the extracted closure values.

This technique, however, present a limitation, related to the applied loading conditions: the presence of high strain implies a great vertical displacement of the measurement surface. This means that the magnification employed for image acquisition is limited by the vertical travel of the defect during the fatigue cycle and that only a small portion of the area surrounding the tip can be monitored. During the experiments, it was found that for the current setup the maximum allowable magnification, satisfactory for DIC measurements, is 30X, which corresponds to a resolution of 1 $\mu m/pix$.

At this point, the technique was applied to the experiments, positioning the virtual strain gauges at 150 μm from crack-tip, since it was found that this position provides best results: an example of the crack closure measurements, obtained during small scale testing, is provided in Fig.5.10a and b. Crack opening and closing levels can be easily recognized and occur at the same strain level. These observations confirm the

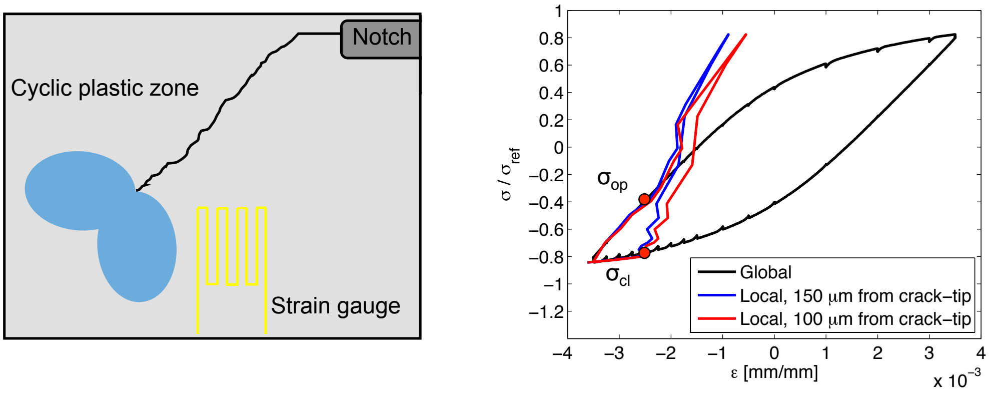

(a) (b)

Figure 5.9: *Crack closure measurements in LCF with DIC. a) Virtual strain gauge position adopted for crack closure estimates; b) comparison between local and global hysteresis loops and opening and closing levels identification.*

measurements presented by Vormwald [3] and the validity of his concept.

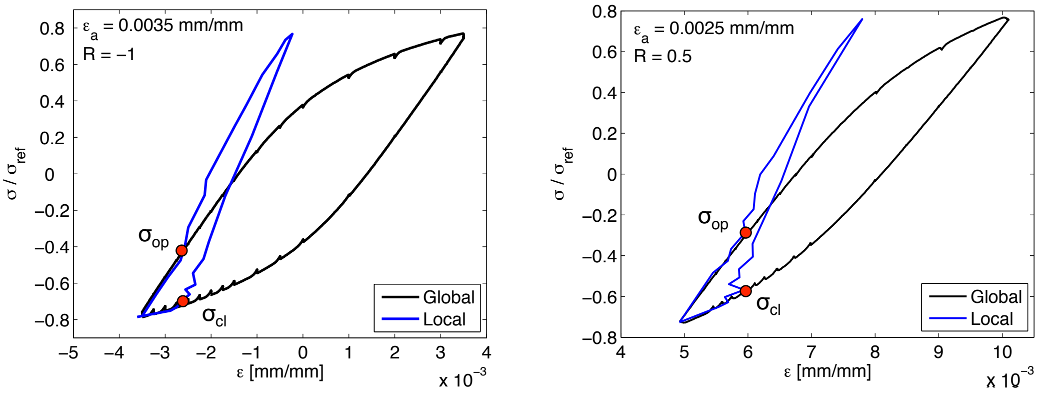

(a) (b)

Figure 5.10: *Crack closure measurements in LCF with DIC on small scale specimens. a) comparison between local and global hysteresis loops and opening and closing levels identification for tests conducted at R = -1; b) comparison between local and global hysteresis loops and opening and closing levels identification for tests conducted at R = 0.5.*

5.3.3 Results

Experimental results were compared to those obtained considering Newman's analytical model. As it can be seen in Fig. 5.11a, the model, when R = -1 tests are considered, correctly estimates the value of the effective stress range, providing a small error ($\approx 5\%$). On the other part, greater errors are present when tests with a mean strain are considered (Fig. 5.11b). In particular, for those tests performed at R = 0.5, the model underestimates the value of $\Delta\sigma_{eff}$: this implies that a procedure based on Newman's formulation underestimate the applied effective J-Integral range. In order to verify if the model can be improved, a different formulation of the flow stress was implemented [22]: the value of σ_0, calculated according to Eq. 5.1, was replaced by the cyclic yield stress. This new formulation, represented in Fig. 5.11 by a dashed line, offer a small improvement, since it increases the value of $\Delta\sigma_{eff}$ in both the considered conditions, but it still provides wrong estimates when tests with an applied mean strain are considered.

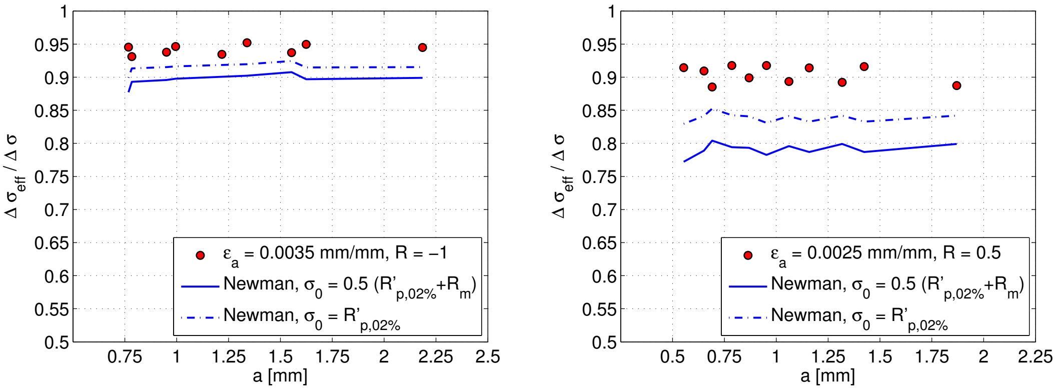

(a) (b)

Figure 5.11: *Comparison between experimental and analytical effective stress amplitudes, small scale specimens. a) R = -1, ϵ_a = 0.0035 mm/mm; b) R = 0.5, ϵ_a = 0.0025 mm/mm.*

In Fig. 5.12, experimentally observed crack growth rates are plotted against the effective J-Integral ranges, calculated considering the effective stress and strain amplitudes measured with DIC: all the experimental points collapse on a single curve, which has the same trend of the da/dN - ΔK_{eff} curve obtained testing a C(T) specimen at high load ratio (R = 0.7).

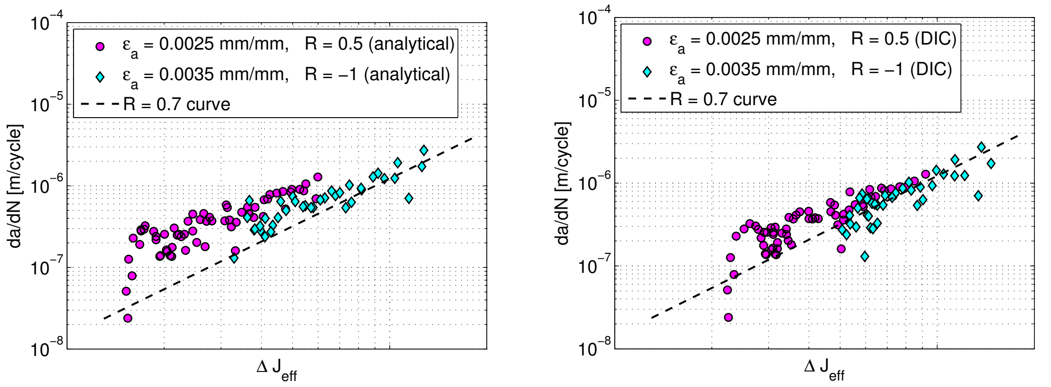

(a) (b)

Figure 5.12: *Fatigue crack growth analysis based on ΔJ_{eff} [3]. a) Crack opening and closing levels calculated according to Newman; b) Crack opening and closing levels calculated from DIC measurements.*

5.4 FATIGUE CRACK GROWTH IN LARGE SCALE SPECIMENS

5.4.1 Experiments

The experimental analysis of fatigue crack growth on small scale specimens underlined the capability of ΔJ_{eff} based models to accurately describe crack propagation under severe loading conditions. At this point, larger specimens were tested, in order to check the propagation model when artificial defects with a constraint similar to that estimated for linepipes are present. A schematic of the specimen used for testing, together with the shape and the orientation of the artificial defect, is presented in Fig. 5.13a. The defects adopted in this phase were 7 mm wide, whereas two different depth were considered: initially, four specimens containing a 0.7 mm deep notch were fatigue tested, whereas a final experiment was performed on a specimen with a 1.4 mm deep defect. Two different ranges of artificial defect dimensions were chosen to evaluate the constraint change effect during propagation. In the following part of this chapter, this geometry will be referred as $large\ scale$.

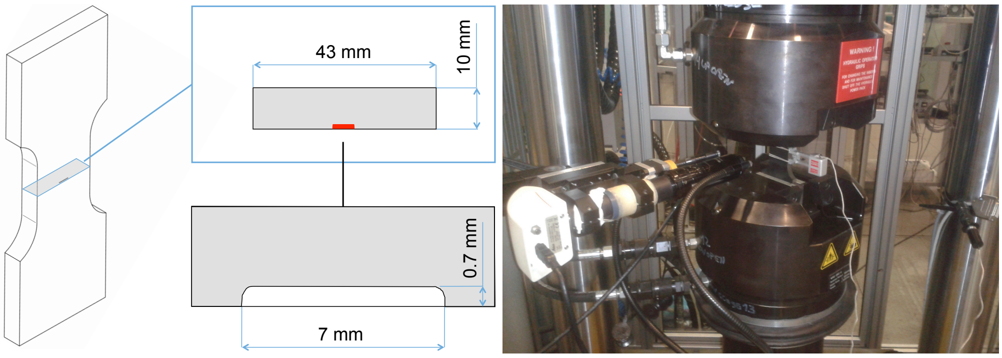

(a) (b)

Figure 5.13: *LCF testing on large scale specimens. a) Schematic of the large scale specimen, together with micro-notch geometry and disposition. b) The specimen mounted in the 250 kN load frame.*

Before testing specimen were prepared following the procedure discussed in the previous section: initially, specimens were mechanically polished, painted and then precracked in compression. At this point, specimens were tested in a 250 kN servo hydraulic load frame. A longitudinal extensometer, with a 20 mm long gage, was employed to control the applied strain amplitude. Experimental setup is shown in Fig. 5.13b. Specimens were cyclically loaded adopting the same levels discussed in Section 5.2. Two tests for each loading condition were performed on the samples containing 0.7 mm deep defects, whereas the specimen with the greater defect was tested at R = 0.5.

5.4.2 Results

Crack opening and closing levels were measured according to the technique presented in Section 5.3. In Fig. 5.14 two selected fatigue load cycles, employed for crack closure analysis, are reported. A measurement cycle obtained from R = -1 testing is reported in Fig. 5.14a: the experimental technique is cabaple of measuring the crack opening level, but the method looses accuracy when the descending part of the hysteresis loop is considered. The same observations can be made considering the measurement cycle obtained from R = 0.5 testing (Fig. 5.14b). This can be related to the fact that DIC allows to measure crack opening and closing levels only on the surface of the specimens. It can be assumed that the plane stress condition occurs for these external points, whereas the remaining part of the crack front is experiencing a stress condition similar to plane strain. This means that crack opening and closing levels are different along the crack front. In particular, the plane stress condition implies that surface points tend to open and close at stresses higher than those registered for the central points of the crack. Consequently, during unloading, the external points are the first to experience crack closing: in these conditions, measurements are disturbed by the stress fields generated by the contact occurring in those zones where plane strain condition is present. This feature is not present in the small scale specimens, since the crack front is smaller and it can be assumed that all the point lying on the crack front experience the same opening and closing levels.

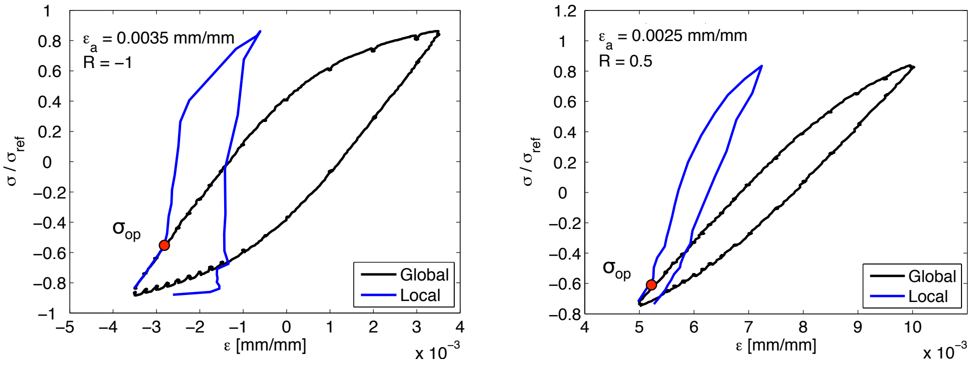

(a) (b)

Figure 5.14: *Crack closure measurements in LCF with DIC on large scale specimens. a) comparison between local and global hysteresis loops and opening and closing levels identification for tests conducted at R = -1; b) comparison between local and global hysteresis loops and opening and closing levels identification for tests conducted at R = 0.5.*

In order to evaluate the values of $\Delta\sigma_{eff}$, it was assumed that crack closing occurred at the same strain level registered at opening, following what was experimentally observed on the small scale specimens and Vormwald's hypotheses. Experimental results, expressed in terms of $\Delta\sigma_{eff}/\Delta\sigma$, are reported in Fig. 5.15, where, for both the loading conditions investigated, it can be observed that the measured values of $\Delta\sigma_{eff}$ are higher than those recorded during small scale testing. This is related to the fact that the constraint condition registered in the large scale specimen geometry is more severe than the one of the small scale specimen. In particular, it can be noted that the ratio between $\Delta\sigma_{eff}$ and $\Delta\sigma$ is very close to 1, meaning that the crack stays open for almost the entire fatigue cycle.

After the end of the tests, two specimens were broken in liquid nitrogen, to observe the final shape of the fatigue crack and to highlight the difference in propagation between the superficial and the deepest points of the crack. In Fig. 5.16a the crack observed after the fatigue test conducted at R = 0.5 on the sample with the 1.4 mm deep

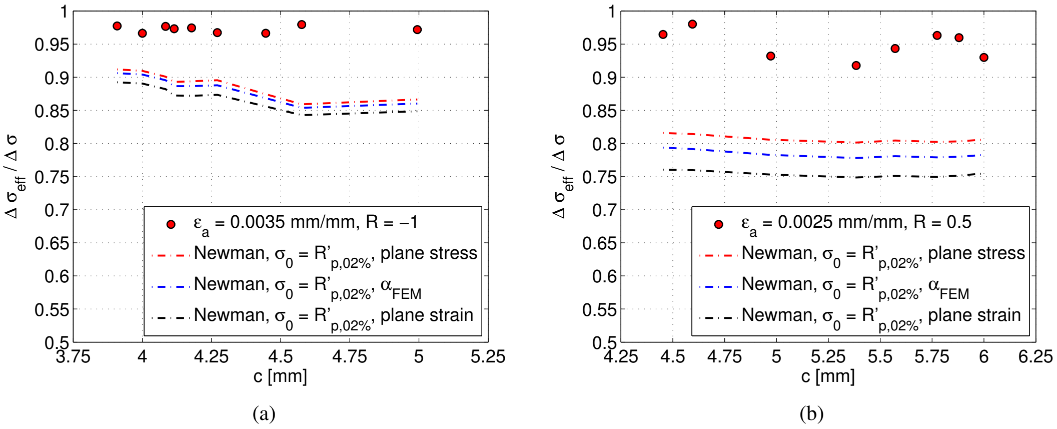

Figure 5.15: *Comparison between experimental and analytical effective stress amplitudes, large scale specimens. a) R = -1, ϵ_a = 0.0035 mm/mm; b) R = 0.5, ϵ_a = 0.0025 mm/mm.*

defect is reported. The experiment was interrupted when the surface crack length, $2c$, was equal to 13.14 mm. The final crack depth, measured after breaking the specimen in liquid nitrogen, was equal to 4.73 mm. The crack shape is completely different from the initial notch geometry. In particular, a *canoe shape* defect can be observed: this is due to the fact that, on the surface, crack propagation occurs at slower rates, since crack opening and closing levels are higher because of the plane stress condition acting in these regions. The same shape was observed even for the specimen tested at R = -1, presented in Fig. 5.16b: this test was stopped after a limited number cycles, in order to observe the aspect ratio in an intermediate condition, between the beginning and the end of the test. The specimen exhibits a 2.97 mm deep crack, whereas crack width is equal to 9.9 mm.

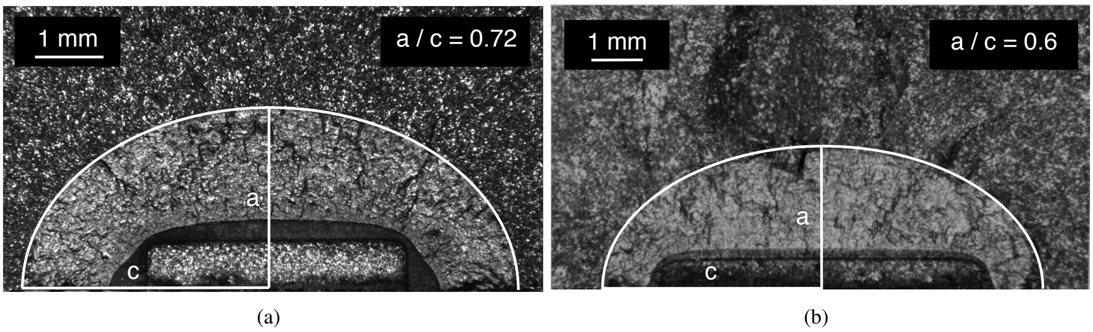

Figure 5.16: *Fracture surface of two large scale specimens after the end of the test. a) Initial defect depth 1.4 mm, R = 0.5; b) Initial defect depth 0.7 mm, R = -1.*

It is worth remarking that the aspect ratio of the defect is changing during the test, because of the different crack growth rates experienced at the different points along crack flanks. An intermediate aspect ratio, a/c, of 0.6 was calculated for the specimen stopped before the end of the test, whereas the crack of the specimen stopped at the target number of cycles exhibited an a/c equal to 0.73. The different crack growth rates along the crack front, together with the small number of specimens tested, made it impossible to obtain a relationship between a and c. This neglected the possibility to obtain a graph like the one proposed in Fig. 5.12.

5.4.3 Analysis of constraint

The observation of the crack shape after the experiments underlined the fact that the constraint factor, α, is changing along the crack front. In order to evaluate the loading condition present at the crack deepest point and to evaluate opening and closing levels according to Newman's analytical model, a FEM model was developed to calculate α. The FEM model employed for calculations is reported in Fig. 5.17: original crack profile (Fig. 5.16b) was approximated with an ellipse, as proposed in Fig. 5.17a. 8-nodes linear 3D elements were employed during the analysis: mesh was refined around the crack front, with a minimum element size of 50 μm. In order to reduce computational time, all the present symmetries were considered: this allowed to model only one quarter of the large scale specimen, as shown in Fig. 5.17b, in which boundary conditions are also depicted. Normal displacements were neglected on the symmetry planes, whereas the external force was applied on a reference point, connected to the model by a coupling costraint. Reference point, during the simulation, had all the degrees of freedom constrained, except of U_3, the axial direction.

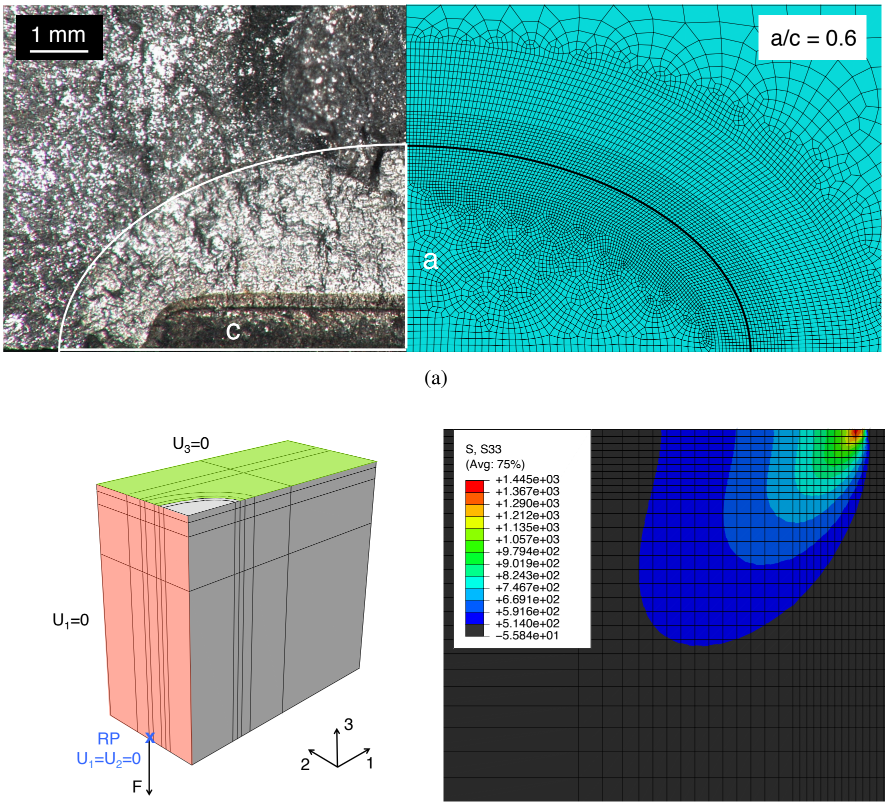

(a)

(b)

(c)

Figure 5.17: *Numerical analysis of the large scale specimen. a) Mesh refinement along the crack front; b) boundary conditions; c) Plastic zone around the crack front, crack deepest point.*

According to Newman [82], the constraint factor can be calculated as:

$$\alpha = \frac{\int_{A_0} \sigma_n dA_n}{\sigma_0 \cdot A_0} \tag{5.2}$$

where σ_n is the value of the stress in the n-th element of the plastic zone surrounding the tip, A_n is the area of the n-th element of the total plastic zone A_0 and σ_0 is the flow stress, calculated following Vormwald's proposal (Eq. 5.1). Numerically, the integral of Eq. 5.2 can be computed as:

$$\alpha = \frac{\int_{A_0} \sigma_n dA_n}{\sigma_0 \cdot A_0} \approx \frac{\sum_i \sigma_{ni} \cdot A_i}{A_0 \sigma_0} = 1.47 \tag{5.3}$$

where σ_n is the value of the stress calculated along the third direction and A_i is the area in which the total plastic zone was divided, in which the stress was supposed constant and equal to the nodal value. It was found that, for the given geometry, $\alpha = 1.47$.

At this point it was possible to calculate the analytical values of the effective stress ranges. In Fig. 5.15, analytical values are compared to those experimentally measured. In this case, only the formulation of the flow stress proposed by Savaidis was considered. In order to observe the influence of the constraint factor on the crack opening levels, three different values of α were considered. In particular, $\alpha = 1$ (plane stress) and $\alpha = 2.5$ (plane strain) were taken into account, together with the value of the constraint factor numerically calculated. The plane stress condition is the most demanding one, since it implies the highest value of $\Delta\sigma_{eff}$, whereas the plane strain condition is the one that exhibits the smallest values of the effective stress ranges. This behavior is not in line with the experimental results, since it was observed that the opening loads measured during small scale testing ($\alpha = 1$) were higher than those recorded during large scale tests: this means that the loading conditions considered in this study exceeds the limits of validity of the analytical model proposed by Newman.

It is also worth remarking that the effective stress ranges measured during the experiments were comparable to the total total stress range, since crack opening levels were close to the applied minimum stress. From an engineering point of view, this means that a crack propagation model based on total stress and strain amplitudes can be implemented and provide satisfactory results. These experimental observations, together with the da/dN-ΔJ_{eff} curve calculated in section 5.3, were employed in the following section to provide a tool capable of assessing fatigue lives of large scale specimens.

5.5 FATIGUE LIFE ASSESSMENT FOR LARGE SCALE SPECIMENS

Tests performed on small scale specimens provided the da/dN - ΔJ_{eff} curve necessary for fatigue life assessment, whereas the crack closure measurements performed on large scale specimens allowed an accurate estimation of the effective stress ranges experienced by the defect during propagation. This information, together with a correct formulation of ΔJ_{eff} range can be used to estimate the fatigue life of the large scale specimens.

This section is divided into two different parts. In the first, the analytical formulation of ΔJ is modified in order to take into account the geometry of large scale specimens. At this point, the formulation is checked with a numerical model, in order to validate the so-obtained equation. Finally, fatigue life of two specimens is assessed considering two different propagation models. A model based on the total ΔJ, interesting from an engineering point of view, is implemented and its estimates are compared to those proposed by the model which considers ΔJ_{eff}.

5.5.1 ΔJ formulation for large scale specimens

The general formulation of ΔJ can be espressed as:

$$\Delta J = \Delta J_{el} + \Delta J_{pl} = Y^2 \pi a \left(\frac{\Delta \sigma^2}{E'} + h\left(n_i\right) \Delta \sigma \Delta \epsilon_{pl} \right) \tag{5.4}$$

where Y is the geometric factor, $\Delta\sigma$ is the applied stress range, $h\left(n_i\right)$ is a function that takes into account the effects of plastic strain, $\Delta\epsilon_{pl}$ is the plastic strain and

$$E' = \begin{cases} E, & \text{plane stress} \\ E/\left(1-\nu^2\right), & \text{plane strain} \end{cases} \tag{5.5}$$

.

The concept of ΔJ was proposed by Dowling [26,31], who extended to fatigue the line integral originally introduced by Rice [27]. Cyclic J-Integral was implemented by replacing remote stress and strain with the remote stress and strain amplitudes cyclically applied to the cracked component. This feature, together with the fact that J is a line integral that can be computed only considering monotonic loadings, neglects the possibility to extract the value of ΔJ from numerical simulations. Because of this, in this work the values of Y and $h\left(n_i\right)$ were calculated by considering a numerical model of a large scale specimen monotonically loaded.

The FEM model reported in Fig. 5.17 was modified and employed for calculations: the geometric factor Y was calculated by considering material elastic behavior. For the given geometry, a value of 0.86 was obtained for the crack deepest point. This value differs less than 5% from the value provided by Newman-Raju equations [112].

Material elastic-plastic behavior was introduced, in order to evaluate an estimate of $h\left(n_i\right)$. Material inelastic behavior was modelled by adopting a power hardening law, as proposed in Eq. 5.6, where the Ramberg-Osgood equation is reported.

$$\epsilon = \epsilon_{el} + \epsilon_{pl} = \frac{\sigma}{E} + \left(\frac{\sigma}{k_i}\right)^{1/n_i} \tag{5.6}$$

During the simulation, the value of the applied force, F, was monotonically increased, in order to evaluate the trend of J. It was found that Eq. 5.4 best fits numerical results when the formulation of $h\left(n_i\right)$ proposed in Eq. 5.7 is adopted, as shown in Fig. 5.18. This equation, originally proposed in [113], was calculated considering plane strain conditions and it further confirms that the crack deepest point, during fatigue crack propagation, experiences a stress condition similar to plane strain.

$$h\left(n_i\right) = \frac{3}{4\sqrt{n_i}} \tag{5.7}$$

Following these observations, Eq. 5.4 was modified in order to take into account the geometry of the large scale specimen, as proposed in Eq. 5.8, where plane strain

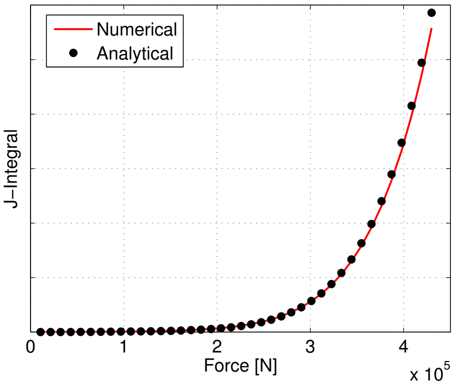

Figure 5.18: *Numerical analysis of the large scale specimen for J validation: comparison between numerical and analytical results, expressed in terms of J vs applied force.*

conditions are assumed.

$$\Delta J = a\left(2.12\frac{\Delta\sigma^2}{E} + \frac{1.75}{\sqrt{n_i}}\Delta\sigma\Delta\epsilon_{pl}\right) \tag{5.8}$$

5.5.2 Fatigue life estimates

In this section, fatigue life of two broken specimens is assessed. The estimate is obtained by calculating the number of cycles necessary for the crack deepest point to propagate from the initial depth, a_0, measured after precracking, to the final defect size, a_f, measured after breaking the samples in liquid nitrogen.

An iterative procedure was implemented, in order to take into account material initial transient behavior. This was necessary because the values of $\Delta\sigma$ and $\Delta\epsilon_{pl}$, during initial fatigue cycles, are very different from those recorded in the stabilized hysteresis loop. Moreover, this allowed the extraction of ΔJ directly from the stress/strain cycles, following original Dowling's proposal [26]. The steps considered in each iteration of the procedure are the following:

- calculation of the experimental stress and plastic strain amplitudes at the $i-th$ load cycle, together with the strain power exponent n_i;
- evaluation of the applied ΔJ_i;
- computation of the $i-th$ crack increment as:

$$da_i = c\,(\Delta J_i)^m \cdot d\hat{N}, \text{ with } d\hat{N} = 1 \tag{5.9}$$

  where c and m are the constants that describe the closure-free propagation curve of the small scale specimens, shown in Fig. 5.12b.
- crack length update:

$$a_i = a_{i-1} + da_i \tag{5.10}$$

Two different formulation of ΔJ were employed during calculations. Since the experimentally measured crack opening levels were very low, comparable to the minimum applied load, an initial model that considered ΔJ_{tot} was adopted. According to this formulation, the total part of the stress and plastic strain ranges are considered in ΔJ calculations. Fatigue life assessment obtained considering ΔJ_{tot} is represented in Fig. 5.19 by blue dashed lines. As expected, this formulation provides, for both the experiments, conservative results. This feature makes the model very interesting from an engineering viewpoint, since it provides consistent results with a relatively simple formulation, making it the preferrable choice for industrial applications.

As a further step in the analysis, the model based on ΔJ_{eff} was implemented. This model follows the formulation proposed by Vormwald [3], described in Chapter 2. In order to calculate the effective J-Integral range, $\Delta\sigma$ and $\Delta\epsilon_{pl}$ where replaced in Eq. 5.8 with the effective stress and plastic strain ranges, calculated as proposed in Table 5.1. Since it was not possible to evaluate crack closing levels, it was assumed that closing occurs at σ_{cl}, the stress level in which, during unloading, the strain at crack opening, ϵ_{op}, is reached, following what was experimentally observed on small scale specimens.

Table 5.1: *Stress and strain components for ΔJ_{tot} and ΔJ_{eff} formulations.*

ΔJ_{tot}	ΔJ_{eff}
$\Delta\sigma = \Delta\sigma_{tot}$ $\Delta\epsilon_{pl} = \epsilon_{max} - \epsilon_{min} - \frac{\Delta\sigma_{tot}}{E}$	$\Delta\sigma = \Delta\sigma_{eff} = \sigma_{max} - \sigma_{cl}$ $\Delta\epsilon_{pl} = \epsilon_{max} - \epsilon_{op} - \frac{\Delta\sigma_{eff}}{E}$

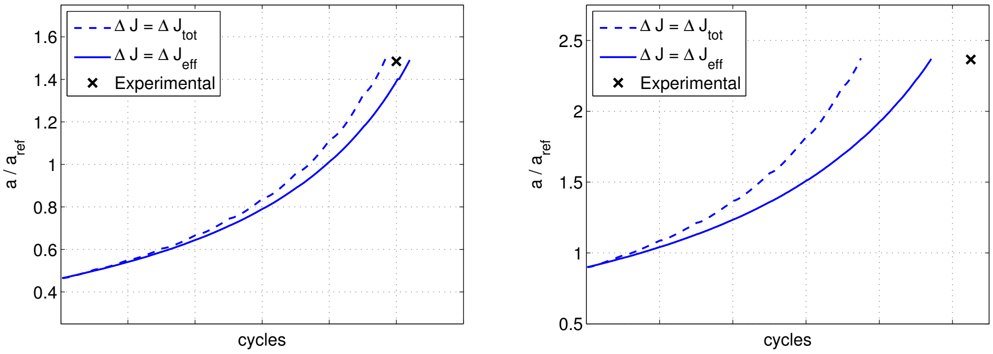

(a)

(b)

Figure 5.19: *Fatigue life assessment for the two broken specimens. The cross represents the experimental point, whereas the dashed and continuous lines are, respectively, the results of the simulations performed considering the models based on ΔJ_{tot} and ΔJ_{eff}. a) Test performed at R = -1; b) Test performed at R = 0.5.*

Fatigue life assessment, obtained consideringt ΔJ_{eff} is represented in Fig. 5.19 by a continuous blue line. As it can be seen, the model tends to be unconservative when the first sample is considered (Fig. 5.19a). This is due to the fact that, in our calculations, the opening and closing levels were kept constant during the propagation, whereas it has been proved [65] that even crack closure is a transient mechanism. In particular, it was observed that a crack, in the early propagation stage, stays open for the whole load cycle. This observation, together with the fact that the first test was interrupted after a very small number of cycles, explains the cause of the small error in fatigue life estimation. On the other hand, the fatigue life assessment for the second test, obtained considering ΔJ_{eff} and proposed in Fig. 5.19b, provides more accurate results, reduces the safety margin and probes that the opening levels measured with DIC are correct.

5.6 CONCLUSIONS

Fatigue crack growth under severe loading conditions was investigated for a linepipe steel. A preliminary experimental campaign was performed on specimens containing 400 μm deep semi-circular defects, in order to observe fatigue crack growth. Two different loading conditions were investigated. Specimens were initially tested with a fixed strain ratio, R, equal to -1, with an applied strain amplitude, ϵ_a, equal to 0.0035 mm/mm, to check the ΔJ_{eff}-based model presented in chapter 2. At this point the strain ratio was changed to 0.5 and ϵ_a to 0.0025 mm/mm, in order to check crack propagation with the selected straining conditions. Experimental results were analyzed in terms of crack growth rates and were compared to those obtained testing a C(T) specimen at high stress ratio (R = 0.7). It was observed that experimental crack growth rates were higher than those measured during long crack testing. Therefore, a new series of experiments was performed on the same specimen geometry, in order to check crack-closure. An innovative experimental technique, based on digital image correlation, was employed to measure crack opening levels. The technique consisted in applying a virtual strain gauge under the defect: crack opening and closing levels were evaluated as the points in which the stress/strain cycle measured by the virtual gauge differed from the remote one, measured by the extensometer which controlled the strain amplitude applied to the specimen.

DIC-based measurements showed that the analytical opening levels, calculated with the model proposed by Newman, were higher than those experimentally observed: this means that the value of ΔJ_{eff} calculated with the model underestimated the real crack propagation driving force. At this point, the propagation model was modified to take into account measured crack closure levels: experimental data points shifted on the da/dN - ΔJ_eff obtained from C(T) testing.

A different specimen geometry was then taken into account. Specimens with a 43 mm x 10 mm net section were tested with the same loading conditions applied on the small specimens, in order to check crack propagation in presence of greater defects. In this phase, 0.7 and 1.4 mm deep defects were considered. Crack opening levels were measured during propagation, with the same technique employed for the small specimens. Smaller crack opening levels were observed: this was related to the difference in the constraint factor between the two considered geometries.

Finally, the crack propagation model was employed to assess fatigue life of the large scale specimens: ΔJ equation was modified in order to take into account the geometry of the large scale specimens. A numerical model was employed to confirm the proposed formulation, showing that, for the large scale geometry, the plastic part of the J-integral can be modelled considering a plane strain condition.

CHAPTER 6

Concluding remarks

The primary objective of this Ph.D thesis was the study of short crack propagation in components for the energy industry, such as turbine disks, blades and pipelines. These components, during their in-service lifetime, are usually designed to withstand a limited number of load cycles. Gas turbines, for example, are vastly chosen to produce the energy necessary to meet the load peaks requested by users: this means that, during their lifetime, they are subjected to several start-ups and shut-downs, which correspond to several load cycles. Because of this, they are usually designed considering a target of 10000 cycles. The same observations can be made for pipelines: due to the high demand of oil resources, these products have to deal with very complex exploitation fields. In particular, these tubes are subjected to high pressures and to elevated changes in temperature, which imply that, during their in-service operations, they have to withstand a series of severe load cycles in presence of very high strains. It is evident that fatigue life design of these components should take into account the presence of high plastic strains, meaning that fatigue cracks, during cycling, propagate in plastic regions.

Because of this, the activity developed in this thesis was focused on the study of crack propagation in presence of plastic strains. Experimental campaigns were developed in order to observe crack propagation in specimens that simulated the stress/strain conditions present in the most critical parts of the components, such as the blade attachments of turbine disks. Experimental results were compared to those provided by analytical models which considered short crack propagation in the LCF regime.

In Chapter 2, an experimental campaign was developed to check the effects of high temperature on short crack propagation. Experimental results were analyzed by applying a model based on ΔJ_{eff}. The analytical formulation of ΔJ was modified, following Dowling's original proposal, in order to evaluate the cyclic J-Integral directly from the hysteresis loops. This new formulation allowed the extraction of ΔJ even for those materials that do not exhibit Masing's behavior and for those loading conditions that imply the presence of a mean stress. It was found that models based on ΔJ cannot be applied on short crack propagation above a given temperature, since there are damage mechanisms present at the crack tip. Therefore, it was necessary to include an acceleration factor in the calculations, in order to provide conservative assessments.

In Chapter 3, the necessity to accurately describe material cyclic response was highlighted by the analysis of short crack propagation in presence of a plastic strain gradient. This activity was performed in order to observe short crack propagation in loading conditions similar to those experienced by turbine disks. A numerical analysis, which considered material elastic-plastic behavior, was performed in order to check the stress field present at the root of blade attachments, the most critical parts of the disk. It was found that the particular in-service conditions induced, in this part of the disk, an elastic shakedown response. This condition was also observed during the experiments and implied that a formulation based only on the stress intensity factor ranges could be adopted, since the plastic term of ΔJ_{eff} equation was nearly zero, being the fatigue cycle fully elastic ($\Delta K = \sqrt{\Delta J \cdot E}$). It was found that the propagation model was able to describe crack propagation only when the load cycle registered at the root of the notch was fully reversed. The reasons of the wrong estimates, obtained when a mean stress was present, were related to the analytical model adopted to measure crack opening levels: the model proposed by Newman, usually employed in these calculations, is not suitable for loading conditions with an applied mean load.

Because of this, an innovative experimental technique, based on digital image correlation, was developed to measure crack opening loads. In Chapter 4, this technique was adopted to measure crack opening and sliding levels during Mixed Mode (I+II) propagation in single crystals. The material used for testing was a Ni-based superalloy, Haynes 230. Moreover, a regression algorithm was applied in order to extract crack propagation driving forces from the displacement field measured around crack tips. The measured stress intensity factor ranges were employed to evaluate the cyclic plastic strain zones present around the tip. In order to validate the presented technique, a numerical model, which considered single crystal plasticity was developed. Numerically calculated plastic zones were compared to those experimentally extracted, showing good agreement in terms of shape and extension.

The technique presented in Chapter 4 was applied to LCF in Chapter 5. In this chapter, an experimental activity was performed to check crack propagation under severe loading conditions, like those experienced by pipelines for undersea applications. Experimental results, depicted in Fig.6.1, showed that crack opening levels were completely different from those calculated considering Newman's analytical model. At this point, measured crack opening levels were implemented in the crack propagation model based on ΔJ_{eff}. It was found that, in order to obtain conservative assessments, material cyclic response had to be accurately modeled, underlining, another time, the necessity to include material transient behavior in calculations.

The work presented in this thesis can be further developed in two different lines. First of all, new analytical models and computational methods for opening levels evaluation should be developed, since it is evident that the model proposed by Newman is not suitable for LCF at $R \neq 0$, because it does not take into account effects such

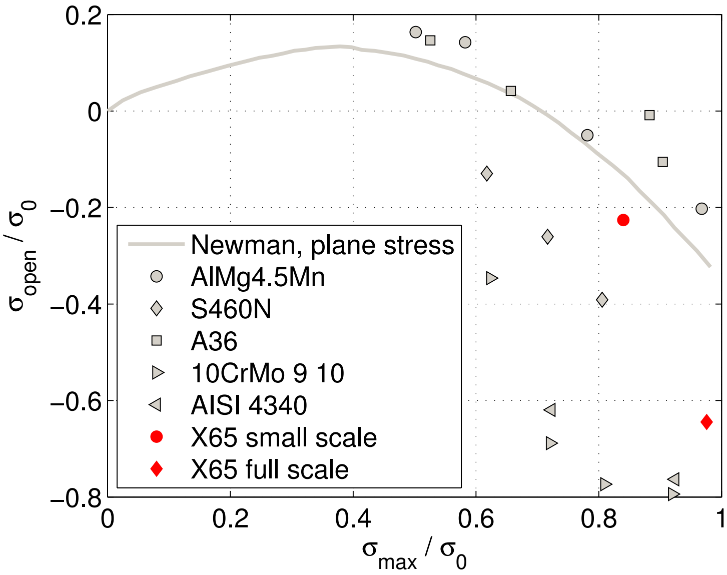

Figure 6.1: *Comparison between crack opening levels calculated according to Newman and experimental measurements at R = -1. Grey points represent results presented in [3], whereas red points are those experimentally measured in this work.*

as ratchetting and it is able to predict closure levels only when fully reversed loading is considered. Numerical techniques, such as those presented in [114, 115], can be considered.

Finally, another possible development is the study of short crack propagation in Haynes 230 polycrystals, following the techniques discussed in Chapter 2. Being Haynes 230 an alloy designed for high temperature applications, it is expected that, during short crack propagation tests at high temperature, the alloy does not exhibit the damage mechanisms highlighted in chapter 2 during propagation in quenched and tempered steels. This could open to more precise prediction models of Ni-based superalloys in turbine disks and blades, because higher operating temperatures are needed for new power generation turbines.

The crack closure measurements, performed on single crystals, can also be employed to develop predictive models for components that present a single crystal structure, such as turbine blades. They can also be used as a starting point for the implementation of models that predict closure levels in polycrystals, considering grain interaction.

Publications

Papers in international journals

- S. Foletti, S. Beretta, F. Scaccabarozzi, S. Rabbolini, and L. Traversone. FATIGUE CRACK GROWTH IN BLADE ATTACHMENT OF TURBINE DISKS: EXPERIMENTAL TESTS AND LIFE PREDICTION, to appear in *Material Performance and Characterization*;
- S. Rabbolini, G.J. Pataky, H. Sehitoglu and S. Beretta. FATIGUE CRACK GROWTH IN HAYNES 230 SINGLE CRYSTALS: AN ANALYSIS WITH DIGITAL IMAGE CORRELATION, to appear in *Fatigue & Fracture of Engineering Materials & Structures*;
- S. Rabbolini, S. Beretta, S. Foletti and A. Riva. SHORT CRACK PROPAGATION IN LCF REGIME AT ROOM AND HIGH TEMPERATURE IN Q & T ROTOR STEELS, to appear in *International Journal of Fatigue*;
- S. Rabbolini, S. Beretta, S. Foletti and M.E. Cristea. CRACK CLOSURE EFFECTS IN LINE PIPE STEEL: AN ANALYSIS WITH DIGITAL CORRELATION, submitted to *Engineering Fracture Mechanics*;

Conference papers

- S. Beretta, S. Foletti, S. Rabbolini, L.E. Bordo, A. Sanguineti, and L. Traversone. MODELS FOR SMALL CRACK GROWTH IN LCF AT ROOM TEMPERATURE AND HIGH TEMPERATURE. ASME Turbo Expo 2012;
- S. Rabbolini, G.J. Pataky, H. Sehitoglu and S. Beretta. ANISOTROPIC STRESS INTENSITY FACTOR RANGES MEASUREMENTS WITH DIC. 20^{th} European Conference on Fracture.
- S. Foletti, S. Beretta, F. Bassi, S. Rabbolini and M.E. Cristea. CRACK GROWTH MODEL BASED ON ΔJ APPROACH OF PIPES UNDER SEVERE DEFORMATIONS CYCLING. 20^{th} European Conference on Fracture.

Bibliography

[1] J. Schijve. Four lectures on fatigue crack growth. *Engineering Fracture Mechanics*, 11(1):167–168, 1979.

[2] J. Carroll, C. Efstathiou, J. Lambros, H. Sehitoglu, B. Hauber, S. Spottswood, and R. Chona. Investigation of fatigue crack closure using multiscale image correlation experiments. *Engineering Fracture Mechanics*, 76(15):2384–2398, 2009.

[3] M. Vormwald and T. Seeger. The consequences of short crack closure on fatigue crack growth under variable amplitude loading. *Fatigue and Fracture of Engineering Materials and Structures*, 14(2/3):205–25, 1991.

[4] R.C. McClung and H. Sehitoglu. Characterization of fatigue crack growth in intermediate and large scale yielding. *Journal of Engineering Materials and Technology*, 113:15–22, 1991.

[5] J.C. Newman. A crack-closure model for predicting fatigue crack growth under aircraft spectrum loading. In JB Chang and CM Hudson, editors, *Methods and models for predicting fatigue crack growth under random loading*, pages 53–84. ASTM, 1981.

[6] C.C. Osgood. Damage-tolerant design(safe-life and fail-safe structural design philosophies in fatigue damage and operating lifetime control). *Machine Design*, 41:91–95, 1969.

[7] R.C. Combes J.R. Design for damage tolerance. *Journal of Aircraft*, 7(1):18–20, 1970.

[8] P. Paris and F. Erdogan. A critical analysus of crack propagation laws. *Basic Engng Trans ASME Series D*, 85:528–34, 1963.

[9] A.J. McEvily Jr and R.G. Boettner. On fatigue crack propagation in fcc metals. *Acta Metallurgica*, 11(7):725–743, 1963.

[10] W. Elber. Fatigue crack closure under cyclic tension. *Engineering Fracture Mechanics*, 2(1):37–44, 1970.

[11] A.J. McEvily. On crack closure in fatigue crack growth. *Mechanics of Fatigue Crack Closure*, 982:35–43, 1988.

[12] J.C. Newman and W. Elber. *Mechanics of fatigue crack closure*, volume 982. ASTM International, 1988.

[13] J.D. Dougherty, J. Padovan, and T.S. Srivatsan. Fatigue crack propagation and closure behavior of modified 1070 steel: finite element study. *Engineering Fracture Mechanics*, 56(2):189–212, 1997.

[14] H. Tsukuda, H. Ogiyama, and T. Shiraishi. Fatigue crack growth and closure at high stress ratios. *Fatigue & Fracture of Engineering Materials & Structures*, 18(4):503–514, 1995.

[15] ASTM. Astm e647 standard test method for measurement of fatigue crack growth rates. Technical report, ASTM international, 2013.

[16] D.H. Chen and H. Nisitani. Analytical and experimental study of crack closure behavior based on a s-shaped unloading curve. *Mechanics of Fatigue Crack Closure*, 982:475–488, 1988.

[17] M Toyosada and T Niwa. The significance of rpg load for fatigue crack propagation and the development of a compliance measuring system. *International journal of fracture*, 67(3):217–230, 1994.

[18] F.C. Tong and T.G.F Gray. Fatigue crack closure study based on whole-field displacements. *International journal of fatigue*, 18(8):593–601, 1996.

[19] F.A. Diaz, E.A. Patterson, R.A. Tomlinson, and J.R. Yates. Measuring stress intensity factors during fatigue crack growth using thermoelasticity. *Fatigue & Fracture of Engineering Materials & Structures*, 27(7):571–583, 2004.

[20] S.I. Rokhlin and J-Y Kim. In situ ultrasonic monitoring of surface fatigue crack initiation and growth from surface cavity. *International journal of fatigue*, 25(1):41–49, 2003.

[21] J. Schijve. Some formulas for the crack opening stress level. *Engineering Fracture Mechanics*, 14(3):461–465, 1981.

[22] G. Savaidis, M. Dankert, and T. Seeger. An analytical procedure for predicting opening loads of cracks at notches. *Fatigue & Fracture of Engineering Materials & Structures*, 18(4):425–442, 1995.

[23] R.G. Forman and S.R. Mettu. Behavior of surface and corner cracks subjected to tensile and bending loads in ti-6al-4v alloy. Technical report, NASA, Sep 1990.

[24] U. Zerbst, R. Lundén, K-O Edel, and R.A. Smith. Introduction to the damage tolerance behaviour of railway rails–a review. *Engineering fracture mechanics*, 76(17):2563–2601, 2009.

[25] K.J. Miller. Materials science perspective of metal fatigue resistance. *Materials science and technology*, 9(6):453–462, 1993.

[26] N.E. Dowling. *Cyclic Stress-Strain and Plastic Deformation Aspects of Fatigue Crack Growth*. ASTM, 1977.

[27] J.R. Rice. A path independent integral and the approximate analysis of strain concentration by notches and cracks. *Journal of applied mechanics*, 35(2):379–386, 1968.

[28] N.E. Dowling and J.A. Begley. Fatigue crack growth during gross plasticity and the j-integral. In *Mechanics of crack growth*, pages 82–103. ASTM, 1976.

[29] C.F. Shih. estimates for strain hardening materials in antiplane shear using fully plastic solutions. mechanics of crack growth. *ASTM STP*, 590:3–26, 1976.

[30] CF Shih and J.W. Hutchinson. Fully plastic solutions and large scale yielding estimates for plane stress crack problems. *Journal of Engineering Materials and Technology*, 98:289–95, 1976.

[31] N.E. Dowling. J-integral estimates for cracks in infinite bodies. *Engineering fracture mechanics*, 26(3):333–348, 1987.

[32] P. Zezulka and J. Polak. Short crack growth and fatigue life in austenitic-ferritic duplex stainless steel. *Fatigue and Fracture of Engineering Materials and Structures*, 28(10):923–35, 2005.

[33] G. Härkegård, J. Denk, and K. Stärk. Growth of naturally initiated fatigue cracks in ferritic gas turbine rotor steels. *International Journal of Fatigue*, 27(6):715–726, 2005.

[34] R.C. McClung and H. Sehitoglu. Closure behavior of small cracks under high strain fatigue histories. In J.C. Newman and W. Elber, editors, *Mechanics of FATIGUE CRACK CLOSURE*, chapter 2, pages 279–99. ASTM, 1988.

[35] D. Radaj and M. Vormwald. Elastic-plastic fatigue crack growth. In *Advanced Methods of Fatigue Assessment*, pages 391–481. Springer, 2013.

[36] U. Zerbst, M. Madia, and D. Hellmann. An analytical fracture mechanics model for estimation of s-n curves of metallic alloys containing large second phase particles. *Engineering Fracture Mechanics*, 82:115–134, 2012.

[37] U. Zerbst, M. Madia, J. Eufinger, and T. Bruder. Bruchmechanisches modell zur ermittlung der schwingfestigkeit von geschweißten und nichtgeschweißten proben. *Materials Testing*, 55(7-8):511–519, 2014/08/08 2013.

[38] *R6. Assessment of the Integrity of Structures Containing Defects*. British Energy Generation Ltd., 2000.

[39] U. Zerbst, M. Schodel, S. Webster, and R.A. Ainsworth. *Fitnet-for-Service fracture assessment of structures containing cracks. A workbook based on the European SINTAP/FITNET procedure*. Elsevier Science, 2007.

[40] J. Eufinger, A. Heinrietz, T. Bruder, and H. Hanselka. An engineering approach to fatigue analysis based on elastic-plastic fracture mechanics. *Fatigue and Fracture of Engineering Materials and Structures*, 36(1):65–74, 2013.

[41] B Tomkins. Fatigue crack propagation - an analysis. *Philosophical Magazine*, 18(155):1041, 1066 1968.

[42] J. Polak. Plastic strain-controlled short crack growth and fatigue life. *International Journal of Fatigue*, 27:1192–1201, 2005.

[43] J. Polak, T. Kruml, K.Obrtlik, J. Man, and M. Petrenec. Short crack growth in polycrystalline materials. *Procedia Engineering*, 2:883–92, 2010.

[44] R.P. Skelton. The prediction of crack growth rates from total endurances in high strain fatigue - thirty years on. *Fatigue and Fracture of Engineering Materials and Structures*, 32(2):81–83, 2008.

[45] *Assessment procedure R5.* British Energy Generation Ltd., 2003.

[46] S. Beretta, S. Foletti, S. Rabbolini, L.E. Bordo, A. Sanguineti, and L. Traversone. Models for small crack growth in lcf at room temperature and high temperature. In *ASME Turbo Expo 2012: Turbine Technical Conference and Exposition*, pages 323–330. American Society of Mechanical Engineers, 2012.

[47] W.H. Peters and W.F. Ranson. Digital imaging techniques in experimental stress analysis. *Optical Engineering*, 21(3):213427–213427, 1982.

[48] M.A. Sutton, W.J. Wolters, W.H. Peters, W.F. Ranson, and S.R. McNeill. Determination of displacements using an improved digital correlation method. *Image and vision computing*, 1(3):133–139, 1983.

[49] W.H. Peters, W.F. Ranson, M.A. Sutton, T.C. Chu, and J. Anderson. Application of digital correlation methods to rigid body mechanics. *Optical Engineering*, 22(6):226738–226738, 1983.

[50] T.C. Chu, W.F. Ranson, and M.A. Sutton. Applications of digital-image-correlation techniques to experimental mechanics. *Experimental mechanics*, 25(3):232–244, 1985.

[51] M.A. Sutton, C. Mingqi, W.H. Peters, Y.J. Chao, and S.R. McNeill. Application of an optimized digital correlation method to planar deformation analysis. *Image and Vision Computing*, 4(3):143–150, 1986.

[52] H.A. Bruck, S.R. McNeill, M.A. Sutton, and W.H. Peters Iii. Digital image correlation using newton-raphson method of partial differential correction. *Experimental Mechanics*, 29(3):261–267, 1989.

[53] W.T. Riddell, R.S. Piascik, M.A. Sutton, W. Zhao, S.R. McNeill, and J.D. Helm. Determining fatigue crack opening loads from near-crack tip displacement measurements. *ASTM SPECIAL TECHNICAL PUBLICATION*, 1343:157–174, 1999.

[54] M.A. Sutton, W. Zhao, S.R. McNeill, J.D. Helm, R.S. Piascik, and W.T. Riddell. Local crack closure measurements: Development of a measurement system using computer vision and a far-field microscope. *ASTM Special Technical Publication*, 1343:145–156, 1999.

[55] W. Elber. The significance of fatigue crack closure. In *Damage Tolerance in Aircraft Structures: A Symposium Presented at the Seventy-third Annual Meeting American Society for Testing and Materials, Toronto, Ontario, Canada, 21-26 June 1970*, volume 486, page 230. ASTM International, 1971.

[56] M.D. Sangid, G.J. Pataky, H. Sehitoglu, R.F. Hamilton, and H.J Maier. High resolution analysis of opening and sliding in fatigue crack growth. *International Journal of Fatigue*, 37:134–145, 2012.

[57] S.R. McNeill, W.H. Peters, and M.A. Sutton. Estimation of stress intensity factor by digital image correlation. *Engineering fracture mechanics*, 28(1):101–112, 1987.

[58] M.L. Williams. On stress distribution at base of stationary crack. *Journal of Applied Mechanics*, 24(1):109, 1957.

[59] S. Yoneyama, Y. Morimoto, and M. Takashi. Automatic evaluation of mixed-mode stress intensity factors utilizing digital image correlation. *Strain*, 42(1):21–29, 2006.

[60] G.J. Pataky, H. Sehitoglu, and H.J. Maier. High temperature fatigue crack growth of haynes 230. *Materials Characterization*, 75:69–78, 2013.

[61] P.C. Paris and G.C. Sih. Stress analysis of cracks. In *Fracture toughness testing and its applications*, pages 30–83. ASTM, 1965.

[62] N.E. Dowling. Crack growth during low-cycle fatigue of smooth axial specimens. *Astm Stp*, 637:97–121, 1977.

[63] Ch Wüthrich. The extension of the j-integral concept to fatigue cracks. *International Journal of Fracture*, 20(2):R35–R37, 1982.

[64] M. Vormwald. *Crack initiation life prediction based on fracture mechanics for short cracks*. PhD thesis, Technical University Darmstadt, 1989.

[65] AJ McEvily, M. Endo, and Y. Murakami. On the $\sqrt{\text{area}}$ relationship and the short fatigue crack threshold. *Fatigue and Fracture of Engineering Materials and Structures*, 26:269–78, 2003.

[66] J.C. Earthman. Characterization of small crack growth in 12% CrMoV steel under high temperature, low cycle fatigue conditions. *Materials Science and Engineering*, A132:89–95, 1991.

[67] D. Rojas Jara. *9-12% Cr heat resistant steels: alloy design, TEM characterisation of microstructure evolution and creep response at 650°C*. PhD thesis, Ruhr-Universitat Bochum, 2011.

[68] J.H Lee, B.J Kim, M.K. Kim, and B-S Lim. Effects of temperature and oxidation on threshold stress intensity factor of 12% Cr steel for steam turbine rotor component. *Journal of Mechanical Science and Technology*, 27(5):1273–1277, 2013.

[69] E. Voce. A practical strain-hardening function. *Acta Metallurgica*, 51:219—226, 1948.

[70] J-L Chaboche. Constitutive equations for cyclic plasticity and cyclic viscoplasticity. *International Journal of Plasticity*, 5(3):247–302, 1989.

[71] J.A. König. *Shakedown of elastic-plastic structures*. Elsevier, 2012.

[72] G.A. Georgiou. Probability of detection (pod) curves: derivation, applications and limitations. *Jacobi Consulting Limited Health and Safety Executive Research Report*, 454, 2006.

[73] G. Savaidis, A. Savaidis, G. Tsamasphyros, and Ch. Zhang. On size and technological effects in fatigue analysis and prediction of engineering materials and components. *International journal of mechanical sciences*, 44(3):521–543, 2002.

[74] C. Santus and D. Taylor. Physically short crack propagation in metals during high cycle fatigue. *International Journal of Fatigue*, 31(8):1356–1365, 2009.

[75] X.Q. Feng and D. Gross. A global/local shakedown analysis method of elasto-plastic cracked structures. *Engineering fracture mechanics*, 63(2):179–192, 1999.

[76] X. Wang and S.B. Lambert. Semi-elliptical surface cracks in finite-thickness plates with built-in ends. ii. weight function solutions. *Engineering Fracture Mechanics*, 68(16):1743–1754, 2001.

[77] X. Huang and T. Moan. Improved modeling of the effect of< i> r</i>-ratio on crack growth rate. *International Journal of Fatigue*, 29(4):591–602, 2007.

[78] R.C. McClung. Finite element analysis of specimen geometry effects on fatigue crack closure. *Fatigue & fracture of engineering materials & structures*, 17(8):861–872, 1994.

[79] J.C. Newman. A crack opening stress equation for fatigue crack growth. *International Journal of Fracture*, 24(4):R131–R135, 1984.

[80] S. Beretta, M. Carboni, and M. Madia. Modelling of fatigue thresholds for small cracks in a mild steel by "strip-yield" model. *Engineering Fracture Mechanics*, 76(10):1548–1561, 2009.

[81] J.Z. Liu and X.R. Wu. Study on fatigue crack closure behavior for various cracked geometries. *Engineering fracture mechanics*, 57(5):475–491, 1997.

[82] J.C. Newman Jr, C.A. Bigelow, and K.N. Shivakumar. Three-dimensional elastic-plastic finite-element analyses of constraint variations in cracked bodies. *Engineering Fracture Mechanics*, 46(1):1–13, 1993.

[83] J.C. Newman Jr and J.J. Ruschau. The stress-level effect on fatigue-crack growth under constant-amplitude loading. *International Journal of Fatigue*, 29(9):1608–1615, 2007.

[84] G. Härkegärd and A. Wormsen. Non-linear analysis of shallow cracks in smooth and notched plates part 1: Analytical evaluation. *The Journal of Strain Analysis for Engineering Design*, 40(3):237–244, 2005.

[85] G. Härkegärd and A. Wormsen. Non-linear analysis of shallow cracks in smooth and notched plates part 2: finite element validation. *The Journal of Strain Analysis for Engineering Design*, 40(3):245–254, 2005.

[86] AJ McEvily and RC Boettner. On fatigue crack propagation in fcc metals. *Acta Metallurgica*, 11:725–43, 1963.

[87] C. Laird. The influence of metallurgical structure on the mechanisms of fatigue crack propagation. *PAPER FROM FATIGUE CRACK PROPAGATION, ASTM STP NO 415. 1967, 131-180*, 1967.

[88] G.J. Pataky, M.D. Sangid, H. Sehitoglu, R.F. Hamilton, H.J. Maier, and P. Sofronis. Full field measurements of anisotropic stress intensity factor ranges in fatigue. *Engineering Fracture Mechanics*, 94:13–28, 2012.

[89] G.C. Sih, P.C. Paris, and G.R. Irwin. On cracks in rectilinearly anisotropic bodies. *International Journal of Fracture Mechanics*, 1(3):189–203, 1965.

[90] P.D. Shah, C.L. Tan, and X. Wang. T-stress solutions for two-dimensional crack problems in anisotropic elasticity using the boundary element method. *Fatigue & fracture of engineering materials & structures*, 29(5):343–356, 2006.

[91] R.W. Hertzberg. *Deformation and fracture mechanics of engineering materials*, volume 89. Wiley, 1996.

[92] K. Tanaka. Fatigue crack propagation from a crack inclined to the cyclic tensile axis. *Engineering Fracture Mechanics*, 6(3):493–507, 1974.

[93] Q. Chen, N. Kawagoishi, and H. Nisitani. Evaluation of fatigue crack growth rate and life prediction of inconel 718 at room and elevated temperatures. *Materials Science and Engineering: A*, 277(1):250–257, 2000.

[94] Y.L. Lu, P.K. Liaw, G.Y. Wang, M.L. Benson, S.A. Thompson, J.W. Blust, P.F. Browning, A.K. Bhattacharya, J.M. Aurrecoechea, and D.L. Klarstrom. Fracture modes of haynes< sup>®</sup> 230< sup>®</sup> alloy during fatigue-crack-growth at room and elevated temperatures. *Materials Science and Engineering: A*, 397(1):122–131, 2005.

[95] R. Hill. *The Mathematical Theory of Plasticity, The Oxford Engineering Science Series*. Oxford, 1950.

[96] J. Ricel. The mechanics of crack tip deformation and extension by fatigue. *fatigue crack propagation, ASTM, ASTM STP*, page 415, 1966.

[97] K. Gall, H. Sehitoglu, and Y. Kadioglu. Plastic zones and fatigue-crack closure under plane-strain double slip. *Metallurgical and materials transactions A*, 27(11):3491–3502, 1996.

[98] G.I. Taylor. Plastic strain in metals. *J Inst Metals*, (62):307, 1938.

[99] R. Hill. Generalized constitutive relations for incremental deformation of metal crystals by multislip. *Journal of the Mechanics and Physics of Solids*, 14(2):95–102, 1966.

[100] J.R. Rice. Inelastic constitutive relations for solids: an internal-variable theory and its application to metal plasticity. *Journal of the Mechanics and Physics of Solids*, 19(6):433–455, 1971.

[101] R. Hill and J.R. Rice. Constitutive analysis of elastic-plastic crystals at arbitrary strain. *Journal of the Mechanics and Physics of Solids*, 20(6):401–413, 1972.

[102] A. Needleman, R.J. Asaro, J. Lemonds, and D. Peirce. Finite element analysis of crystalline solids. *Computer methods in applied mechanics and engineering*, 52(1):689–708, 1985.

[103] E.H. Lee. Elastic-plastic deformation at finite strains. *Journal of Applied Mechanics*, 36(1):1–6, 1969.

[104] Y. Huang. *A User-material Subroutine Incroporating Single Crystal Plasticity in the ABAQUS Finite Element Program*. Harvard Univ., 1991.

[105] A. Izquierdo, H. Quintanilla, G. Richard, E. Garcia, M. Armengol, P. Novelli, L. Di Vito, G. Porcu, G. Mannucci, E. Anelli, et al. Development of line pipe for high pressure/high temperature and sour service applications. *Proc. of Offshore and Arctic Engineering, OMAE2009-79153*, 2009.

[106] L. Di Vito, G. Mannucci, G. Mortali, M. Armengol, P. Novelli, A. Izquierdo, G. Richard, and H. Quintanilla. Ultra heavy wall linepipe x65: Material performances for severe applications. In *ASME 2009 28th International Conference on Ocean, Offshore and Arctic Engineering*, pages 145–158. American Society of Mechanical Engineers, 2009.

[107] L Di Vito, J Ferino, G Mannucci, A Lucci, L Vitali, F Marchesani, M Armengol, P Novelli, F Tintori, P Darcis, et al. Ultra heavy wall linepipe x65: Ratcheting in severe cyclic straining. In *ASME 2010 29th International Conference on Ocean, Offshore and Arctic Engineering*, pages 899–910. American Society of Mechanical Engineers, 2010.

[108] M.E. Cristea, S. Beretta, and A. Altamura. Fatigue limit assessment on seamless tubes in presence of inhomogeneities: Small crack model vs. full scale testing experiments. *International Journal of Fatigue*, 41:150–157, 2012.

[109] J. Newman Jr, J. Schneider, A. Daniel, and D. McKnight. Compression precracking to generate near threshold fatigue-crack-growth rates in two aluminum alloys. *International journal of fatigue*, 27(10):1432–1440, 2005.

[110] A.L. Gurson. Continuum theory of ductile rupture by void nucleation and growth: Part i—yield criteria and flow rules for porous ductile media. *Journal of engineering materials and technology*, 99(1):2–15, 1977.

[111] A. Needleman and V. Tvergaard. An analysis of ductile rupture modes at a crack tip. *Journal of the Mechanics and Physics of Solids*, 35(2):151–183, 1987.

[112] J.C. Newman Jr and I.S. Raju. An empirical stress-intensity factor equation for the surface crack. *Engineering Fracture Mechanics*, 15(1):185–192, 1981.

[113] M.Y. He and J.W. Hutchinson. The penny-shaped crack and the plane strain crack in an infinite body of power-law material. *Journal of Applied Mechanics*, 48(4):830–840, 1981.

[114] R.C. McClung and H. Sehitoglu. Closure and growth of fatigue cracks at notches. *Journal of Engineering Materials and Technology*, 114(1):1–7, 1992.

[115] G.P. Potirniche, S.R. Daniewicz, and J.C. Newman. Simulating small crack growth behaviour using crystal plasticity theory and finite element analysis. *Fatigue & Fracture of Engineering Materials & Structures*, 27(1):59–71, 2004.

[116] V. Tvergaard. Influence of voids on shear band instabilities under plane strain conditions. *International Journal of Fracture*, 17(4):389–407, 1981.

[117] V. Tvergaard. On localization in ductile materials containing spherical voids. *International Journal of Fracture*, 18(4):237–252, 1982.

[118] G. Bernauer and W. Brocks. Micro-mechanical modelling of ductile damage and tearing–results of a european numerical round robin. *Fatigue & Fracture of Engineering Materials & Structures*, 25(4):363–384, 2002.

Appendices

APPENDIX *A*

Analysis of damage with the GTN model

In order to provide a possible explanation of the higher crack growth rates registered during fatigue tests performed on the line pipe steel, fracture surface was investigated. The surface analysis, reported in Fig.5.6, underlined the fact that a damaged area is present ahead of the tip. In particular, it can be observed that the damaged area extends from the horizontal precrack and has a triangular shape. This damage mechanism can be related to the very high plastic strains present around crack tip: in particular, it was supposed that the strain field acting at the tip during the first load can initiate a process of nucleation, growth and coalescence of small voids. Because of this, a numerical analysis based on the Gurson, Tvergaard and Needleman (GTN) model was implemented. In the following sections a brief overview of the constitutive model is provided, together with the results obtained from FEM models of the cracked specimens.

A.1 The GTN model for void nucleation, growth and coalescence simulation

The initial formulation of the GTN model is due to Gurson [110], who developed a constitutive model for porous ductile media based on a rigid-plastic material behavior and the upper bound theorem of plasticity. Tveergard [116, 117], after detailed phenomenological studies of the bifurcation behavior of materials containing periodical distributions of voids, refined the constitutive Gurson's model by modifying its original yield function, including three additional parameters (q_1, q_2 and q_3):

$$\Phi = \frac{\sigma_M^2}{\sigma_y^2} + 2q_1 f^* cosh\left(q_2 \frac{3\sigma_h}{2\sigma_y}\right) - \left(1 + q_3 f^{*2}\right) = 0 \tag{A.1}$$

where σ_M is the von Mises stress of the deviatoric part of the macroscopic stress tensor, σ_{ij}, σ_h is the macroscopic hydrostatic stress, σ_y is the current flow stress of the fully dense material matrix and f^* is the effective void volume fraction.

The plastic strains are derived from Eq. A.1; the presence of the first invariant of the stress tensor in the yield condition results in non-deviatoric plastic strains:

$$\dot{\epsilon}_{ij}^{pl} = \dot{\lambda}\frac{\partial \Phi}{\partial \sigma_{ij}} = \dot{\lambda}\left(\frac{1}{3}\frac{\partial \Phi}{\partial \sigma_h} I + \frac{3}{2\sigma_M}\frac{\partial \Phi}{\partial \sigma_M S}\right) \tag{A.2}$$

where I is the identity matrix, S is the deviatoric part of σ_{ij} and $\dot{\lambda}$ is the non-negative plastic flow multiplier.

The matrix flow stress, σ_y, is calculated by imposing equality between the rates of macroscopic and matrix plastic work:

$$\sigma_{ij}\dot{\epsilon}_{ij}^{pl} = (1 - f^*)\,\sigma_y \dot{\bar{\epsilon}}^{pl} \tag{A.3}$$

where $\dot{\bar{\epsilon}}^{pl}$ is the average effective plastic strain rate of the material. It can be noted that this formulation gives the same results of the von Mises one, in the limiting case of zero porosity ($f^* \to 0$) and that, on the other hand, $f^* = 1$ implies that the material is fully voided and has no stress carrying capacity. In his work, Tvergaard [116, 117] originally suggested the values of $q_1 = 1.5$, $q_2 = 1$ and $q_3 = q_1^2$. The concept of f^*, the effective void volume fraction, was introduced by Needleman and Tvergaard [111], to better predict the effects of coalescence. It is calculated starting from the void volume fraction, f:

$$f^* = \begin{cases} f, & f \le f_c \\ f_c + \frac{f_u^* - f_c}{f_F - f_c}\left(f - f_c\right), & f_c < f < f_F \\ f_u^*, & f \ge f_F \end{cases} \tag{A.4}$$

where f denotes the current void volume fraction, f_c is a critical value at which f^* starts to deviate from f, f_F is the value of void volume fraction at which the material is no longer capable of carrying stress andf_u^* is the value of f^* at fracture and can be calculated as:

$$f_u^* = \frac{q_1 + \sqrt{q_1^2 - q_3}}{q_3} \tag{A.5}$$

To complete the constitutive model, the total change in void volume fraction is expressed as the contribution of two different processes, the growth of existing voids and the nucleation of new voids. Mathematically this can be expressed as:

$$\dot{f} = \dot{f}_{growth} + \dot{f}_{nucleation} \tag{A.6}$$

Assuming that the growth of the existing voids is based on the law of conservation of mass, $\dot{f}_{growth}$ can be written as:

$$\dot{f}_{growth} = (1 - f)\,\dot{\epsilon}_{kk}^{pl} \tag{A.7}$$

where $\dot{\epsilon}_{kk}^{pl}$ is the trace of the macroscopic plastic strain rate tensor. Void nucleation based on plastic straining can be computed as:

$$\dot{f}_{nucleation} = A\dot{\bar{\epsilon}}^{pl} \tag{A.8}$$

where the parameter A follows a normal distribution [118], described according to Eq. A.9, where ϵ_N is the mean value of the nucleation strain, s_N is the standard deviation and f_N is the volume fraction of the nucleated void. According to the GTN model, voids are nucleated only in tension.

$$A = \frac{f_N}{s_N\sqrt{2\pi}} exp\left[-\frac{1}{2}\left(\frac{\bar{\epsilon}^{pl} - \epsilon_N}{s_N}\right)^2\right] \tag{A.9}$$

The GTN model describes material behavior with eight parameters ($\epsilon_N, s_N, f_N, q_1, q_2, q_3, f_c, f_F$). An additional parameter, f_0, can be added to the model. This parameter is introduced in the model to take into account the presence of voids in the material even before loading. In the following section, the GTN model was applied to simulate stress/strain behavior of a cylindrical specimen subjected to axial loading, in order to check if the model can correctly describe the stress/strain behavior of the considered line pipe steel.

A.2 Numerical simulations of tensile behavior of a line pipe steel

At this point, two different numerical simulations of a cylindrical specimen were developed in order to check if the GTN model can accurately describe material behavior not only in terms of stress/strain response, but also in terms of failure mechanisms.

In the present work, the model was implemented by considering the set of parameters reported in Table A.1.

Table A.1: *GTN model parameters.*

q_1	q_2	q_3	ϵ_N	s_N	f_N	f_c	f_F	f_0
1.5	1	2.25	0.3	0.1	$5{\cdot}10^{-4}$	0.02	0.1817	$1.5{\cdot}10^{-4}$

The first model considered during calculations is shown in Fig. A.1a, where the applied boundary conditions are depicted. 20 μm long quadratic axial-symmetric elements were used in the reduced section of the specimen. In Fig. A.1b, numerical results, in terms of von Mises stress, are reported: the model, at the end of the simulation, is capable of predicting necking, which occurs in the reduced section of the specimen.

In Fig. A.1c the 3D model employed for calculations is reported. In order to reduce computation time, only one eighth of the specimen was modeled. Even in this case the chosen element size, in the reduced section, was 20 μm. In Fig. A.1d the results registered at the end of the simulation are reported: necking is correctly predicted even during 3D simulation.

A comparison between the numerical stress/strain curves and the one experimentally obtained is reported in Fig. A.2: GTN model is capable of predicting the value of the ultimate tensile strength , even if the simulated curves present a more marked softening. it is worth remarking that both 2D axial-symmetric and 3D simulations provide the same results. Because of this, a new numerical model was implemented. The geometry of the small scale specimen was modeled. A crack was introduced in the model, in order to simulate the conditions present during the first strain ramp of the fatigue tests.

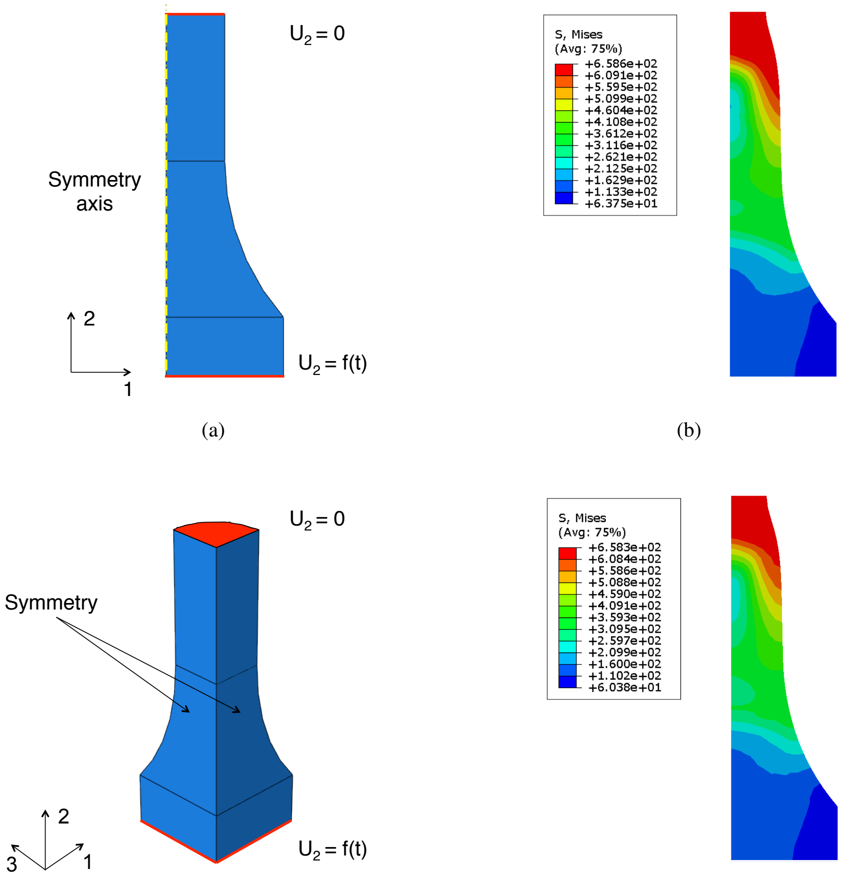
$U_2 = 0$
Symmetry axis
2
1
$U_2 = f(t)$
S, Mises
(Avg: 75%)
+6.586e+02
+6.091e+02
+5.595e+02
+5.099e+02
+4.604e+02
+4.108e+02
+3.612e+02
+3.116e+02
+2.621e+02
+2.125e+02
+1.629e+02
+1.133e+02
+6.375e+01
$U_2 = 0$
Symmetry
2
3
1
$U_2 = f(t)$
S, Mises
(Avg: 75%)
+6.583e+02
+6.084e+02
+5.586e+02
+5.088e+02
+4.590e+02
+4.091e+02
+3.593e+02
+3.095e+02
+2.597e+02
+2.099e+02
+1.600e+02
+1.102e+02
+6.038e+01

(a) (b)

(c) (d)

Figure A.1: *Numerical models employed for monotonic stress/strain simulation. a) Boundary conditions of the axial-symmetric model; b) Numerical stress distribution at necking in the 2D model; c) Boundary conditions of the 3D model; d) Numerical results for the 3D geometry at necking.*

Numerical results, together with a discussion of the FEM model employed, are reported in the following section.

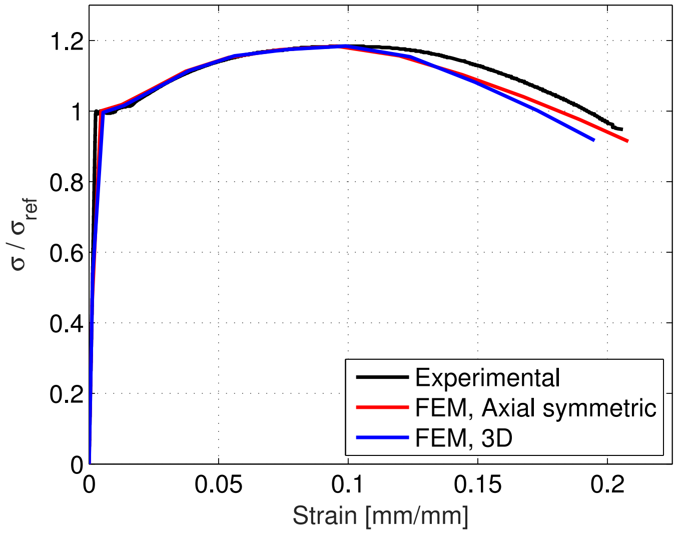

Figure A.2: *Comparison between experimental and numerical stress/strain curves.*

A.3 FEM simulation of the cracked small scale specimen

The numerical analyses of the monotonic stress/strain curve of the pipeline steel underlined the capability of the GTN model to describe material behavior, in particular when the material start softening. The following step was to apply GTN equations on a FEM model representing the specimens after compression precracking, in order to check if the damaged area observed around the crack after the first load cycle could be related to void nucleation and growth. The grid employed for calculations is depicted in Fig. A.3a: only one half of the specimen was considered, in order to reduce computational time. A semi-circular crack, whose depth was 0.5 mm, was modeled in order to simulate the defect after precracking. Mesh was refined around the crack front: the size of the elements in this area was 20 μm. An axial displacement of 0.12 mm, necessary to apply a remote strain of 0.01 mm/mm, was applied to the model, in order to simulate the initial strain ramp.

Numerical results, in terms of equivalent plastic strain, are depicted in Fig. A.3b, whereas the damage, expressed in terms of f^*, is reported in Fig. A.3a: the model predicts that an increase in void volume fraction is present around the tip, but it is equal to $2.5{\cdot}10^{-4}$, a value which is very far from f_F, the value at which the material is no longer capable of carrying stress. Moreover, the zone in which the damage initiation is present is very small, around 60 μm.

The numerical analysis based on the GTN model highlighted the fact that the speed increment is not related to a damage mechanism acting at the tip: this means that the difference between short and long crack propagation expressed in Fig. 5.5 is related to a different factor, crack closure.

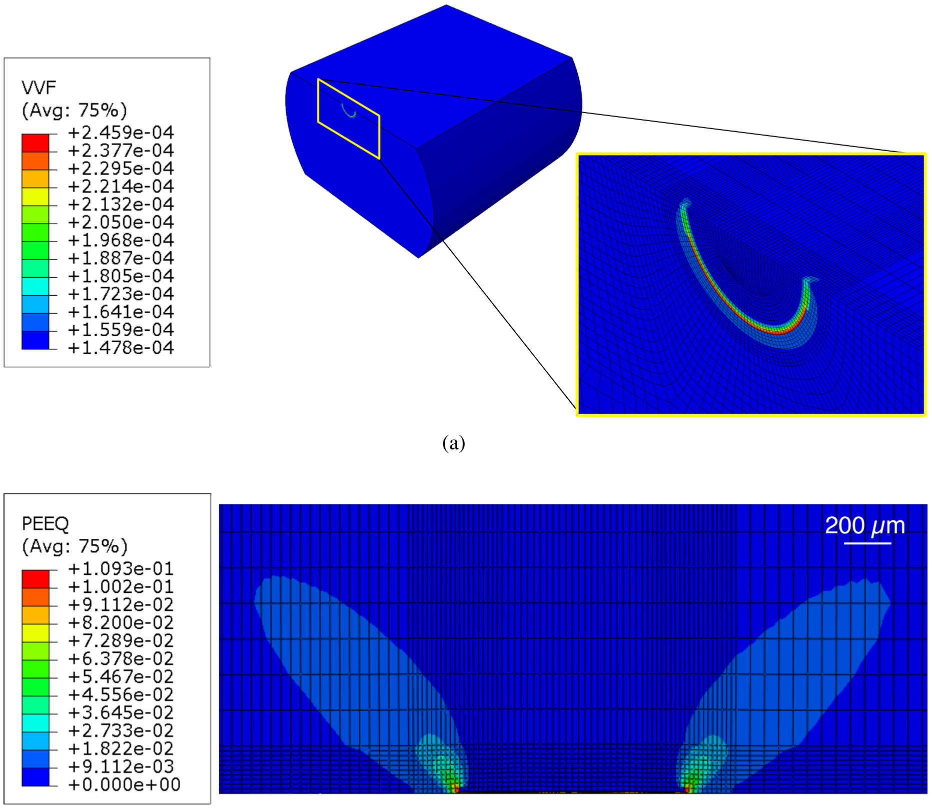
VVF
(Avg: 75%)
+2.459e-04
+2.377e-04
+2.295e-04
+2.214e-04
+2.132e-04
+2.050e-04
+1.968e-04
+1.887e-04
+1.805e-04
+1.723e-04
+1.641e-04
+1.559e-04
+1.478e-04
PEEQ
(Avg: 75%)
+1.093e-01
+1.002e-01
+9.112e-02
+8.200e-02
+7.289e-02
+6.378e-02
+5.467e-02
+4.556e-02
+3.645e-02
+2.733e-02
+1.822e-02
+9.112e-03
+0.000e+00
200 μm

(a)

(b)

Figure A.3: *3D model of the 0.5 mm deep semi-circular crack. a) Void volume fraction after the first load. b) Equivalent plastic strain (PEEQ) distribution around the crack front.*